NUMERICAL-BASED STUDY OF SPENT ACID BLOCKAGE DAMAGE IN ACIDIZED GAS WELLS

A Dissertation

by

QI ZHANG

Submitted to the Office of Graduate and Professional Studies of
Texas A&M University
in partial fulfillment of the requirements for the degree of

DOCTOR OF PHILOSOPHY

Chairs of Committee,	A. Daniel Hill
Committee Members,	Charles Glover
	Ding Zhu
	Hisham A. Nasr-El-Din
Head of Department,	A. Daniel Hill

December 2013

Major Subject: Petroleum Engineering

ABSTRACT

Aqueous fluids introduced by different stimulation treatments cause water blockage in the near-wellbore region of wells. This water blockage acts the same as formation damage when the well is put back on production. One of the examples is when gas wells in carbonate reservoirs are acid-stimulated; the wormholes that propagate into the formations might be surrounded by a region of high aqueous fluid saturation created by the leakoff of spent acid. The spent-acid blockage damage could be severe, especially in lower permeability regions where capillary forces are relatively high. This research presents studies that investigate the spent-acid damage in wormhole region of acid-stimulated gas wells.

We start the investigation with lab-scale coreflood experiments. With the experimental study, this work verifies the spent acid blockage phenomenon accompanying the acid stimulations. A model that simulates a gas flowback experiment is then developed to match with the results from the experiments. From this numerical simulation, we are able to obtain the information of the properties that cannot be measured directly from the experiments.

We then extend the research to a field-scale study by approximating the wormhole as a long, slender half-ellipsoid centered in an ellipsoidal flow field. Models that can capture both the displacement and evaporation regimes of spent acid recovery process are developed. These models are solved numerically to predict the pressure behavior and spent acid distributions during the gas flowback process.

With the numerical models, we study the effects of several key factors, such as pressure drop, pore-size distribution, and addition of additives on the efficiency of spent acid recoveries. The results show that the time needed to recovery the same amount of spent acid increases exponentially with decreasing pressure drop and absolute formation permeability. Besides, common additives routinely added to acid systems may aid, or

hinder, spent acid recovery, depending primarily on their effects on rock wettability. With the studies performed on the model developed, we provide recommendations for minimizing spent acid damage to gas well productivity.

DEDICATION

This dissertation is dedicated in loving memory of my grandfather, Ruzhou Zhang

ACKNOWLEDGEMENTS

First of all, I would like to express my deepest gratitude to both Dr. A.D. Hill and Dr. D. Zhu, for their insightful suggestions and guidance when I felt clueless; for their continuous patience and encouragement when I felt unmotivated. The opportunity they provided to broaden my professional knowledge and to prepare myself for the future challenges has been precious. Without their persistent support and help this dissertation would not have been possible.

I would also like to thank Dr. H.A. Nasr-El-Din for his invaluable advice when I first started my research. His humor and kindness makes me feel warm throughout the whole process. My sincere gratitude also goes to Dr. C. Glover for serving as my committee member and managing time out of busy schedules to read this dissertation and provide valuable comments.

My gratitude also goes to my colleagues and friends, especially Zhuoyi Li, Zhiyong Zhang, and Jichao Yin for their assistance and discussions during all these years. I would like to thank all the staff members here in Texas A&M University. Because of you guys this journey has been much more enjoyable for me. I also want to acknowledge the Qatar National Research Fund for the financial support of this study.

Finally I would like to thank my beloved parents and grandma for their unconditional love and support. Thank you for keeping me grounded and calm throughout my graduate studies.

NOMENCLATURE

a_1 to a_6	coefficients in Eq. 4-14
A_η	cross-sectional area normal to the η direction, L^2
A_ξ	cross-sectional area normal to the ξ direction, L^2
b_1 to b_6	coefficients in Eq. 4-16
B_i	phase formation volume factor, L^3/L^3
c	concentration, N/L^3
c_{sp}	ion concentration of spent acid, N/L^3
$c_{g,p}$	coefficient of $\Delta_t p_g$ in the expansion of gas accumulation, L^4t/m
$c_{g,sp}$	coefficient of $\Delta_t S_{sp}$ in the expansion of gas accumulation, L^4t/m
$c_{sp,p}$	coefficient of $\Delta_t p_g$ in the expansion of spent acid accumulation, L^4t/m
$c_{sp,sp}$	coefficient of $\Delta_t S_{sp}$ in the expansion of spent acid accumulation, L^4t/m
c_1 to c_6	coefficients in Eq. 4-17
c_l	fluid compressibility, Lt^2/m
c_μ	fractional change of water viscosity per unit change of pressure, $1/(m/Lt^2)$
D_{wh}	wormhole penetration depth into the formation, L
$\vec{e}_x$	unit vector in the x direction
$\vec{e}_y$	unit vector in the y direction
$\vec{e}_\eta$	unit vector in the η direction
$\vec{e}_\xi$	unit vector in the ξ direction
h_η	scale factor, L
h_ξ	scale factor, L
H	focus of the wormhole, L
i_{wh}	acid injection rate, L^3/t
J	Jacobian matrix
k	permeability, L^2

$k_{r,nw}$	non-wetting phase relative permeability, fraction
$k_{r,w}$	wetting phase relative permeability, fraction
$k_{r,nw}^{'}$	non-wetting phase end-point relative permeability, fraction
$k_{r,w}^{'}$	wetting phase end-point relative permeability, fraction
k_{ξ}	permeability in the direction of the ξ axis, L^2
k_{η}	permeability in the direction of the η axis, L^2
n_{nw}	non-wetting phase relative permeability exponent, dimensionless
n_{w}	wetting phase relative permeability exponent, dimensionless
p_c	capillary pressure, m/Lt^2
$p_{critical}$	critical pressure, m/Lt^2
p_e	boundary pressure, m/Lt^2
p_{entry}	capillary entry pressure, m/Lt^2
p_i	phase pressures, m/Lt^2
p_{ref}	reference pressure, m/Lt^2
p_{sp}^{s}	saturation pressure, m/Lt^2
$p_{non-wetting}$	pressure in the non-wetting phase, m/Lt^2
$p_{wetting}$	pressure in the wetting phase, m/Lt^2
q_i	production rate or flow rate, L^3/t
r_{wh}	radius of the entry hole of the wormhole, L
R	mole fraction of spent acid component in the liquid phase, fraction
R_m	effective radius, L
R_V	spent acid-gas ratio, L^3/L^3
$\vec{s}$	arc-length used in Eq. 3-5
S_i	phase saturation, fraction
S_g	gas saturation, fraction
$S_{w,irr}$	irreducible wetting phase saturation, fraction
$S_{nw,irr}$	irreducible non-wetting phase saturation, fraction

S_{nwn}	normalized non-wetting phase saturation, dimensionless
S_w	wetting phase saturation, fraction
S_{wn}	normalized wetting phase saturation, dimensionless
Δt	time step, t
t	time, t
T	temperature, T
$T_{critical}$	critical temperature, T
$T_{g\eta}$	gas transmissibility in the η direction , L^4t/m
$T_{g\xi}$	gas transmissibility in the ξ direction , L^4t/m
$T_{sp\eta}$	spent acid transmissibility in the η direction , L^4t/m
$T_{sp\xi}$	spent acid transmissibility in the ξ direction , L^4t/m
T_R	reduced temperature, dimensionless
u	volumetric velocity, L/t
$\vec{u}_i$	volumetric velocity of component i , L/t
u_{voxel}	attenuation coefficient of voxel, dimensionless
u_{water}	attenuation coefficient of water, dimensionless
u_x	volumetric velocity along x direction, L/t
u_ξ	volumetric velocity along ξ direction , L/t
v_{sp}^l	molar volume of spent acid, L3/N
V_b	gridblock bulk volume, L^3
$V_{g,s}$	gas volume measured at standard condition, L^3
$V_{sp,s}$	vaporized spent acid volume measured at standard condition, L^3
Δw_{ext}	external work
w	length along y and z direction of the small volume element, L
$W_{g,s}$	gas weight, m
$W_{sp,s}$	vaporized spent acid weight, m
Δx	difference along x direction of the small volume element, L

x	distance in the x direction in the Cartesian coordinate system, L
x_{sp}	mole fraction of spent acid component in the liquid phase, fraction
X	unknown variable used in Eq. 4-33, Eq. 4-34 and Eq. 4-35
y	distance in the y direction in the Cartesian coordinate system, L
y_{sp}	mole fraction of spent acid component in the gas phase, fraction
y_g	mole fraction of gas component in the gas phase, fraction
z	distance in the z direction in the Cartesian coordinate system, L
Z	elevation in respect to datum (positive downward), L

Greek

α	contact angle, radian
α_c	transmissibility conversion factor whose value equals 1.127
β_c	volume conversion factor whose value equals 5.614583
ε	dimensionless length in spent acid front calculation, dimensionless
ϕ	formation porosity, fraction
ϕ_0	initial formation porosity, fraction
γ	interfacial tension, $mL/t^2/L$
γ_l	fluid gravity for phase l, m/L^2t^2
η	η coordinate in an ellipsoidal/elliptical coordinate, radian
$\Delta\eta$	difference along η direction, L
φ_{sp}	spent acid fugacity coefficient, dimensionless
μ_i	viscosity, L^3/t
θ	dimensionless time in spent acid front calculation, dimensionless
$\rho^{'}$	saturated liquid density, m/L^3
$\rho_{critical}$	phase density at the critical point, m/L^3
ρ_i	phase density, m/L^3
τ	$1-T/T_{critical}$

$\Delta\xi$	difference along ξ direction, L
ξ	ξ coordinate in an ellipsoidal/elliptical coordinate, L
ξ_{wh}	ξ coordinate for wormhole, L
λ	pore-size distribution coefficient, dimensionless
ψ	ψ coordinate in an ellipsoidal/elliptical coordinate, radian
Φ	quantity used in Eq. 3-6

Subscripts

g	gas
sp	spent acid
i	index for blocks in the η direction
j	index for blocks in the ξ direction

Superscripts

n	old time step
$n+1$	current (or new) time step
$'$	first derivative

TABLE OF CONTENTS

Page

LIST OF FIGURES

LIST OF TABLES

Page

1. INTRODUCTION

1.1 Background

Gas reservoirs have been highly valued in recent years and it is estimated that more than 40% of the world's gas reserves are held in carbonate reservoirs. The Middle East, for example, is dominated by carbonate fields, with around 90% of gas reserves held within these reservoirs (as cited in Kravets, 2012). Different kinds of operations are carried out in the field and it is known that any operation is a potential source of damage to the well and might result in a decline in production rate. Matrix acidizing is the technique that has been used extensively in carbonate reservoirs to maintain or increase gas well productivity. In these treatments, aqueous solutions of acids are injected into the formations to dissolve the natural rock around the well and other solids that have been artificially introduced into the formation during the operations. The dissolution of solids by the acid solution tends to increase the absolute permeability of the rock near the well; however, poor gas production can still be observed after some treatments, especially in low-permeability reservoirs. Researchers believe that this poor performance may be because of the invasion of a large volume of spent acid (water containing reaction products) which are introduced into the formation during the stimulation operations. This phenomenon is known as water/spent acid blockage.

In a water/spent acid blockage phenomenon, liquids invade the near wellbore reservoir and create a bank around the wellbore. Once the aqueous fluids penetrate deeply into the formation, it is normally very difficult to recover them. For the purpose of restoring oil or gas relative permeability, it is necessary and important to remove these trapped liquids.

1.2 Literature Review

1.2.1 Carbonate acidizing and spent acid blockage

Carbonate acidizing is dominated by the wormholing process, the creation of conductive channels in the rock. Studies have shown that for a given reservoir condition and acid concentration, the dissolution patterns and the wormholing efficiency are acid injection rate dependent, with the compact pattern created at relatively low acid flux, the wormhole pattern developed at intermediate flux, and the uniform pattern at a higher flux. The injection rate, at which the dominant wormhole pattern is obtained, is called the optimum injection rate in an acid treatment. For highly reactive acid/rock systems, the optimum injection rate does exist and it depends on the rock mineralogy, acid concentration and reaction temperature (Wang et al., 1993). Interstitial velocity (V_i) and pore volume to breakthrough (PV_{bt}) are usually utilized to describe the wormholing process. Interstitial fluid velocity is a measure of the velocity of the fluid front, which can be calculated as $q/A\Phi$. Pore volume to break through is the ratio of the acid volume required for breakthrough to the pore volume of the core sample.

Buijse and Glasbergen (2005) presented an empirical model to predict the wormhole propagation phenomenon. The model requires two parameters: the optimum pore volume to breakthrough and the optimum interstitial velocity. These two parameters characterize the optimum conditions of wormhole propagation process in carbonate rocks and can be obtained from core flood experiments. Furui et al. (2010) analyzed field treatment data and showed that the current wormhole models under-predicted the wormhole penetration compared to field treatments responses. Their experimental results showed that smaller pore volumes were required to break through the larger cores. They developed a new wormhole model based on the Buijse and Glasbergen semi-empirical model. Their model takes into account of the acid flux at the tip of the wormhole as well

as the core size dependencies and predicts deeper wormhole penetration into the formation.

With these models, we can calculate the breakthrough pore volumes, wormhole front and the spent acid front of an acidizing treatment. Generally, if the calculated breakthrough pore volume is less than 1, the wormhole front moves faster than the spent acid front. The spent acid from the treatment would not cause further problem. Contrarily, if the breakthrough pore volume is greater than 1, the spent acid front moves at a higher rate than the wormhole front. The spent acid that goes beyond the wormhole tip might cause another issue, which is the spent acid/water blockage problem.

The spent acid/water blockage problem was brought up as early as the 1940s. In Yuster's work (1946), gas wells with gas flow retarded by water were called "water-drowned" wells. He suggested that one of the possible phenomena which are responsible for conductivity decline is the reduction in effective relative permeability due to the presence of liquid saturation. McLeod et al. (1966a, 1966b) stated that many acid treatments in sandstone which would otherwise be quite successful were spoiled by a very low spent acid clean-up. This was often a result of water block in the critical matrix surrounding the wellbore. Bennion et al. (1994, 1996, 2005) also pointed out aqueous phase trapping as one of the most severe causes that often plagued the success of low permeability gas reservoir operations when he analyzed potential formation damage types.

Since the water/spent acid blockage problem was observed, both experimental and numerical studies have been performed widely in order to achieve a faster liquid recovery rate. The most commonly considered dominant cause of water blockage is capillary pressure. In fluid statics, capillary pressure is the difference in pressure across the interface between two immiscible fluids, and is described with the famous Young-Laplace equation (Collins, 1961) as,

$$p_c = p_{non\text{-}wetting} - p_{wetting} = \frac{2\,\gamma \cos\alpha}{R_m} \quad \text{..... (1-1)}$$

where γ is the interfacial tension (also referred to as surface tension), α is the contact angle between the liquid and the solid surface, and R_m is the effective radius. In a water-wet reservoir, water is the wetting phase and gas/oil is the non-wetting phase. A displacement force is needed to overcome the capillary pressure for the non-wetting phase to migrate in such reservoirs. Thus the smaller the capillary pressure, the faster the non-wetting phase moves. By examining the equation, we can either lower the surface tension or increase the contact angle to reduce the capillary pressures and the majority of the studies were carried out by following these two concepts.

1.2.2 Experimental studies

The earliest and the mostly used method for water/spent acid blockage removal is to use solvents, such as alcohol and other water miscible organic solvents. These solvents have the ability to lower the surface tension and therefore result in a smaller capillary pressure. This method is not new to the oil industry and can be traced back to the 1940s. Yuster (1946) performed experiments on small radial sandstone cores with high vapor-pressure, low surface-tension liquids which were completely miscible with water. He found that the application of these liquids removed water from the critical matrix surrounding gas wells almost completely. Some of the liquids used with success were acetone and a 9-to-1 mixture of acetone and diethyl ether.

Alcohol was then successfully used by McLeod et al. (1966a, 1966b) as part of the stimulation fluids in gas wells for both matrix acidizing and hydraulic fracturing, particularly in heterogeneous sandstone formations with slow clean-up histories. They concluded that formations which contain more than five percent clay were prime candidates for alcohol fluids. Optimum alcohol concentrations in acid for water block removal are 20 percent isopropyl (IPA) or 30 percent methanol. Meanwhile alcohol

content in water-base fracturing fluid runs from 15 to 50 percent and depends upon which polymer system is used.

This method continues to play an important role even nowadays because of its low cost. Al-Anazi et al. (2002, 2005a, 2005b) addressed the adverse impacts of completion fluids and condensate banking on gas relative permeability. They conducted a series of coreflood experiments on both carbonate and sandstone, high and low permeability core samples. Methanol, isopropyl and alcohol brine mixtures were examined to assess their effectiveness in removing or reducing liquid blockage. A treatment in Hatter's Pond field, Alabama (Al-Anazi et al., 2005c) showed increases in gas and condensate productivity after a methanol injection treatment and indicated a successful field application.

Although the solvent injection method is cost-efficient, it offers only temporary productivity restorations, which is relatively short compared to the entire production duration. Early in Penny et al.'s work (1983), a material that could absorb to the matrix surface and render it non-water wet was placed in the methanol containing prepad. With the change of contact angle, the resulting non-water wet surfaces exhibited nearly zero capillary pressures and promoted a rapid, thorough cleanup of injected water. Based upon the same idea, Li and Firoozabadi (2000) started the studies of altering rock wettability from liquid wetting to intermediate gas-wetting with chemical treatments. They believed that the strong liquid wetting attributes of the rocks lead to low liquid mobility. With the wettability alteration, an increase in liquid mobility was obtained, preventing the accumulation of liquid with high saturation, and resulting in high gas production rates.

Since most reservoirs are at elevated temperatures, the chemical solutions need to be tested to assure their stability and effectiveness at higher temperatures. In the precursor work of Firoozabadi (Li and Firoozabadi, 2000), the alteration was completed at 24^{o}C. Tang and Firoozabadi (2002, 2003) then increased the operation temperature up to 90^{o}C, and measured the effect of wettability alteration on liquid mobility. However, Fahes and Firoozabadi (2007) found that those chemicals were ineffective at 140^{o}C and

they were successful in finding high temperature sustainable alternative chemicals which could permanently alter rock substrates from liquid-wetting to intermediate gas-wetting. They also indicated that the wettability alteration did not have a measurable effect on the absolute permeability of the rock. The chemicals that were used in their studies were mainly fluorochemical surfactants, which were tested mostly on sandstone core samples with contact angle and spontaneous imbibition experiments.

More chemicals were tested and applied because of the excellent attribute of wettability alterations. Panga et al. (2006) examined five different chemicals with coreflood experiments and evaluated their abilities to prevent water blockage formation at high temperatures. Sharma and his research group performed a series of studies (Kumar et al., 2006; Xie et al., 2008; Bang et al., 2009). They successfully treated both Berea and reservoir sandstones at reservoir conditions using several surfactants in different solvent mixtures. Their experimental work mainly consisted of chemical screening, selection of solvent mixtures, spontaneous imbibition and coreflood experiments. Based on their lab scale studies, Butler et al. (2009) applied the wettability alteration technique in a sandstone reservoir in Oklahoma and demonstrated the treatment was highly effective. Although they aimed mainly at finding chemicals to mitigate accumulation of condensate in gas reservoirs, their work is still instructive for water blockage removals. Ahmadi et al. (2011) extended their chemical treatments to mitigate liquid blockage in carbonate gas formations. Besides traditional contact angle and imbibition tests, they used X-ray Photoelectron Spectroscopy (XPS) to screen the chemicals beforehand. It was demonstrated that the treatment was effective at high pressure and high temperature (HPHT).

Trapped liquid recovery is accompanied by vaporization. This phenomenon was observed in the 1940s too, but it was not studied in detail until the 2000s. Kamath and Laroch (2003) exposed their coreflood experiments to large pore volume of gas flow and found that the cleanup of water in gas wells occurred in two regimes: (1) displacement of

the fluid from the core followed by (2) vaporization of water by the flowing gas. The second regime gives slow displacement, and the deliverability slowly increases during several months. They suggested that short term well tests may erroneously exaggerate the extent of gas deliverability loss because of water blockage since it is a transient phenomenon. And adding alcohol can improve the second regime dramatically.

Zuluaga et al. (2001, 2003) performed experiments to determine water vaporization rate by flow in dry gas through porous media, such as unconsolidated sandpacks and consolidated Berea cores. Their tests indicated that water vaporization rate increased with increasing gas flow rate and temperature, and decreased with increasing pressure and salinity.

Mahadevan and Sharma (2003) conducted gas displacement experiments for long periods of time (up to 10,000 PV) on cores that were fully saturated with brine at ambient temperatures. They studied the effects of rock permeability, wettability, temperature, pressure drawdown and surfactants on the cleanup processes and the results also showed that volatile solvents affected the evaporation regime more than displacement regime. Bazin et al. (2010) investigated fracture-face damage in tight gas core samples by injecting gas for a long time. Their studies implicated that adding methanol in fracturing fluid can help to reduce water blockage. They believed that with the presence of methanol the portioning of water between gas and liquid phases was thermodynamically modified. As a consequence, evaporation was enhanced.

1.2.3 Numerical studies

Although not as widely applied as experimental work, numerical simulations have also been tried by researchers to quantify the effects of water blockage. Due to the complications of the involvement of evaporation in the water/spent acid recovering process, numerical simulations have come out with diverse results.

A large portion of simulations are based on modified equation of state compositional models (Bette and Heinemann, 1989; Kurihara et al., 2000). In this method, water is usually treated as a component among other species in the hydrocarbon phases and it allows for mass transfer between the aqueous phase and the hydrocarbon phases. This modification results in more algebraic constraints over the usual compositional equations. But since it is physically founded, this method is versatile in application.

Efforts have been devoted to the development of simple models which can account for evaporation as well. Humphreys (1991) developed a modified form of material balance equation to take into account significant water vaporization effects, providing the mole (volume) fraction of the vapor phase was measured experimentally. The modified form could be used to accurately predict gas-initially-in place and recovery factor, and hence, the reserves. In Kamath and Laroche's work (2000), the K_{rg}-PV_{gas} curves under reservoir conditions are obtained from upscaling the laboratory data for both binary and ternary systems by considering evaporation regime effects. A skin factor was then defined to account for this altered permeability around the well, which could be used in well deliverability calculations for different situations.

Based on Humphreys' idea, Zuluaga and Lake (2004) proposed a semi-analytical model for water vaporization in gas producers. In the model, gas phase pressure could be calculated analytically from the pseudo-pressure equation. The vapor-liquid equilibrium was computed for the new pressure and the water saturation would be updated accordingly. In their study, capillary pressure was also considered by introducing a modified equilibrium constant. Parekh and Sharma (2004) studied cleanup of water blocks in depleted low-permeability reservoirs by using a chemical flooding simulator, in which black oil model was used. Effects such as drawdown, capillary pressure, and relative permeability were analyzed. Their results suggested the need of lowering

capillary pressure by reducing interfacial tension and/or altering wettability of the rock surfaces.

Mahadevan et al. (2007a, 2007b) proposed a mathematical model for the evaporative cleanup of water blocks in gas wells. Their model was developed by rearranging water and gas mass conservation equations and then solved numerically. The model was used to calculate the saturation profiles in both unfractured and fractured wells. They studied the effects of several factors and concluded that the impact of evaporation on the improvement of the gas relative permeability is quite significant.

1.3 Objective and Approach

This project is aimed at 1) studying the spent acid propagation phenomena in acid treatments in detail; 2) analyzing the effects from the possible factors which might affect the spent acid cleanup process after the treatments. We carry out the studies both experimentally and numerically.

Most of the previous studies were conducted on very small scale core plugs and no research has been performed with real acid treatments and spent acid invasion involved. In this project, we design an experiment on larger dimension core samples. The experiment simulates wormhole growth and it allows us to capture the spent acid distribution profiles. CT scan technique is utilized in the experiments to get a better interpretation of the experiment results. Several common acid additives are also added to observe their effects. Then, a model that simulates the coreflood experiment is built to match with the experimental results. With the simulation study, we are able to obtain general ideas of the parameters which cannot be measured directly from the experiments, such as capillary pressure and relative permeability behaviors.

From the existing studies, we know the time required for the recovery of spent acid from the formation depends on a number of possible factors, such as pressure drop,

temperature, relative permeability characteristics and capillary pressure. These factors should be carefully studied especially in the case of low permeability formation for proper prediction of the cleanup process and the productivity enhancement. In this study, we use a half prolate spheroid to approximate the wormhole geometry and simulate the spent acid recovery process at the field scale. The numerical simulation includes both displacement and evaporation regimes. The parametric studies give us quantitative understanding of the effects from several possible affecting factors. This combined experimental and theoretical study is expected to help us improve the efficiency of the matrix acidizing process in gas reservoirs.

For the rest of this dissertation, in **Chapter 2**, we briefly cover the CT scan technology first and follow up with detailed explanations of experiment procedures. The simulation model which is developed to further analyze the experiment results is then described before we present the results. In **Chapter 3**, the physical model which resembles wormholes from real field acid treatments is delineated first. Based on this approximation, spent acid balance equations are introduced and solved by using the method of characteristic. **Chapter 4** presents the spent acid recovery model which is able to cover both the displacement and evaporation regimes. The method used to solve the model is described before the validations of the program are given at the end of the chapter. In **Chapter 5**, parametric studies results are discussed for both displacement and evaporation parts. The parameters we study include pressure drop, porosity, formation pore-size distribution and capillary pressure. At the end, we draw conclusions based on the preceding results and discussions in **Chapter 6**.

2. EXPERIMENTAL STUDY*

2.1 Introduction

During an acid treatment, a stimulated zone with high permeability is created in the near wellbore region due to the wormholing process. Thus after the stimulation, we should see less pressure drop than predicted by the radial flow equation. However, as is mentioned in the foregoing descriptions, spent acid/water from the reactions might penetrate deeper beyond the wormhole tips and form a high liquid saturated zone, as illustrated in **Fig. 2.1**. This zone has the potential of cancelling the benefits we can get from acid treatments and is plainly unwelcome.

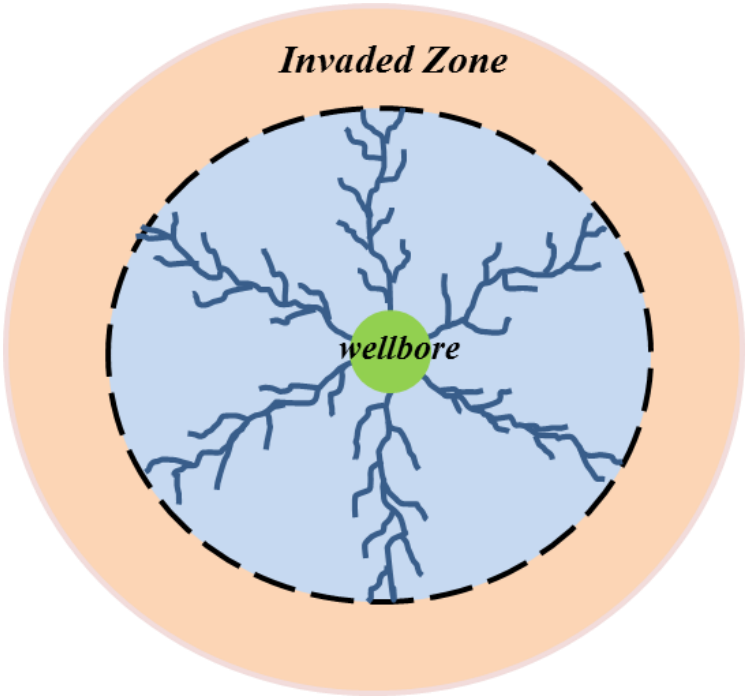

Fig. 2.1 Spent acid invade beyond wormhole tips during acid treatments

*Part of this section is reprinted with permission from "Modeling of Spent-Acid Blockage Damage in Stimulated Gas Wells" by A.D. Hill, Q. Zhang, D. Zhu. Paper IPTC 16481-MS presented at the International Petroleum Technology Conference, 26-28 March 2013, Beijing, China. Copyright 2013 by International Petroleum Technology Conference.

Experiments have been performed extensively to investigate this problem, among which core-flooding tests are the most commonly used strategy. The core-flooding tests usually involve different kinds of chemicals and they need to be examined beforehand. Various techniques, such as X-ray photoelectron spectroscopy (XPS) analysis (Ahmadi et al., 2011), contact angle test and imbibition test, are employed to screen these chemicals. Core-flooding tests are then carried out with these chemicals included and some of them are performed under high pressure and high temperature (HPHT) conditions to simulate real reservoir circumstances. Gas productivities measured before and after the treatments are normally compared to evaluate the durability of the chemicals as well as the effectiveness of the treatments. In addtion, X-ray computed tomography and three-dimensional post-processing techniques have become a helpful method of monitoring the variations in core samples during the experiments in recent years.

The majority of the existing studies have been concentrated on exploring effective methods to remove or mitigate the side effects from the spent acid affected zone. In this research, we focus on the spent acid penetration phenomenon accompanying with the acid treatments. Aside from that, we also study the spent acid recovery process following the treatments. In order to do that, this section presents: 1) the lab-scale experiments which is developed to examine the spent acid penetration and recovery phenomenon in the treatments; 2) the simulation which is utilized to help us to analyze the experiment data.

2.2 Lab-scale Experiments

2.2.1 Experimental 3d visualization

Despite being invented for medical purposes, X-ray Computed Tomography (CT scan) has been widely employed in many industries to help produce 3D representations of objects. Flow in porous media has become one of its important uses. Elaborated

descriptions of basic principles and usages can be found in earlier papers (Goldman, 2007; Izgec, 2009). Only delineations of several concepts that are involved in this work are given here.

In a CT scanning, the object, such as a core plug, is scanned by X-rays at axial slices which are apart from each other to produce a volume of cross-sectional data. Each slice is then divided into a matrix of 3-dimensional rectangular voxels of materials for CT image reconstruction. The objective is to determine how much energy attenuation occurs in the narrow x-ray beam. The attenuation is related to electron density and atomic number of the materials present in the object being scanned. Each material possesses a distinct linear attenuation coefficient, and the total response received by the detectors is a combination of these coefficients (Izgec, 2009). A convention that has existed from the earliest days is to replace the attenuation value for each voxel with the following integer, which is also known as the CT number.

$$CT\ number\ (in\ Hounsfield\ units, HU) = 1000 \cdot \frac{u_{voxel} - u_{water}}{u_{water}} \quad \text{..... (2-1)}$$

In this equation, u_{voxel} is the calculated voxel attenuation coefficient, u_{water} is the attenuation coefficient of water. Apparently, a voxel with only water inside it has a CT number of 0, since $u_{water} - u_{water} = 0$. Meantime, if the voxel contains only air (for which $u_{air} \approx 0$), the CT number would be approximately -1000 (Goldman, 2007). According to Tanaka (2011), higher density and higher atomic numbers result in higher attenuation of X-rays. Thus for the core samples that are used in our experiments, we would expect higher CT numbers.

Once the data set is ready, we use three-dimensional image processing software to post-process them. In the post-processing, we obtain not only the CT number distribution along the entire sample, but also the inner structures of the sample. This procedure definitely makes the understanding of the experiments easier and better. One thing that

needs to be mentioned here is that artifacts can easily be introduced in the scanning and can seriously degrade the accuracy of the tests (Barrett and Keat, 2004). Thus in order to achieve higher quality CT measurements and comparisons, the X-ray attenuations must be distinctly different under various circumstances. According to Withjack (1988), to increase the difference, dopants may be added. At present, all water-soluble radio-contrast agents rely on iodine as it is quite radio-opaque (i.e., it absorbs X-rays well).

In this work, we scan the cores by using an industrial high-resolution X-ray CT scanner in the Department of Petroleum Engineering at Texas A&M University. Compared with medical scanners, this instrument operates at higher energies, which enables users to scan high density objects with higher resolutions. The doping agent that is used in our experiments is sodium iodide (NaI).

2.2.2 Acid additives

There is a vast collection of chemicals that are routinely added and injected along with acid solutions for different purposes during carbonate stimulations. The effects of these additives on rock properties can be either favorable or unfavorable. It is very important to understand the impacts from these acid additives. Studies have been performed under static conditions to measure surface tension and contact angles, since they are the two main parameters that control the capillarity (Saneifar, 2011). In this research several commonly used acid additives are included in acid treatments and their effects under flowing conditions can be studied.

In general, acids attack steel to produce solutions of (mainly) iron salts while generating hydrogen gas. Depending on the steel metallurgy, type of acid, its strength and the temperature, the reaction may be more or less vigorous. However, particularly with mineral acids, this attack can lead to the removal of a substantial amount of metal mass, potentially weakening or shortening the lifespan of the equipment (Rae and Lullo, 2003).

Corrosion inhibitor is the additive that is used to prevent metal equipment and structures, such as well tubular, mixing tanks, and coiled tubing from corrosions. They must remain effective under reservoir pressure and temperature for the duration of the treatment and must not react with the acid itself. The corrosion inhibitors used in this work are a formic acid based corrosion inhibitor, which for the purpose of this study will be called FA-CI and a methanol and isopropanol based corrosion inhibitor, which for the purpose of this study will be called MI-CI.

In any oilfield operation, all those metal equipment and structures are the possible sources where iron can enter the solutions. They can add up to a significant concentration of iron in the live or partially spent acid. Several iron reaction products can precipitate from acid as it spends and the pH rises. The most likely is ferric hydroxide, which forms a gelatinous, plugging precipitate when the acid pH rises about pH 2.2. Various chemical methods have been employed to address this issue of iron precipitation. The most common ones include chelation/sequestration (EDTA, citric acid and its salts) and reduction (erythorbic and ascorbic acids) (Rae and Lullo, 2003). Iron Control agents used in this work are a citric acid based iron control agent, which for the purpose of this study will be called CA-ICA and a trisodium nitrotriacetate (trisodium NTA) based iron control agent, which for the purpose of this study will be called T-ICA.

2.2.3 Core-flood experimental procedure

In all, the experiment comprises an acidizing treatment, a gas flowback procedure and several CT scans.

The core samples used in this study are either Texas cream chalk or Indiana limestone. They are cut into 1.5 inch diameter by 20 inch long specimens. We keep all the core plugs dry before acid treatments in order to simulate the gas reservoir conditions. At the very beginning, we always weigh the cores for porosity calculation purpose. The

core sample is then CT scanned for the first time to get the CT number distribution along the core sample.

Next is the acid treatment. The schematic of the acidizing set-up is shown in **Fig. 2.2** and the details of the set-up can be found in Nevito's work (2006). At the beginning of the experiment, the core is placed in a standard hastelloy core holder and the fluids are stored in different accumulators. Overburden pressure is applied around the core sample to make sure the fluids does not bypass the core and this pressure is usually kept at least 300 psi above the core inlet pressure. In the experiment, the pressure drop is monitored by using differential pressure transducers. We begin the test by flowing nitrogen through the system till the pressure drop across the core is stabilized. With the known injection rate and pressure drop, the permeability of the core sample can be estimated by using Darcy's law. Following that, acid solution is injected into the system. The acid solutions used in this work are usually 15 wt% HCl solution, into which different additives are added. In order to keep reacted carbon dioxide in the solutions, the backpressure needs to be maintained to at least 1000 psi.

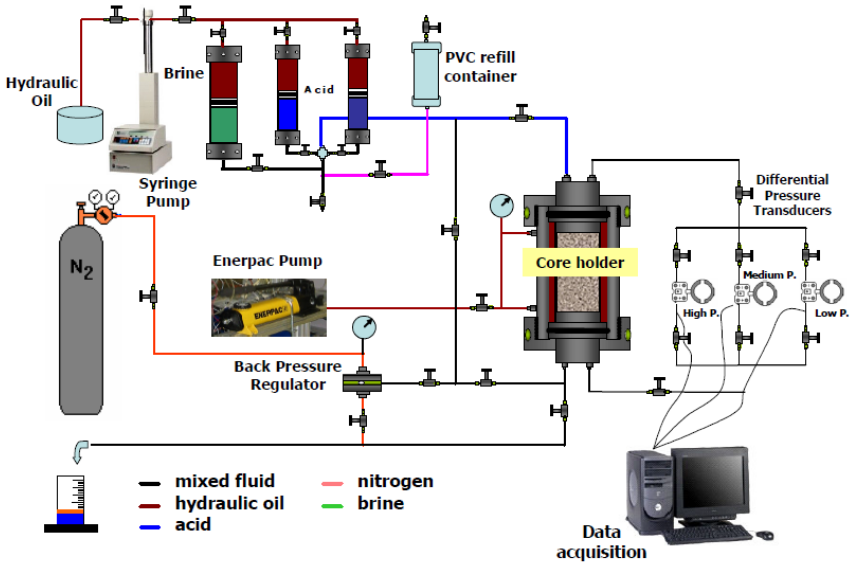

Fig. 2.2 Acid core-flooding experiment schematic

Fig. 2.3 Illustration of the fluid flow directions

Different from the traditional acidizing experiments, in this study the acid treatment is always terminated before the pressure difference drops to a negligible value (indication of wormhole breakthrough). This practice will end up with wormholes only partially penetrating the core plugs and gives us extra room to examine the possible spent acid blockage phenomenon. When acid treatment is finished, the core sample is taken out of the core holder and sent for another CT scan.

Then the core plug is put back in the set-up and nitrogen is flowed back from the other side of the sample, as shown in **Fig. 2.3**, to simulate the gas production as well as the spent acid recovery process. During this procedure, both inlet pressure and outlet gas flow rate are recorded. The gas flowback procedure lasts for about 2 hours. After that, a final CT scanning is performed on the same core sample. One thing that needs to be pointed out is that we should start all the scans at the same or at least close enough positions on the same core sample. Because we will need to compare the data from all these three scans in the succeeding analysis, to do this is helpful in ensuring the accuracy of the comparisons.

2.2.4 Experimental results

In the X-ray CT scans of this study, the separation distance between each slice is set to be 4 mm and it results in a total of 126 CT scans with the dimension of our cores (20 inches). CT scans are taken along the core. The higher we want the resolution of the results to be, the more scans should be taken. In **Fig. 2.3** the images of the slices from a core sample are shown in sequence. In the first 50 or so images, we can observe obvious

dark dots and they are the images of the wormhole. Besides, a distinct color contract can be seen in the final row of the images and it is a sign of heterogeneity of the core sample. After gathering the large volume of data together and post-processing them, we get the 3-D interpretation of the interior of the core sample, which is presented in **Fig. 2.4** and **Fig. 2.5**. The figure clearly denotes that the wormhole terminates inside the core just as we designed. The results from the above analysis are straightforward and it also shows that the CT scan and 3-D post-processing technologies are very helpful in core sample characterizations.

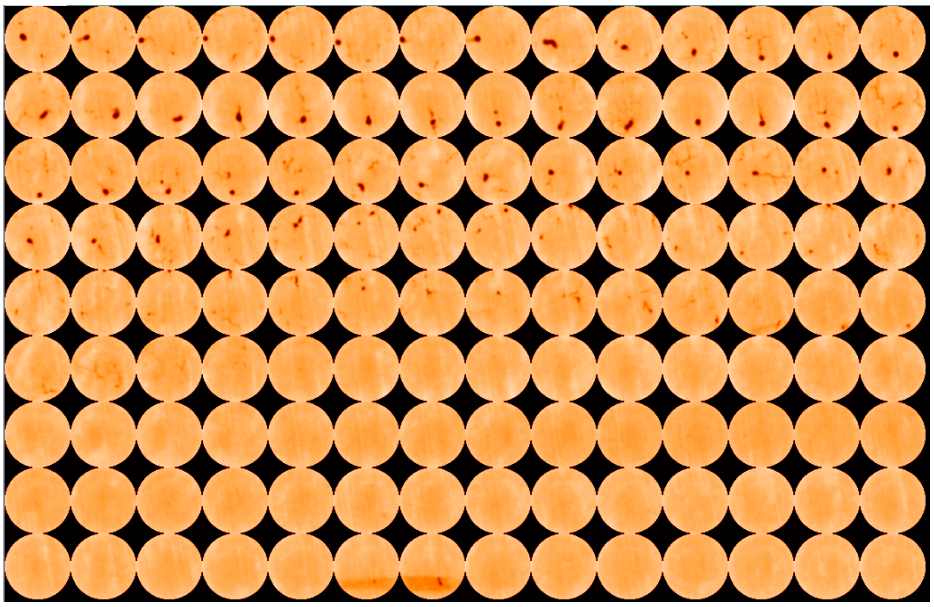

Fig. 2.4 CT scan slices of a sample core plug

Fig. 2.5 3D constructed wormhole of a sample core plug

We carried out acidization and gas flowback for a total of ten experiments. The details of the core samples as well as the experimental conditions and results can be found in Nasir's work (2012). In **Table 2.1**, we list the details of four of the experiments.

Table 2.1 Experiment conditions and results

ID	Additive	K mD	$Q_{gas,\ outlet}$ L/min	T_{inj} min	Wormhole end, slice	Spent acid end, slice
Ind 9	None		19.5	45	52	66
Ind 12	T-ICA	3.4	5.7	120	73	92
TxCC 4	FA-CI	3.5	3.5	120	14	26
TxCC 5	T-ICA	4.0	6.5	120	50	66

In the four experiments that are mentioned in **Table 2.1**, the first two were performed on Indiana limestone and the other two were performed on Texas cream chalk. Iron control agents were used in experiments Ind 12 and TxCC 5; corrosion inhibitor was used in TxCC4 and no acid additive was used in Ind 9. The amount of sodium iodide that

was adopted in the experiments is 5 wt. % and the amount of all the additives are 2 wt. %. The CT scan results for these experiments are shown in **Fig. 2.6** through **Fig. 2.9**. In each figure, we present CT number distributions along the core sample before and after the acidizing, as well as the one after gas flowback. These curves are put together and compared with each other to study the spent acid penetration and recovery processes.

In all these figures, we can find that the curves depicting dry core average CT numbers always lie at the very bottom. It is because the pores in dry core plugs are saturated with air and air has a relatively low CT number ($CT_{num,air} \approx 0$). After the acid treatment, a wormhole has formed in the core samples. The end points of the wormholes are marked in all figures according to the 3-D post-processing image results. Meanwhile, as a result of the invasion of high CT number fluids, average CT number curves go up in all the cases in the wormhole region. It can also be observed that high CT numbers do not just stop at the end of the wormholes; instead they keep spreading farther into the core samples and then decrease till the dry core level. The zone between the wormhole end and the dry core section is the spent acid invaded region which was mentioned earlier in this chapter. In reality, this zone has the potential of blocking the critical matrix surrounding the wellbore and further decreasing well productivity.

During gas flowback, with the displacement of spent acid from the core plug, the average CT number curve goes down. Differences between CT number curves before and after gas flowback are highlighted in all the figures. We can notice that differences are observed only around the wormhole tip zone and no obvious difference show up in the wormhole region. It means that only part of the spent acid around the tip zone was recovered within about 2 hours gas flowback. If we want more spent acid recovered from the core plugs, we need to extend the time we run gas flowback.

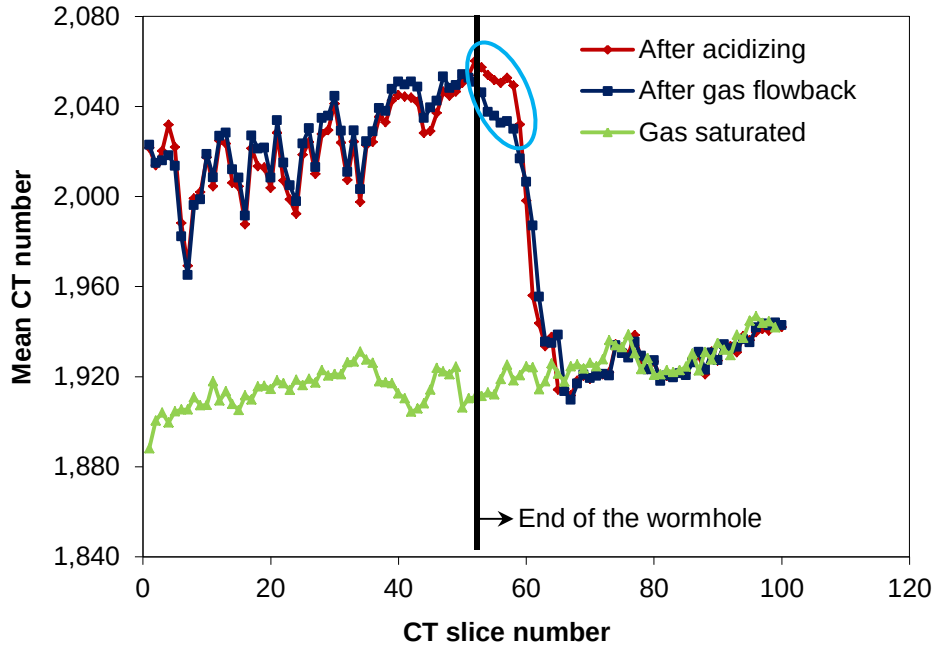

Fig. 2.6 CAT scan results (Ind 9)

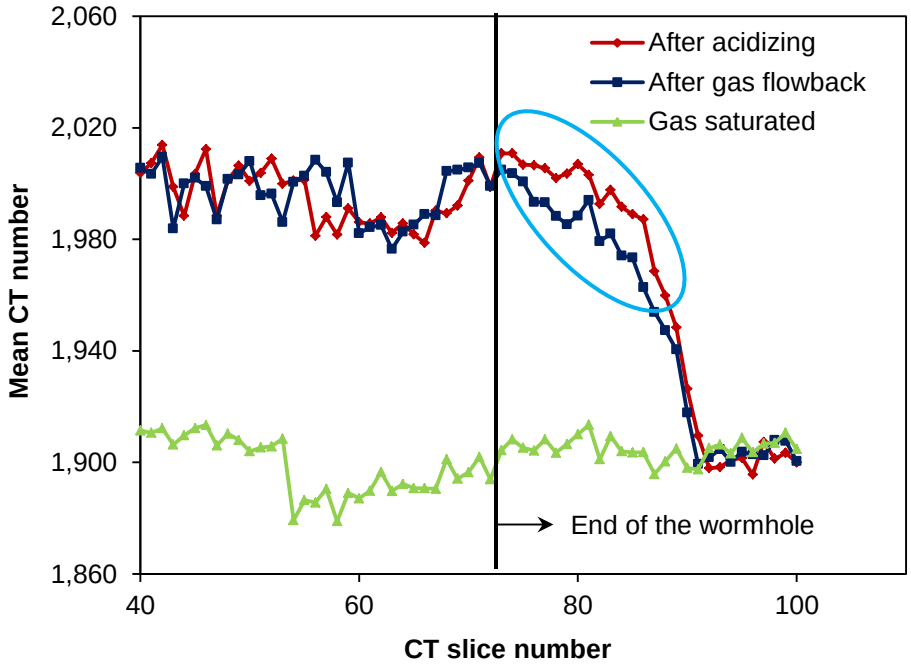

Fig. 2.7 CAT scan results (Ind 12)

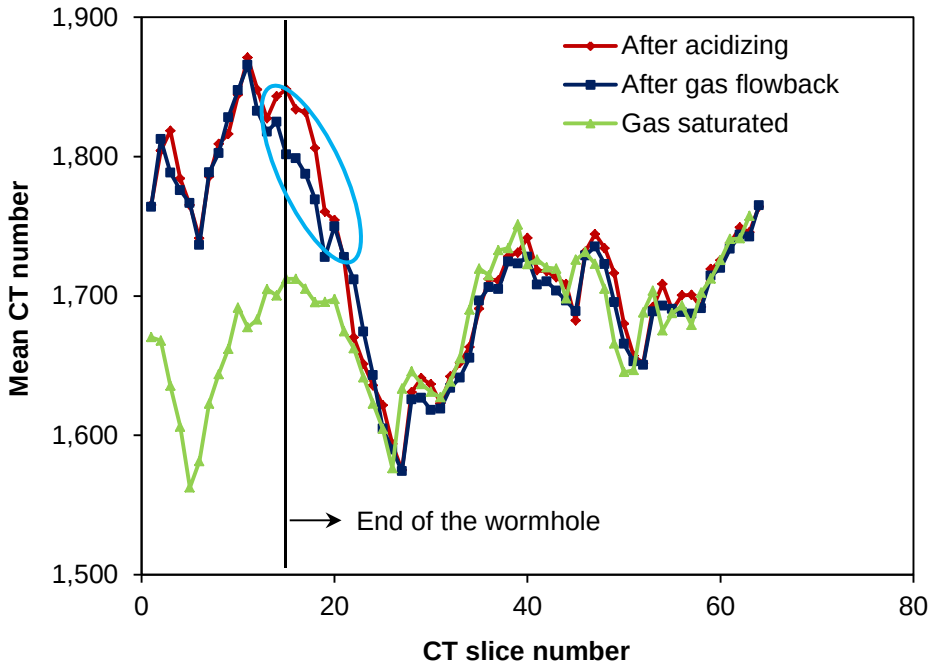

Fig. 2.8 CAT scan results (TxCC 4)

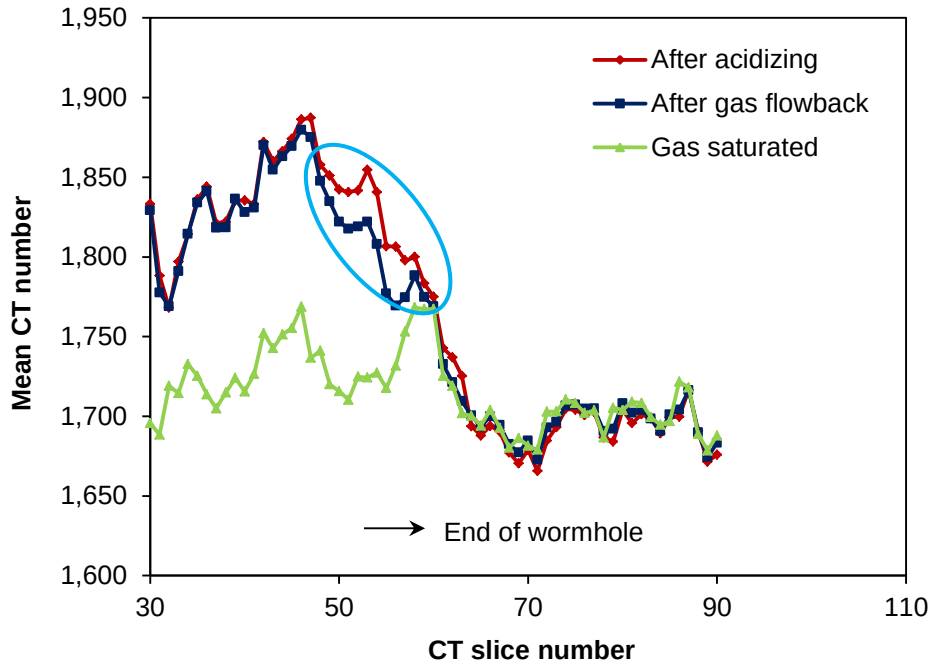

Fig. 2.9 CAT scan results (TxCC 5)

2.3 Simulation of Experiments

2.3.1 Experiment simulation model

During the experiments, we are able to obtain the information of several formation properties, such as porosity and absolute permeability. However, it is difficult for us to get the information of some of the other properties, such as relative permeability and capillary pressure. These properties are essential for fluid flow calculations and further engineering estimations. Particularly, in some of the acid treatments that were discussed above, different acid additives were added. These additives are known to have an influence on surface tension and contact angles. We are interested in learning the relative permeability and capillary pressure characteristics of these core samples after the treatments.

Different measurement techniques have been developed to determine relative permeability of porous media. Most of the measurements fall into two main categories: steady-state or unsteady-state measurements. Sometimes empirical models are used to estimate relative permeability because of the difficulties involved in the measurements. Relative permeability can also be determined from the production history of a reservoir and its fluid properties (Honarpour and Mahmood, 1988).

For this study, since we know some properties of the core sample and also the gas flow information of the gas flowback process, we can build a simplified numerical model to simulate this process and thereby obtain the unknown properties from this experimental matching.

The model is built with commercial software (ECLIPSE E100) and the model parameters are extracted from the experiments. Since the core is cylindrical, only the cross section is considered by accounting for the symmetries. The dimensions of the model are scaled up from the experiments proportionally. In most of the cases, we scaled up the experiment model by 200 times, which results in a scaled-up model of 25ft by 333

ft. In addition to that, finer grids are assigned to the wormhole and the spent acid affected zone for higher accuracy. A sample of experiment simulation grid is shown in **Fig. 2.10**.

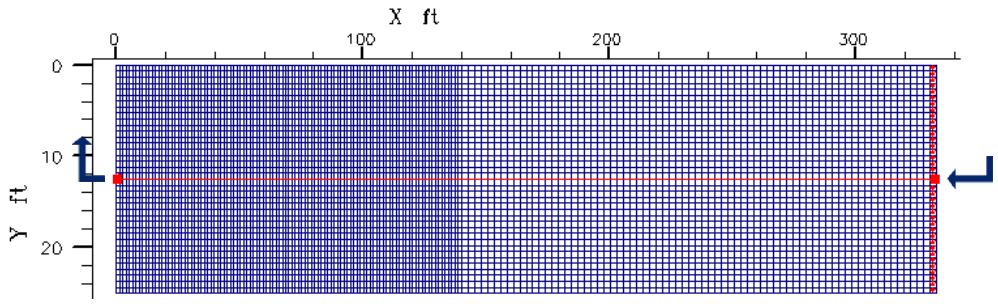

Fig. 2.10 Sample of experiment simulation grids

For properties that can be measured from the experiments, such as porosity and absolute permeability, the same values are applied to the simulation model directly. Since wormholes are more conductive than the rest of the matrix, we assign a much higher permeability to the grid blocks where the wormholes are located. Initial spent acid saturation is assumed to be 1 for the grid blocks in wormhole zone and 0 for the grids in the unaffected zone. For the spent acid affected region between these two zones, we obtain the initial saturation by linearly interpolating the average CT numbers that are obtained right after the acid treatments. An example of the spent acid initial saturation is given in **Fig. 2.11**. At the inlet of the simulation model, constant injection pressure is applied according to the experimental conditions.

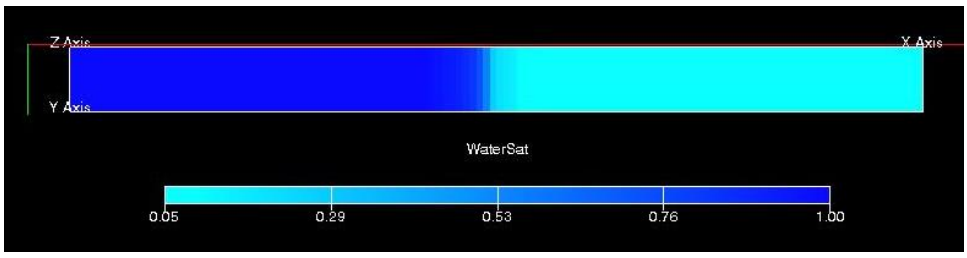

Fig. 2.11 Initial spent acid distribution in experiment simulation model

Table 2.2 Experimental and simulation model conditions

Conditions	P	V	Z	T
1. Experiment outlet	√	Measured	√	√
2. Experiment inlet	√	PV_{inj}	√	√
3. Experiment simulation model inlet @ reservoir condition	√	PV_{inj}	√	√
4. Experiment simulation model outlet @ standard condition	√	$PV_{standard}$	√	√

Within the matching process, gas/spent acid relative permeability and capillary pressure profiles are adjusted, since they cannot be measured directly in the experiments. The real gas law is applied to calculate the gas volumes. In the experiments, we use a gas flow meter to obtain the gas volume from flow rate at the core outlet. This value is then used to calculate gas pore volumes at the core inlet and it is also the gas pore volume value that is used in simulations. However, since output files in the software are written at standard conditions, an additional conversion is needed to get the gas volume at this condition. In **Table 2.2**, we list the conditions that are involved in the calculations. With all the parameters set, we are now ready to run the simulations. A sample ECLIPSE input file for experiment simulation study is presented in **APPENDIX A**.

2.3.2 Experiment simulation results

Experiment simulations were carried out for the experiments that were listed in **Table 2.1**. From the experimental CT scan results (**Fig. 2.6** through **Fig. 2.9**), we know that only part of the spent acid was recovered around the wormhole tip zone. The goal of the scaled-up simulation is to adjust relative permeability and capillary profiles to match this change. The relative permeability model that is used in the matching process is the modified Brooks and Corey model or the power law model (Brooks and Corey, 1964), which is expressed in Eq. 2-2 and Eq. 2-3.

$$k_{r,w} = k'_{r,w}(S_{wn})^{n_w} \qquad n_w = 3 + 2/\lambda$$
$$k_{r,nw} = k'_{r,nw}(S_{nwn})^{n_{nw}} \qquad n_{nw} = 1 + 2/\lambda \quad \text{..... (2-2)}$$

where,

$$S_{wn} = \frac{S_w - S_{w,irr}}{1 - S_{w,irr} - S_{nw,irr}} \quad \text{..... (2-3)}$$

is the normalized wetting phase saturation. For capillary pressure, we use the following equation,

$$p_c = p_{entry}(S_{wn})^{-1/\lambda} \quad \text{..... (2-4)}$$

When we match the scaled-up simulation results with the experimental results, we mainly adjust exponents n_w and n_{nw}, as well as the pore-size distribution coefficient λ. In **Table 2.3**, the parameters that are used for k_r and p_c calculations are summarized.

Table 2.3 Relative permeability and capillary pressure parameter summary

Exp ID	Additive	$S_{sp,irr}$	$S_{g,irr}$	p_{entry}, psi	n_{sp}	n_g	λ
Ind 9	None	0.15	0.001	2	5	3	1
Ind 12	T-ICA	0.15	0.001	2	5.5	3.5	1
TxCC 4	FA-CI	0.15	0.001	2	2.5	4.0	1
TxCC 5	T-ICA	0.15	0.001	2	4	2	1

In **Fig. 2.12** through **Fig. 2.15**, the experiment and simulation results are shown together. The curves in these figures represent the differences between the average CT numbers before and after the gas flowback. On these curves, fluctuations are observed along the whole core plug. Some of these fluctuations might due to the change of experimental conditions or the experimental errors. Nevertheless, we can still notice the abrupt changes around the wormhole tip zone in all the cases and this is because of the recovery of part of the spent acid during the gas flowback process.

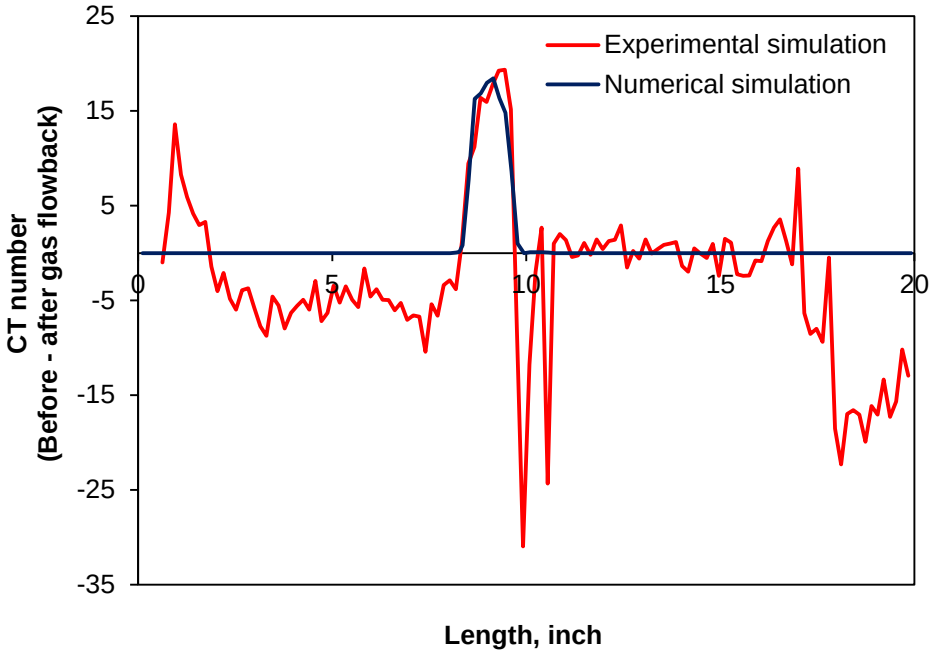

Fig. 2.12 Comparison between experiment and simulation (Ind 9)

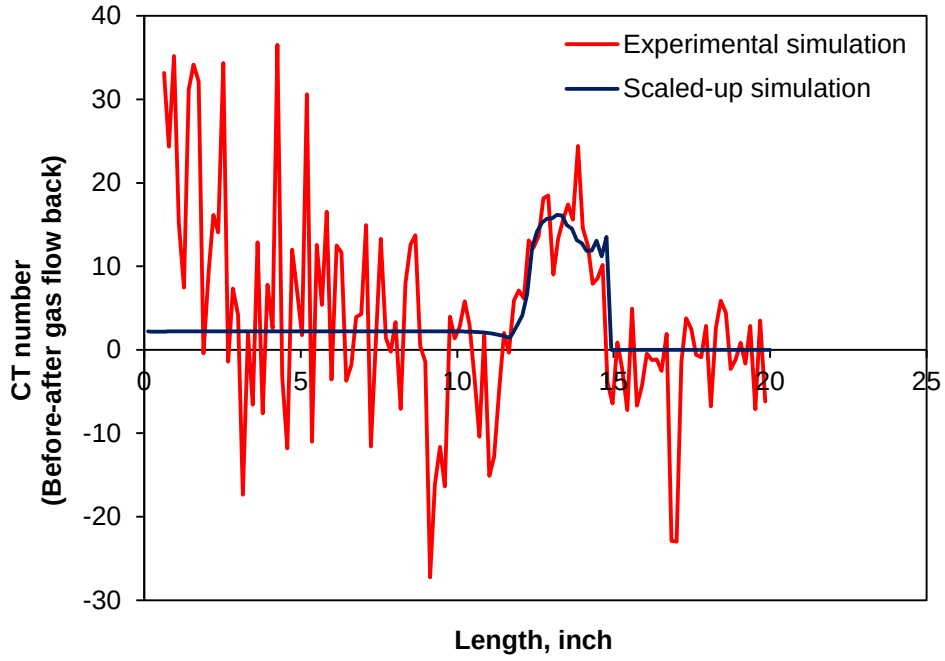

Fig. 2.13 Comparison between experimental and scaled-up simulations (Ind 12)

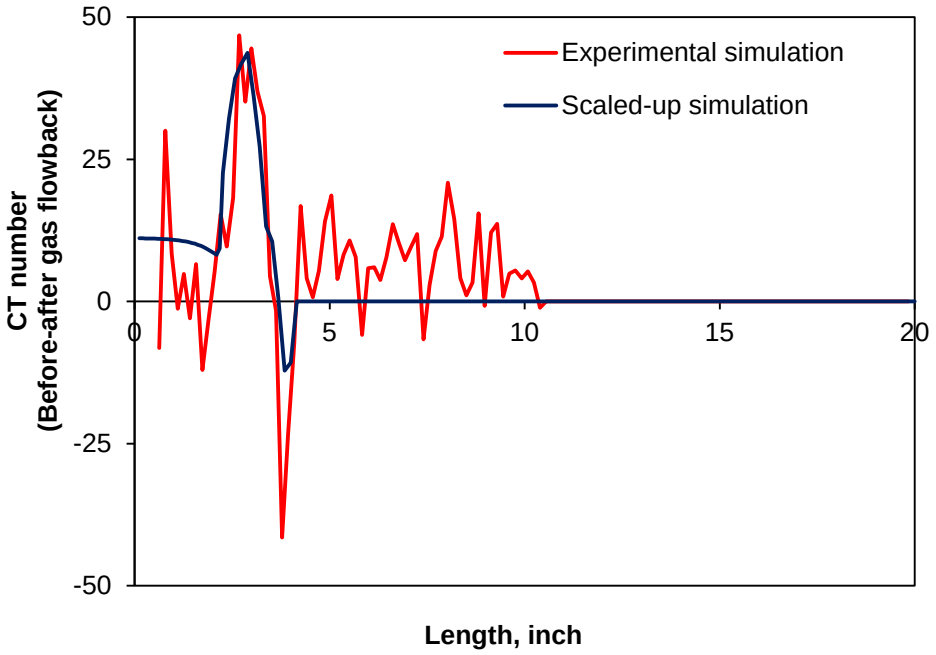

Fig. 2.14 Comparison between experimental and scaled-up simulations (TxCC 4)

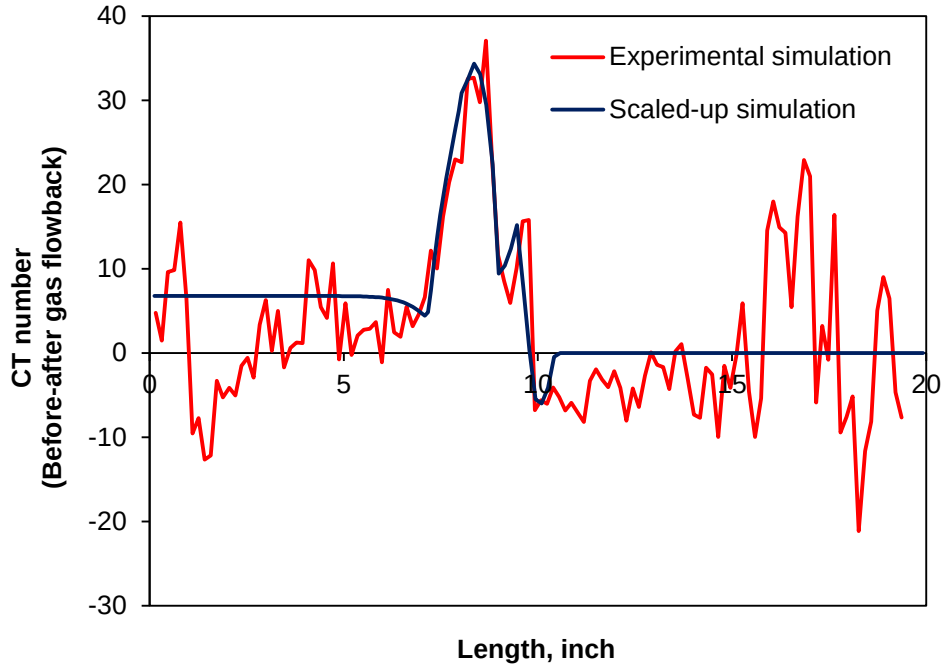

Fig. 2.15 Comparison between experimental and scaled-up simulations (TxCC 5)

For all the cases, by adjusting the relative permeability and capillary pressure function parameters, the scaled-up simulation results can match the experimental results approximately, especially around the wormhole tip region. If we look at the parameters in **Table 2.3**, we can find that the spent acid exponent n_{sp} is larger than the gas exponent n_{sp}, which means that without adding any additives, core Ind 9 stayed liquid wetting. Meanwhile, although iron control agents were added in core Ind 12 and TxCC 5, these two core samples remain liquid wetting as well. According to the existing study (Saneifar, 2011), the two iron control agents, HEDTA and GLDA, did not have significant effects on the spent acid surface tension. They did not have obvious impact on contact angle either when the concentration is 0.3 wt. %. The simulation results also show that the amount of ICA that is used in our acid treatment does not have a distinct effect on formation wettability.

In experiment TxCC4, the spent acid exponent n_{sp} is smaller than the gas exponent n_{sp} and it indicates that core TxCC 4 was changed to non-liquid wetting because of the introduction of corrosion inhibitor in the acid treatments. This phenomenon also corresponds with Saneifar's work (2011) that the addition of two kinds of corrosion inhibitors all resulted in smaller surface tensions. We will see in the subsequent analysis that non-liquid wetting formation is in fact favorable for spent acid recoveries. So it means that the use of corrosion inhibitors at a proper concentration will not harm the deliverability of gas wells and instead, it will probably help improve well deliverability.

2.4 Chapter Summary

In this section, a lab-scale acidizing treatment was designed and carried out on different types of core samples. Several common acid additives were added in the experiments and X-ray CT scan and 3-D image post-processing technologies were employed to visualize

the inner structures of the core plugs. These technologies also helped us find the spent acid distributions at different periods in the experiments.

A scaled-up numerical simulation was introduced to match experimental result, by adjusting relative permeability and capillary pressure function parameters. With the scaled-up simulations, we are able to obtain the information of the properties that cannot be measured from the experiments directly.

3. SPENT ACID FRONT TRACKING

3.1 Introduction

Numerical simulations have been performed by researchers to simulate water/spent acid recovery processes and quantify the effects of the blockage. Most of these studies were undertaken using either Cartesian or cylindrical coordinates. Kamath and Laroche (2003) mapped the water-blocking effect data to a radial wellbore model and made well deliverability predictions. Parekh and Sharma (2004) performed studies on cleanup of water blocks in depleted low-permeability reservoirs and a Cartesian grid system was used in their simulations. Mahadevan et al. (2007a, 2007b) presented a model to calculate the rate at which the water blocks get removed, for either fractured or unfractured gas wells. The model equations were formulated for a one dimensional system, thus it can only be used for linear or radial geometries. Bahrami et al. (2011) studied the effects of water blocking damage on flow efficiency and productivity in tight gas reservoirs. They built their reservoir model using 3-D Cartesian coordinates.

When the porous medium is homogeneous and isotropic, the flow will be radial or linear, depending on the shape of the boundary and it is reasonable to use Cartesian or cylindrical grid systems to represent those reservoirs. However, lack of homogeneity will distort the radial flow geometry (Kucuk and Brigham, 1979). In such conditions, special treatments need to be employed to increase the simulation accuracy. First it is common to see local grid refinements for complex geometries. In both Parekh and Sharma (2004) and Bahrami et al.'s (2011) work, the reservoir was divided into finer grid blocks along the fracture and also near the wellbore in order to capture the near-wellbore effects. Especially when coarse gridblocks are refined with a different type of grids, it generates a hybrid grid system (Collins et al, 1991). Another approach is to use a coordinate which better resembles the real field geometry. This approach has been employed by a number of preceding publications (Riley et al., 1991a; Liao and Lee, 1993; Blasingame et al.,

2007). Kucuk and Brigham (1979) stated that in the area surrounding a vertical fracture, an anisotropic formation, or an aquifer with an elliptical inner boundary, flow would be elliptical.

Acid treatment experiments have been performed mainly on small linear core samples. A typical wormhole metal casting from a linear coreflood experiment is presented in **Fig. 3.1** (Shukla et al., 2006). The casting usually includes a dominant wormhole and small branches. Nevertheless, the structure of the wormhole pattern changes when experimental condition changes. Investigations by McDuff et al. (2010a) presented geometric details of the 3-D wormhole structures formed in their large-scale acidizing treatments, as is shown in **Fig. 3.2**. In their experiment images, wormholes grew nearly symmetrically along the entire completion interval and wormhole branches were generated in all directions.

The geometric characteristic of the 3-D wormhole structure indicates that a model with only linear or simple radial flow could not fully resemble the real flow field geometry in the near wellbore region. Thus in this chapter, we present a simplified numerical model to simulate field wormholes. This model is based on the important features that were observed in 3-D acidizing treatments. Following that, mathematical descriptions of the coordinate that is used for this model is demonstrated. After applying material balance equations to the simplified model, the spent acid front right after the acid treatment is calculated and we will use them as the initial condition for the future spent acid/water blockage recovery numerical simulations.

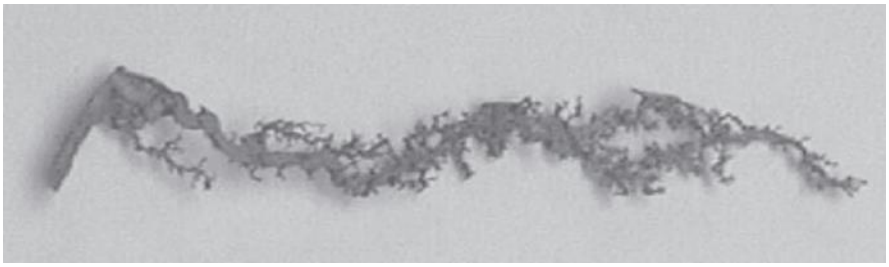

Fig. 3.1 Wormhole metal casting for linear coreflood experiments (Shukla et al., 2006)

Fig. 3.2 Top and side view of wormhole structures (McDuff et al., 2010b)

3.2 Physical Model Simplification

Valsecchi et al. (2012) performed detailed flow simulations of the rock near the wormhole structures following their large scale acid treatment experiments. The simulated streamlines for single-phase gas flow into a wormhole structure are shown in **Fig. 3.3**. The streamlines converge all along the length of the wormhole branches. According to the shape of the streamline curves in the figure, to a good approximation of the symmetry of the problem, we simplify the main part of a wormhole to half of a prolate ellipsoid, as illustrated in **Fig. 3.4**. In this simplified wormhole model, r_{wh} is the radius of the entry hole of the wormhole and D_{wh} is the wormhole penetration depth into the formation.

Mathematically, a prolate ellipsoid is a surface of revolution obtained by rotating an ellipse about its major axis and ellipsoidal coordinates could be utilized for such geometries. An ellipsoidal coordinate is an orthogonal curvilinear coordinate. The curvilinear coordinate has become more popular in recent years because it can eliminate the stagger grids in Cartesian coordinate system and improve the representation of the numerical models (Chau and Jiang, 2001). This type of coordinate is often adopted for problems with special boundary conditions, such as those arising in fluid flow, electrodynamics and the diffusion of chemical species or heat.

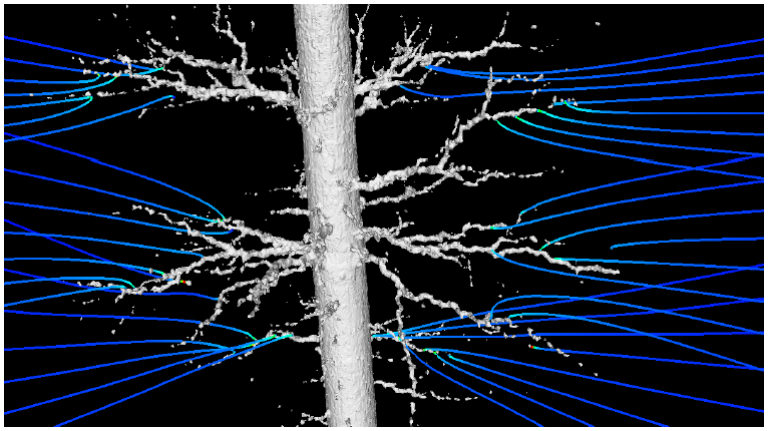

Fig. 3.3 CFD simulated streamlines into a wormhole structure (Valsecchi et al., 2012)

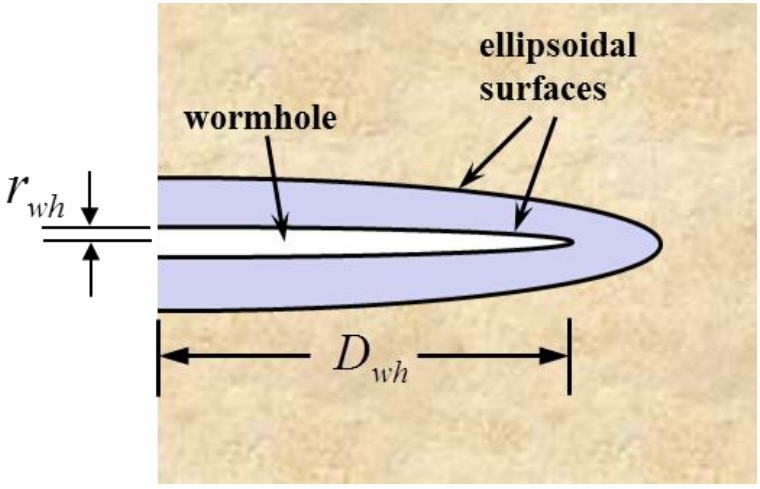

Fig. 3.4 Wormhole simplified to half of Prolate Spheroid

The left figure in **Fig. 3.5** shows the ellipsoidal coordinate system (ξ, η, ψ). The relationship between a rectangular coordinate and a prolate spheroidal coordinate is described below,

$$\begin{aligned} x &= H \sinh\xi \sin\eta \cos\psi \\ y &= H \sinh\xi \sin\eta \sin\psi \\ z &= H \cosh\xi \cos\psi \end{aligned} \quad \text{..... (3-1)}$$

where ξ is a nonnegative real number and $\eta \in [0, \pi]$. The azimuthal angle belongs to the interval $\psi \in [0, 2\pi)$.

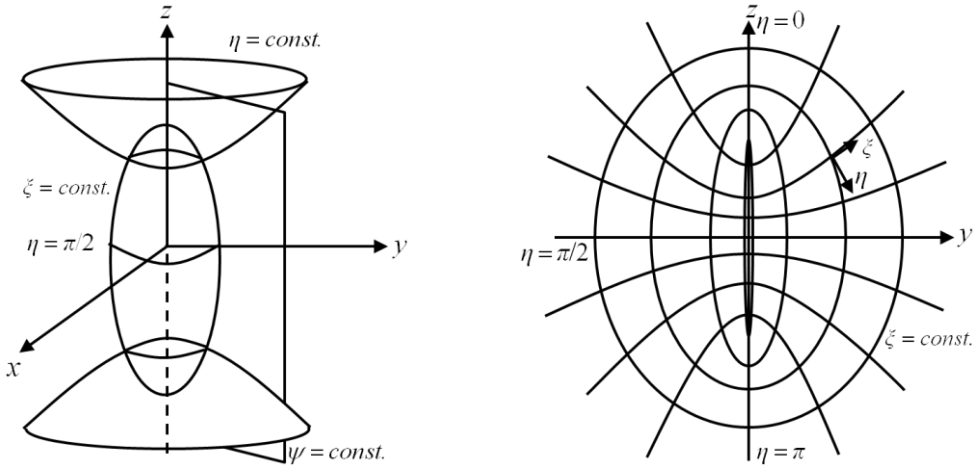

Fig. 3.5 Ellipsoidal and elliptical coordinates

Since prolate spheroid has a rotational symmetry, it can be further simplified into an elliptical coordinate system by considering azimuthal angle ψ as a constant. Accordingly the relationship between Cartesian and elliptical coordinates can be written in Eq. 3-2.

$$\begin{aligned} y &= H \sinh\xi \sin\eta \\ z &= H \cosh\xi \cos\eta \end{aligned} \quad \text{..... (3-2)}$$

The right figure in **Fig. 3.5** presents an illustration of the elliptical coordinates. It can be seen that the elliptical coordinate system consists of a family of ellipses and a

family of hyperbolas. The hyperbolas are labeled for various values of η from 0 to 2π and play a role similar to the angular coordinate. The ellipses are labeled for various values of ξ starting from 0. In this system ξ plays a role similar to the radial coordinate. As ξ increases, the ellipses resemble circles and the hyperbolas become radii of these circles (Riley, 1991b). The two constants that define the shape of the wormhole in an elliptical coordinate are H and ξ_{wh}. Their values can be expressed in terms of r_{wh} and D_{wh} with the following equation (Schechter, 1992),

$$\begin{aligned} r_{wh} &= H \sinh \xi_{wh} \\ D_{wh} &= H \cosh \xi_{wh} \end{aligned} \quad \text{..... (3-3)}$$

When partial differential equations are used to formulate problems involving functions of several variables under elliptical coordinates, we will need to deal with the transformation of differential quantities, such as arc-length and the Laplacian. These transformations can be achieved by using the conventional coordinate transformation methods which employ the scale factors, h_η and h_ξ. The scale factors measure the ratio of the infinitesimal element of arc-length in the new coordinate system to that in the Cartesian system. In elliptical coordinates the two scale factors are equal and can be expressed as (Riley, 1991b):

$$\begin{aligned} h_\xi &= H\sqrt{\sinh^2\xi + \sin^2\eta} \\ h_\eta &= H\sqrt{\sinh^2\xi + \sin^2\eta} \end{aligned} \quad \text{..... (3-4)}$$

Using the scale factors, we can immediately transform the arc-length and Laplacian from Cartesian to elliptical coordinates. If we consider arc-length to be a vector, its differential element is given by:

$$d\vec{s} = dx\vec{e}_x + dy\vec{e}_y = h_\xi d\xi \vec{e}_\xi + h_\eta d\eta \vec{e}_\eta = H\sqrt{\sinh^2\xi + \sin^2\eta}\left(d\xi\vec{e}_\xi + d\eta\vec{e}_\eta\right) \text{..... (3-5)}$$

The two-dimensional Laplacian of a quantity, Φ, is given by the expression:

$$\nabla^2\Phi = \frac{1}{H^2\left(\sinh^2\xi + \sin^2\eta\right)}\left(\frac{\partial^2\Phi}{\partial\xi^2} + \frac{\partial^2\Phi}{\partial\eta^2}\right) \quad \text{..... (3-6)}$$

In addition to the simplifications, several assumptions are made for the following simulations. Since a wormhole is highly conductive, the pressure drop associated with flow within the wormholes can be neglected. Thus within the interior of the wormholes, the pressure is assumed to be constant and equal to p_w, the pressure in the wellbore or the drawdown pressure. Far from the entry point, the fluid pressure is considered as the reservoir pressure P_R. We also assume the distance between each wormhole is large enough, so that the wormhole will be productive over its entire surface and the influence that all the other wormholes might have on its pressure distribution can be neglected.

3.3 Spent Acid Front Track

3.3.1 Spent acid balance equation

Before proceeding to a comprehensive spent acid/water recovery study, we need to find out how deep spent acid/water invades into the formation during the acid treatments. The wormhole generation and spent acid penetration process is complicated and it is not the emphasis for this work. In this study we assume that the wormholing procedures has already ended and resulted in slender elliptical shaped wormholes before spent acid invades. Correspondingly, we also assume acid is consumed completely, that is without considering reaction term in the spent acid balance equations. Based on these assumptions, the following calculations will give us approximate spent acid distribution profiles around wormholes.

We consider a small volume element $w^2\Delta x$ as shown in **Fig. 3.6**. Without considering reaction, the spent acid balance equation about this small element over a small period of time (Δt) yields (Schechter, 1992),

$$\Delta t\, w^2 uc\big|_x - \Delta t\, w^2 uc\big|_{x+\Delta x} = \left[c\phi\big|_{t+\Delta t} - c\phi\big|_t\right] w^2 \Delta x \quad \text{..... (3-7)}$$

where u is the spent acid flux and c is the ion concentration of the spent acid. Dividing by $w^2 \Delta x\, \Delta t$ and taking the limit as Δx and Δt both approach zero, the spent acid balance for a linear system is obtained,

$$\frac{\partial}{\partial t}(c\phi) + u_x \frac{\partial c}{\partial x} = 0 \quad \text{..... (3-8)}$$

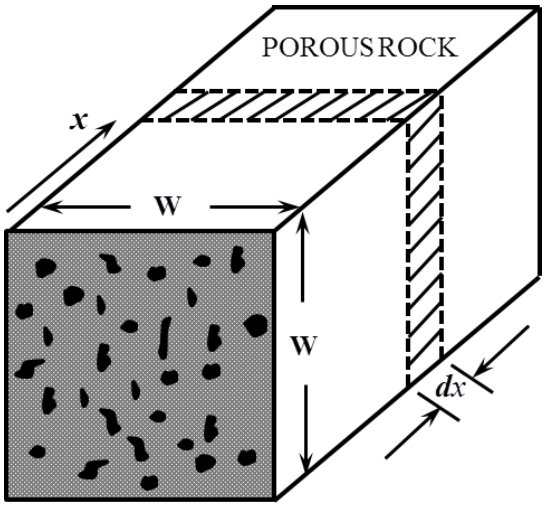

Fig. 3.6 Spent acid front at different time

In a linear flow, the flux (u) in Eqn. 3-8 is a constant. During an acidizing treatment, we are be able to hold the injection rate (i_{wh}) as a constant. However, the flux along the wormhole will not be constant anymore when a wormhole is simplified as half of a slender ellipsoidal surface. Under an elliptical coordinate, the surfaces of constant ξ are also the surfaces of constant pressures. The flux u_ξ is, therefore, perpendicular to surfaces of constant ξ . It can be shown that (Schechter, 1992),

$$u_\xi = \frac{i_{wh}}{2\pi H^2 \sinh\xi}\left[\frac{1}{\cosh^2\xi - \cos^2\eta}\right]^{1/2} \quad \text{..... (3-9)}$$

The above equation shows that although the flux is perpendicular to the surfaces of constant ξ, its magnitude, on the other hand, depends on its position on the wormhole surface. Thus some portion of the wormhole surface will receive larger amounts of acid than the others. With substitution of this flux expression into Eq. 3-8, the acid balance equation can be rewritten as,

$$\phi_0 \frac{\partial c_{sp}}{\partial t} + \frac{i_{wh}}{2\pi H^3 \sinh\xi}\left[\frac{1}{\cosh^2\xi - \cos^2\eta}\right]\frac{\partial c_{sp}}{\partial \xi} = 0 \quad \text{..... (3-10)}$$

To solve this equation, it is convenient to define a dimensionless distance and a dimensionless time, which are expressed in the following equations,

$$\begin{aligned} \varepsilon &= \left(\frac{1}{3}\cosh^3\xi - \cos^2\eta\cosh\xi\right) - \left(\frac{1}{3}\cosh^3\xi_{wh} - \cos^2\eta\cosh\xi_{wh}\right) \\ \theta &= \frac{t i_{wh}}{2\pi H^3 \phi_0} \end{aligned} \quad \text{..... (3-11)}$$

where the subscript wh is intended to denote values specifically related to the geometry of a wormhole. Substituting these dimensionless groups, Eq. 3-10 can be written in a much simpler form,

$$\frac{\partial c_{sp}}{\partial \theta} + \frac{\partial c_{sp}}{\partial \varepsilon} = 0 \quad \text{..... (3-12)}$$

With boundary and initial conditions,

$$c_{sp}(0,\theta) = f_1(\theta) = c_{sp}^0, \ \theta > 0 \quad \text{..... (3-13)}$$

$$c_{sp}(\varepsilon,0) = f_2(\varepsilon) = \begin{cases} c_{sp}^0, & \varepsilon = 0 \\ 0, & \varepsilon > 0 \end{cases} \quad \text{..... (3-14)}$$

3.3.2 Method of characteristics

Eq. 3-12 is a linear convection equation. Generally the linear convection equation has the following form,

$$\begin{cases} \dfrac{\partial u(x,t)}{\partial t} + a\dfrac{\partial u(x,t)}{\partial x} = 0 \quad (a = const) \\ u\big|_{t=0} = f(x) \end{cases} \quad \text{..... (3-15)}$$

Mathematically Eq. 3-15 is a first order hyperbolic partial differential equation and it is characterized by information propagation along certain preferred directions. Now we use the method of characteristics to find the solution of Eq. 3-15 at a time $t > 0$. The method of characteristics uses special curves in the $x-t$ plane along which the partial differential equation (PDE) becomes an ordinary differential equation (ODE) (Hoffman and Frankel, 2001). In the $x-t$ plane, the characteristic curve of the Eq. 3-15 is,

$$\begin{cases} \dfrac{dx}{dt} = a \\ x(0) = c \end{cases} \quad \text{..... (3-16)}$$

The solution of this characteristic curve is $x(t) = at + c$. Let $U(t) = u(x(t),t)$, the rate of change of $U(t)$ along this curve is given by $\dfrac{d}{dt}U(t)$. Using chain rule, we can write,

$$\frac{dU(t)}{dt} = \frac{d}{dt}u\big(x(t),t\big) = \frac{\partial}{\partial x}u\big(x(t),t\big)\frac{dx}{dt} + \frac{\partial}{\partial t}u\big(x(t),t\big) = a\frac{\partial u(x,t)}{\partial x} + \frac{\partial u(x,t)}{\partial t} \quad \text{..... (3-17)}$$

The right hand side of Eq. 3-17 is the same as the left hand side of the linear convection equation Eq. 3-15. Therefore the original problem becomes,

$$\begin{cases} \dfrac{dU(t)}{dt} = 0 \\ U(0) = u(x(0),0) = u(c,0) = f(c) \end{cases} \quad \text{..... (3-18)}$$

In the above equation, the PDE Eq. 3-15 becomes an ODE along the characteristic. The solution to this ordinary differential equation is simply $U(t) = \text{constant}$ and it can be illustrated with **Fig. 3.7**. In the figure, the physical property is propagated along the characteristic with an unchanged magnitude and shape.

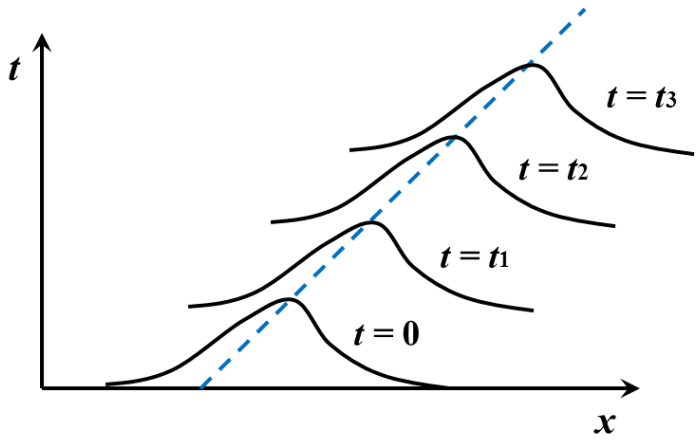

Fig. 3.7 Illustration of analytical solution

Thus when we know the solution at the foot of the characteristic (at x_0), which is the initial condition, we can get the solution anywhere on the characteristic and it is $U(t) = f(c)$. From the characteristic curve, we know that $c = x(t) - at$, and substitutes of c into $U(t)$, we get the analytical solution of the convection equation Eq. 3-15,

$$u(x,t) = f(x-at) \quad \text{..... (3-19)}$$

Now applying this analytical solution to the equations Eq. 12 through Eq. 14, we will have the following spent acid profile,

$$c_{sp}(\varepsilon,\theta) = f_2(\varepsilon-\theta) = \begin{cases} c_{sp}^0, & \varepsilon-\theta = 0 \\ 0, & \varepsilon-\theta > 0 \end{cases} \quad \text{..... (3-20)}$$

From Eq. 3-20, we know that at point $\varepsilon = \theta$, the spent acid has a distribution as the initial distribution; at any point $\varepsilon > \theta$, there is no spent acid invasion. It means the expression $\varepsilon = \theta$ actually determines the location of the spent acid front. Since the functions of ε and θ are monotonic (Eq. 3-11), the results from this expression can be mapped back to elliptical coordinates directly, as demonstrated in Eq. 3-21.

$$\left(\frac{1}{3}\cosh^3\xi - \cos^2\eta\cosh\xi\right) - \left(\frac{1}{3}\cosh^3\xi_{wh} - \cos^2\eta\cosh\xi_{wh}\right) = \frac{ti_{wh}}{2\pi H^3\phi_0} \quad \text{..... (3-21)}$$

In the above equation, at a specific injection time t, we need to solve series of cubic equations of variable ξ with different η values. The solution details are listed in **APPENDIX B**. The solution from Eq. 3-21 will give us the spent acid distribution for the whole region surrounding the wormholes.

3.4 Spent Acid Front Results

Based on the above analysis, we present spent acid front results in this part. To calculate the spent acid front, we assume there are 6 wormholes/ft from acid treatments. The wormholes have the following average dimensions: the radius of wormhole, $r_{wh} = 0.1\,inch$ and the length of the wormhole, $D_{wh} = 59\,inches$, which results in $H = 59.05\,inches$ and $\xi_{wh} = 0.02\,inch$ in Eq. 3-21. We also assume the formation is homogenous and the acid injection rate into each wormhole is about 0.2gal/ft/min. The injection lasts for an hour, which results in 72 gal/ft for the entire treatment.

Fig. 3.8 presents the wormhole and the spent acid front profiles at different injection times. In the calculation, the formation porosity is set to 0.15. From the figure, we can see that spent acid front penetration rate is the highest in the first 1200 seconds. However, in the second and the third 1200 secs, the spent acid front rate keeps decreasing. This is because the matrix volume involved in spent acid spreading is increasing.

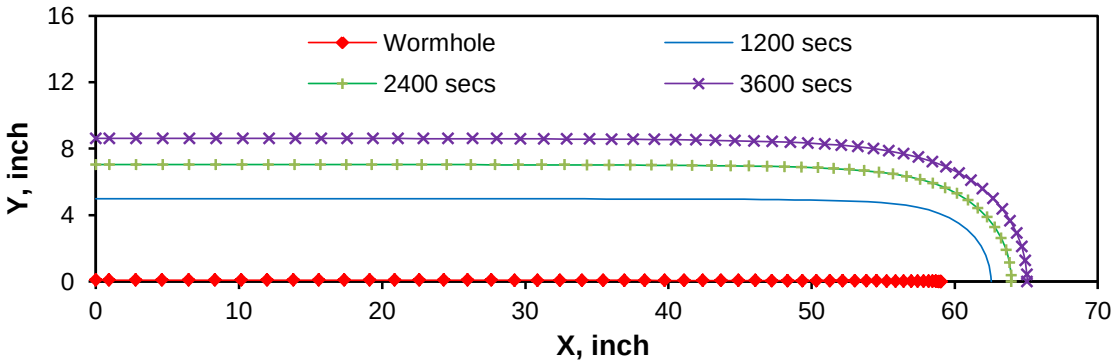

Fig. 3.8 Spent acid front at different injection times

In **Fig. 3.9**, we show the spent acid front profiles in formations with different porosities (0.05, 0.15 and 0.25) with a total injection time of one hour (3600 secs). According to the result, when porosity decreases from 0.25 down to 0.15, the spent acid front moves deeper into the reservoir since less pore space exists in the matrix. However, when formation porosity decreases from 0.15 to 0.05, the spent acid front moves much farther into the formation even with the same amount change of porosity. That means for a formation with an extreme low porosity, we will expect a farther spent acid front and thus probably a more severe spent acid blockage problem.

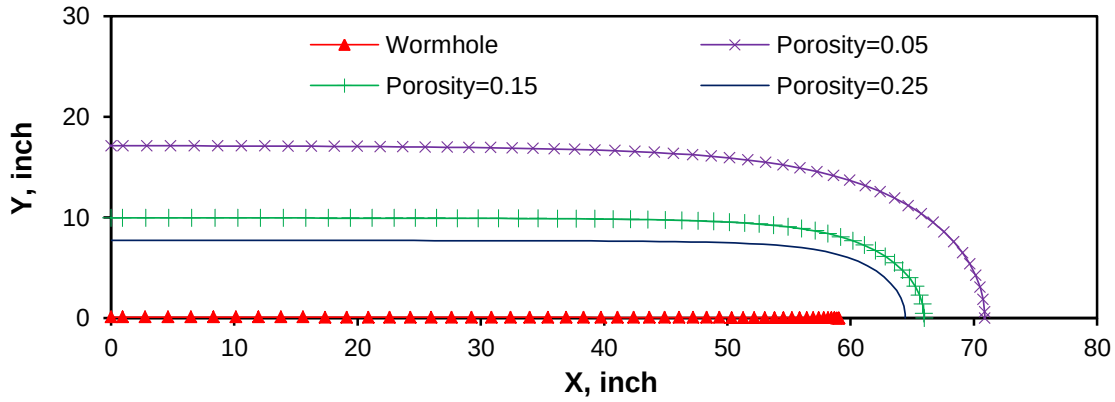

Fig. 3.9 Spent acid front with different porosity

Next we consider a synthetic extreme case in which the formation has fairly low porosity yet relative high permeability. It is not a common case in the real field, but similar situation was reported in existing studies (as cited in Ma and Morrow, 1996). We keep the acid treatment pressure constant when we compare this extreme case with a normal one. Obviously, the resulting injection rate for the extreme case will be much higher because of the high permeability. In the calculation for **Fig. 3.10**, the permeability of the extreme case is 4 times larger than the normal case, but the porosity is only 1/5 of the normal formation. From the figure we can see that spent acid penetrates much deeper in the extreme case and this spent acid has a strong likelihood to cause severe formation damages. The above simulation results also show that the formation properties have great impacts on spent acid invasion process. It is very important for us to find out the critical properties before any acid stimulation.

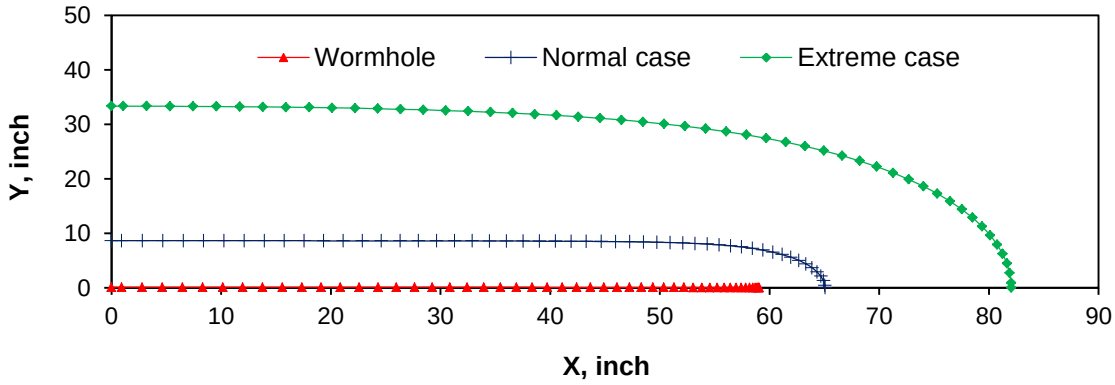

Fig. 3.10 Illustration of spent acid penetration for normal and extreme cases

3.5 Chapter Summary

In this chapter, we simplified the real field wormhole into half of a prolate ellipsoid. The elliptical coordinate that is used for the simplified model is described and the transformations between Cartesian and elliptical coordinates are also presented. Then the spent acid balance equation is described and simplified under elliptical coordinates. To

solve the spent acid balance equation, the method of characteristics is introduced. The spent acid front results presented in this chapter will serve as boundary conditions in subsequent numerical simulations.

4. NUMERICAL MODELS

4.1 Introduction

It was discovered by Kamath and Laroche (2000) that in spent acid/water cleanup processes, gas deliverability recovered is in two phases. The first phase corresponds to the liquid production on well flow back. The second phase corresponds to the evaporation of the water-block region with continued gas flow. Mahadeven and Sharma (2003b) added methanol in some of their core-flood experiments. When comparing the results from these experiments with those without additives, it was easy to identify the displacement and evaporation regimes since the increased volatility of methanol resulted in a significantly better cleanup during the evaporation part. Their experimental results also showed that these two regimes happened at totally different rates. The displacement phase happens rapidly and usually ends in the first 50 pore volumes (PV) or so, whereas the evaporation phase is relatively slow and could last for a much longer period. In some cases increased gas relative permeability can still be observed even after 10,000 PVs. According to their experimental results, only part of the gas relative permeability was recovered in the displacement part and the evaporation regime continued to play a significant role afterwards.

Since evaporation is important in gas relative permeability recovery, especially in tight gas reservoirs, a large number of numerical studies have tried to involve evaporation in their simulations (Bette and Heinemann, 1989; Kurihara et al., 2000; Humphreys, 1991; Zuluaga and Lake, 2008; Mahadevan et al., 2007b; Bazin et al., 2010). Among these studies, the simulation based on the modified equation of state compositional model treated water as a component among other species in the hydrocarbon phases and allowed for mass transfer between the aqueous phase and the hydrocarbon phases (Bette and Heinemann, 1989; Kurihara et al., 2000). This is a physically founded method and is versatile in application. However compositional simulations are more complicated and

time-consuming when comparing to conventional black-oil models, and thus efforts have been made to find an intermediate approach between black-oil and compositional models.

Spivak and Dixon (1973) introduced a modification to a conventional black-oil model and employed it in gas-condensate reservoir simulations. This method is called modified black-oil (MBO) or extended black-oil model. The MBO simulation considers three components (dry gas, oil and water). The main difference between the conventional black-oil simulation and the MBO simulation lies in the treatment of the liquid in the gas phase. The MBO approach assumes that stock-tank liquid components can exist in both liquid and gas phases under reservoir conditions. It also assumes that the liquid content of the gas phase can be defined as a sole function of pressure called vaporized oil-gas ratio, R_V. This function is similar to the solution gas-oil ratio, R_s, normally used to describe the amount of gas-in-solution in the liquid phase (El-Banbi et al., 2006).

Several authors have shown the applicability of the modified black oil (MBO) approach for modeling gas condensate and volatile oil reservoirs. Coats (1985) presented a pseudoization procedure that reduces the multicomponent condensate fluid to a pseudo two-component mixture of surface gas and oil and used the modified black-oil model for the simulations. His results showed that modified black-oil simulation gave very similar results compared with fully compositional models for depletions. In addition, the two models also give identical results for cycling above the dewpoint provided that certain conditions are satisfied. El-Banbi et al. (2000a, 2000b) made a comparison between modified black-oil and compositional model simulations in a full field study for a rich gas condensate reservoir with complex fluid behavior. The two models agreed for the entire simulation above and below the dew point. Their study showed that a MBO approach can be used instead of a fully compositional approach for modeling depletion and water influx processes in near-critical reservoirs.

In this study, in order to handle the water evaporation phenomenon, we borrow the idea from the modified black oil model and introduce a vaporized spent acid/water-gas

ratio, R_V in our simulations. For the rest of this chapter, we will present the details of the model first and then give a brief description of the fully implicit scheme. Subsequently, the validations of the model are provided at the end.

4.2 Spent Acid Recovery Model

4.2.1 Controlling equations

In a modified black oil model, the effect of oil volatility is included by employing the vaporized oil-gas ratio. Similarly, in this simulation we introduce a vaporized spent acid-gas ratio, R_V . Thus, there will be spent acid and gas components in the model. In addition, vaporization of spent acid into the gas phase is allowed, that is the spent acid can exist in both liquid and gas phases. Besides, since gas component is usually assumed to be soluble in oil but not in water at reservoir simulations, we do not consider any gas component in the liquid phase in this study.

To establish the spent acid recovery model, certain physical principles must be followed in order to satisfy the conditions of reservoir fluid flow. These three fundamental relationships are: 1 the continuity equations (differential mass balance); 2 flow rate equations (for example, Darcy's Law); 3 an equation of state (mathematical description of the pressure/volume/temperature (PVT) behavior of the flowing fluid) (Ertekin et al., 2001).

The continuity equation expresses the conservation of mass,

$$\frac{\partial}{\partial t}\left(\rho_i S_i \phi\right) = -\nabla \cdot \left(\rho_i \bar{u}_i\right) + q_i \quad \text{..... (4-1)}$$

where i represents the i^{th} component. Introducing formation volume factors, the continuity equations for gas and spent acid can be expressed respectively by the following equations,

$$\frac{\partial}{\partial t}\left[\frac{\phi\rho_{g,s}}{B_g}S_g\right] = -\vec{\nabla}\cdot\left(\frac{\rho_{g,s}}{B_g}\vec{u}_g\right) + q_g \quad \text{..... (4-2)}$$

$$\frac{\partial}{\partial t}\left[\frac{\phi\rho_{sp,s}}{B_{sp}}S_{sp} + \frac{\phi R_V\rho_{sp,s}}{B_g}S_g\right] = -\vec{\nabla}\cdot\left(\frac{\rho_{sp,s}}{B_{sp}}\vec{u}_{sp} + \frac{R_V\rho_{sp,s}}{B_g}\vec{u}_g\right) + q_{sp} \quad \text{..... (4-3)}$$

Note that the second term on both sides of the spent acid mass conservation equation accounts for the spent acid being transported in the vapor phase.

Darcy's law gives the volumetric flow at a point for each phase in terms of the potential gradient. For multi-phase flow the extended form of Darcy's law for each phase can be expressed as,

$$\vec{u}_i = -\beta_c\frac{kk_{ri}}{\mu_i}\left(\vec{\nabla}p_i - \gamma_i\vec{\nabla}Z\right) \quad \text{..... (4-4)}$$

where $i = sp$ or g and k_{ri}, μ_i, p_i, and γ_i = relative permeability, viscosity, pressure, and fluid gravity for phase i, respectively. β_c = unit conversion factor for the transmissibility coefficient.

The phase-saturation equation, which is a constraint on the sum of phase saturation, is,

$$S_{sp} + S_g = 1 \quad \text{..... (4-5)}$$

and the gas/spent acid capillary pressure relationship is

$$p_c = p_g - p_{sp} = f\left(S_{sp}\right) \quad \text{..... (4-6)}$$

These equations contain four unknowns, p_g, p_{sp}, S_g and S_{sp}. The relationships expressed by Eqs. 4-5 and 4-6 can be used to eliminate two unknowns in the flow equations. Throughout this study, the formulation that uses gas pressure, p_g, and spent acid saturation, S_{sp}, is employed. The resulting two equations with two principal unknowns are listed below,

$$\frac{\partial}{\partial t}\left[\frac{\phi\rho_{g,s}}{B_g}S_g\right]=\vec{\nabla}\cdot\left(\beta_c\frac{\rho_{g,s}}{B_g}\frac{kk_{rg}}{\mu_g}\vec{\nabla}p_g\right)+q_g \quad \text{..... (4-7)}$$

$$\frac{\partial}{\partial t}\left[\frac{\phi\rho_{sp,s}}{B_{sp}}S_{sp}+\frac{\phi R_V\rho_{sp,s}}{B_g}\left(1-S_{sp}\right)\right] = \vec{\nabla}\cdot\left(\beta_c\frac{\rho_{sp,s}}{B_{sp}}\frac{kk_{rsp}}{\mu_{sp}}\vec{\nabla}\left(p_g-p_c\right)+\beta_c\frac{R_V\rho_{sp,s}}{B_g}\frac{kk_{rg}}{\mu_g}\vec{\nabla}p_g\right)+q_{sp} \quad \text{..... (4-8)}$$

Eq. 4-7 and Eq. 4-8 constitute the gas/spent acid flow model, among which, the liquid content, R_V, can be either a function of pressure or an unknown (i.e., primary dependent variable). If spent acid is present at a point, then the liquid spent acid and vapor phases are in equilibrium and R_V can be determined from the equilibrium calculation. If spent acid is not present in the form of a liquid phase, it can still be transported in the vapor phase and the spent acid content at that point must be determined by continuity or mass balance (Spivak and Dixon, 1973).

4.2.2 Fluid characterizations

A key factor in successfully using the modified black-oil model is to utilize the appropriate fluid characterizations which can represent the compositional phenomena adequately. In this study, the PVT functions of the modified black-oil simulation and material balance calculations are: spent acid-gas ratio, R_V; spent acid formation volume factor, B_{sp}; and gas formation volume factor, B_g.

Calculation of those PVT functions involves mass transfer between the liquid and vapor phases and it is usually accounted for by the equilibrium liquid content vs. pressure curve, which is provided by the laboratory tests (Spivak and Dixon, 1973). In the subsequent simulations, we assume spent acid is mainly composed of water (H_2O) and the hydrocarbon component is methane (CH_4). That is, we will simulate a hydrocarbon-water system. The investigations of mass transfer for such system have been performed in

numerous studies (Culberson and McKetta, Jr., 1951; Rigby and Prausnitz, 1968; Wagner and Pruss, 1993; Duan and Mao, 2006; Yarrison et al., 2006). In these studies, both solubility of hydrocarbon in water and water content in hydrocarbon mixtures were measured or modeled. In this work, we choose several existing correlations to estimate spent acid content in the gas phase.

Similar to the definition of dissolved gas-oil ratio, the spent acid-gas ratio is the volume of spent acid (measured at standard condition) vaporized at a given pressure and temperature into a volume of standard cubic feet of gas:

$$R_V(p,T) = \frac{V_{sp,s}}{V_{g,s}} \quad \text{(4-9)}$$

where $V_{sp,s}$ and $V_{g,s}$ are the vaporized spent acid and gas volumes measured at standard conditions. Also note that,

$$V_{sp,s} = \frac{W_{sp}}{\rho_{sp,s}}, V_{g,s} = \frac{W_g}{\rho_{g,s}} \quad \text{(4-10)}$$

where W_{sp} and W_g are the weights of the vaporized spent acid and gas components. $\rho_{sp,s}$ and $\rho_{g,s}$ are the spent acid and gas densities measured at standard conditions, respectively. Thus Eq. 4-9 becomes,

$$R_V(p,T) = \frac{W_{sp}/\rho_{sp,s}}{W_g/\rho_{g,s}} = \frac{y_{sp}\cdot M_{sp}/\rho_{sp,s}}{y_g \cdot M_g/\rho_{g,s}} \quad \text{(4-11)}$$

$$y_g = 1 - y_{sp} \quad \text{(4-12)}$$

In Eq. 4-11, the mole fraction of spent acid, y_{sp} in the gas phase is needed in order to calculate R_V. Since we assume a hydrocarbon-water (CH_4-H_2O) system, y_{sp} can be estimated using the following semi-empirical equation (Duan and Mao, 2006),

$$y_{sp} = \frac{x_{sp} p_{sp}^{S}}{\varphi_{sp} p} \exp\left(\frac{v_{sp}^{l}(p - p_{sp}^{S})}{RT} \right) \quad \text{..... (4-13)}$$

where x_{sp} is the mole fraction of spent acid in the liquid, and is approximated as 1 for CH_4-H_2O system; p_{sp}^{S} is the saturation pressure (bar) and the present study employs Wagner and Pruss (1993) equation, which was proposed based on the critical pressure and temperature and can be written as follows.

$$\ln\left(\frac{p}{p_{critical}} \right) = \frac{1}{T_R}\left[a_1\tau + a_2\tau^{1.5} + a_3\tau^{3} + a_4\tau^{3.5} + a_5\tau^{4} + a_6\tau^{7.5} \right] \quad \text{..... (4-14)}$$

$$\tau = 1 - T / T_{critical} \quad \text{..... (4-15)}$$

$$a_1 = -7.85951783, \qquad a_2 = 1.84408259, \qquad a_3 = -11.7866497,$$
$$a_4 = 22.6807411, \qquad a_5 = -15.9618719, \qquad a_6 = 1.80122502$$

where $p_{critical}$ and $T_{critical}$ stand for the critical pressure and critical temperature of spent acid, respectively, and T_R is the reduced temperature ($T / T_{critical}$). The critical pressure and temperature are 22.064 *MPa* and 647.096 *K*, respectively (Shibue, 2003).

v_{sp}^{l}, molar volume of liquid spent acid, approximates saturated liquid phase volume of spent acid and it can be calculated providing the saturated liquid density ρ' described by Eq. 4-16.

$$\frac{\rho'}{\rho_{critical}} = 1 + b_1\tau^{1/3} + b_2\tau^{2/3} + b_3\tau^{5/3} + b_4\tau^{16/3} + b_5\tau^{43/3} + b_6\tau^{110/3} \quad \text{..... (4-16)}$$

$$b_1 = 1.99274064, \qquad b_2 = 1.09965342, \qquad b_3 = -0.510839303,$$
$$b_4 = -1.75493479, \qquad b_5 = -45.5170352, \qquad b_6 = -6.74694450e5$$

where $\rho_{critical}$ equals $322\, kg/m^3$. Another parameter in Eq. 4-13 for the calculation of spent acid content in the gas phase is the fugacity coefficient of spent acid in the gas phase (φ_{sp}). It can be calculated from the following equation (Duan and Mao, 2006),

$$\varphi_{sp} = \exp\left(c_1 + c_2 p + c_3 p^2 + c_4 pT + c_5 p/T + c_6 p^2/T\right) \quad \text{(4-17)}$$

$c_1 = -1.42006707e-2,$ $c_2 = 1.08369910e-2,$ $c_3 = -1.59213160e-6,$
$c_4 = -1.10804676e-5,$ $c_5 = -3.14287155,$ $c_6 = 1.06338095e-3$

In **Fig. 4.1**, a demonstration of spent acid content in gas phase calculated from the above equations at different pressures and temperatures is shown.

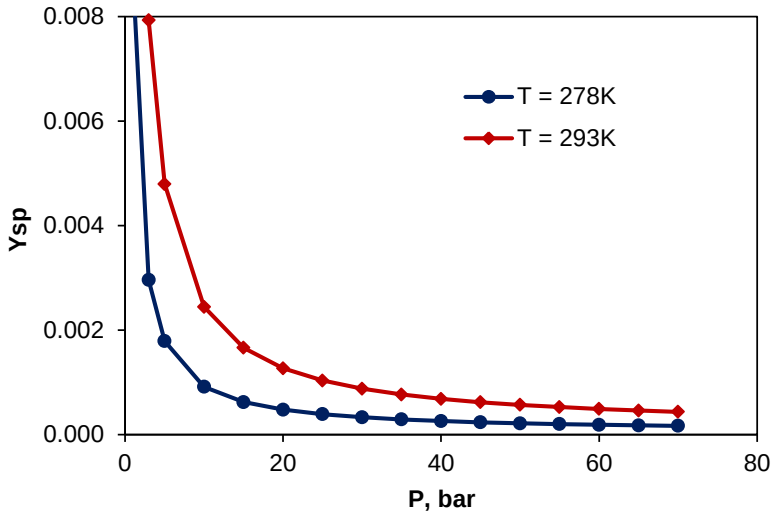

Fig. 4.1 The prediction of spent acid content in the gas phase

From the definition of fluid compressibility,

$$c = -\frac{1}{V}\frac{\partial V}{\partial p}\bigg|_T = \frac{1}{\rho}\frac{\partial \rho}{\partial p}\bigg|_T \quad \text{(4-18)}$$

and the definition of reservoir fluid formation volume factor,

$$B = \frac{V}{V_{sc}} = \frac{\rho_{sc}}{\rho} \quad \text{(4-19)}$$

the following equation can be derived to calculate spent acid formation volume factor, B_{sp},

$$B_{sp}\big|_{p} = \frac{B_{sp}\big|_{p_{ref}}}{1+g+g^2/2} \quad \text{..... (4-20)}$$

where $g = c_{sp}\left(p - p_{ref}\right)$, c_{sp} is the spent acid compressibility and p_{ref} is reference pressure. $B_{sp}\big|_{p_{ref}}$ is the spent acid formation factor at the reference pressure.

Besides, spent acid viscosity is computed as,

$$\mu_{sp}\big|_{p} = \mu_{sp}\big|_{p_{ref}} / \left[1 - c_{\mu}\left(p - p_{ref}\right)\right] \quad \text{..... (4-21)}$$

where c_{μ} is the fractional change of water viscosity per unit change of pressure.

As for gas formation volume factor B_g and viscosity μ_g, we use existing data from the literature (Schlumberger, 2011) and table look-up is employed in the following simulations.

4.2.3 Finite difference discretization and fully implicit scheme

The continuous partial differential equations describing the spent acid-gas flow in porous media shown in the previous section are strongly nonlinear. In some cases, where further simplification can be made, the PDEs can be solved with analytical techniques. However, for most 'real world' applications, such as the problem in this study, this becomes a daunting, if not impossible, task. Thus, we use the popular finite different technique to solve the PDEs.

In **Fig. 4.2**, the grids that are used in this study are presented. We use the same notations ξ and η for the coordinates, as was used in Chapter 3. Before discretization of the PDEs, Eq. 4-7 and Eq. 4-8 are expressed under elliptical coordinates first. By using Eq. 3-4 through Eq. 3-6, the flow equations for gas and spent acid can be expressed by the following two equations.

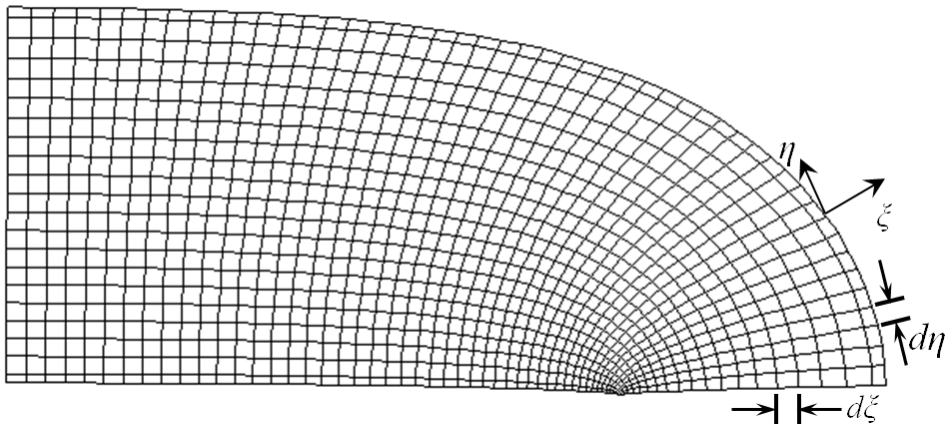

Fig. 4.2 Grids of the simulation region

For gas,

$$\frac{V_b}{\alpha_c}\frac{\partial}{\partial t}\left(\frac{\phi S_g}{B_g}\right)=\frac{1}{h_\eta^2}\frac{\partial}{\partial\eta}\left[\beta_c\frac{k_\eta k_{rg}A_\eta}{\mu_g B_g}\frac{\partial p_g}{\partial\eta}\right]\Delta\eta+\frac{1}{h_\xi^2}\frac{\partial}{\partial\xi}\left[\beta_c\frac{k_\xi k_{rg}A_\xi}{\mu_g B_g}\frac{\partial p_g}{\partial\xi}\right]\Delta\xi+q_{g,sc}$$

..... (4-22)

For spent acid,

$$\frac{V_b}{\alpha_c}\frac{\partial}{\partial t}\left(\frac{\phi S_{sp}}{B_{sp}}+R_V\frac{\phi S_g}{B_g}\right)=\frac{1}{h_\eta^2}\frac{\partial}{\partial\eta}\left[\beta_c\frac{k_\eta k_{rsp}A_\eta}{\mu_{sp}B_{sp}}\frac{\partial p_{sp}}{\partial\eta}+\beta_c R_V\frac{k_\eta k_{rg}A_\eta}{\mu_g B_g}\frac{\partial p_g}{\partial\eta}\right]\Delta\eta$$
$$+\frac{1}{h_\xi^2}\frac{\partial}{\partial\xi}\left[\beta_c\frac{k_\xi k_{rsp}A_\xi}{\mu_{sp}B_{sp}}\frac{\partial p_{sp}}{\partial\xi}+\beta_c R_V\frac{k_\xi k_{rg}A_\xi}{\mu_g B_g}\frac{\partial p_g}{\partial\xi}\right]\Delta\xi+q_{sp,sc}$$

..... (4-23)

The reservoir PDEs are then discretized in both time and space to obtain the algebraic equations that can be solved simultaneously. Here, the term called transmissibility of spent acid/gas is introduced, as shown in Eq. 4.24. The transmissibility contains the geometrical factor of the flow between the two adjacent grids, and the pressure and saturation dependent parameters like formation volume factor, viscosity, and the relative permeability (Ertekin et al., 2001).

$$T_{g\eta} = \beta_c \frac{k_\eta A_\eta}{\delta\eta} \frac{k_{rg}}{\mu_g B_g} \quad \text{..... (4-24)}$$

For gas, the discretized form of Eq. 4-22 is,

$$\begin{aligned} &C_{g,p_{i,j}}\left(p_{g_{i,j}}^{n+1} - p_{g_{i,j}}^{n}\right) + C_{g,sp_{i,j}}\left(S_{sp_{i,j}}^{n+1} - S_{sp_{i,j}}^{n}\right) \\ &= T_{g\eta_{i+1/2,j}}^{n+1}\left(p_{g_{i+1,j}}^{n+1} - p_{g_{i,j}}^{n+1}\right) + T_{g\eta_{i-1/2,j}}^{n+1}\left(p_{g_{i-1,j}}^{n+1} - p_{g_{i,j}}^{n+1}\right) \\ &+ T_{g\xi_{i,j+1/2}}^{n+1}\left(p_{g_{i,j+1}}^{n+1} - p_{g_{i,j}}^{n+1}\right) + T_{g\xi_{i-1/2,j}}^{n+1}\left(p_{g_{i,j-1}}^{n+1} - p_{g_{i,j}}^{n+1}\right) + q_{gsc_{i,j}}^{n+1} \end{aligned} \quad \text{..... (4-25)}$$

$$C_{g,p} = \frac{h_\eta^2}{\Delta t}\left(\frac{V_b}{\alpha_c}\right)\left[\frac{\phi'}{B_g^n} + \phi^{n+1}\left(\frac{1}{B_g}\right)'\right]\left(1 - S_{sp}^n\right) \quad \text{..... (4-26)}$$

$$C_{g,sp} = -\frac{h_\eta^2}{\Delta t}\left(\frac{V_b}{\alpha_c}\right)\left(\frac{\phi}{B_g}\right)^{n+1} \quad \text{..... (4-27)}$$

For spent acid, the discretized form of Eq. 4-23 is,

$$\begin{aligned} &C_{sp,p_{i,j}}\left(p_{g_{i,j}}^{n+1} - p_{g_{i,j}}^{n}\right) + C_{sp,sp_{i,j}}\left(S_{sp_{i,j}}^{n+1} - S_{sp_{i,j}}^{n}\right) \\ &= T_{sp\eta_{i+1/2,j}}^{n+1}\left(p_{sp_{i+1,j}}^{n+1} - p_{sp_{i,j}}^{n+1}\right) + \left(T_{g\eta}R_V\right)_{i+1/2,j}^{n+1}\left(p_{g_{i+1,j}}^{n+1} - p_{g_{i,j}}^{n+1}\right) \\ &+ T_{sp\eta_{i-1/2,j}}^{n+1}\left(p_{sp_{i-1,j}}^{n+1} - p_{sp_{i,j}}^{n+1}\right) + \left(T_{g\eta}R_V\right)_{i-1/2,j}^{n+1}\left(p_{g_{i-1,j}}^{n+1} - p_{g_{i,j}}^{n+1}\right) \\ &+ T_{sp\xi_{i,j+1/2}}^{n+1}\left(p_{sp_{i,j+1}}^{n+1} - p_{sp_{i,j}}^{n+1}\right) + \left(T_{g\xi}R_V\right)_{i,j+1/2}^{n+1}\left(p_{g_{i,j+1}}^{n+1} - p_{g_{i,j}}^{n+1}\right) \\ &+ T_{sp\xi_{i,j-1/2}}^{n+1}\left(p_{sp_{i,j-1}}^{n+1} - p_{sp_{i,j}}^{n+1}\right) + \left(T_{g\xi}R_V\right)_{i,j-1/2}^{n+1}\left(p_{g_{i,j-1}}^{n+1} - p_{g_{i,j}}^{n+1}\right) + q_{sp,sc_{i,j}}^{n+1} \end{aligned} \quad \text{..... (4-28)}$$

$$C_{sp,p} = \frac{h_\eta^2}{\Delta t}\left(\frac{V_b}{\alpha_c}\right)\left(\begin{array}{c} \left[\frac{\phi'}{B_{sp}^n} + \phi^{n+1}\left(\frac{1}{B_{sp}}\right)'\right]S_{sp}^n \\ + \left\{\left[\frac{\phi'}{B_g^n} + \phi^{n+1}\left(\frac{1}{B_g}\right)'\right]R_V^n + \left(\frac{\phi}{B_g}\right)^{n+1} R_V'\right\} \times \left(1 - S_{sp}^n\right) \end{array}\right) \quad \text{..... (4-29)}$$

$$C_{sp,sp} = \frac{h_\eta^2}{\Delta t}\left(\frac{V_b}{\alpha_c}\right)\left[\left(\frac{\phi}{B_{sp}}\right)^{n+1} - \left(\frac{\phi}{B_g}\right)^{n+1} R_V^{n+1}\right] \quad \text{..... (4-30)}$$

After the PDEs are discretized, two algebraic equations, one for gas and one for spent acid, exist for each grid block. When these equations are assembled together, it is a non-linear equation set and has the following general form,

$$f_i\left(\{x_j\}\right) = 0,\ 1 \le i,\ j \le n,\ \text{where } \{x_j\} = (x_1, x_2, \ldots x_n) \quad \text{..... (4-31)}$$

where x_j represents the pressure and saturation unknowns for all the grid blocks.

There are a number of formulations that can be used to solve this equation set, such as implicit pressure explicit saturation (IMPES), fully implicit and etc. The advantage of IMPES formulation is its speed. In this study, we choose to use the fully implicit formulation for the fact that it provides more flexibility in selecting the time-step and grid size. In the fully implicit formulation, the pressure and saturation unknowns as well as the terms that depend on the primary variables are all evaluated at the new time step $n+1$. This treatment of the flow equations results in a non-linear system of equations.

A non-linear equation system has to be linearized before any solution technique is applied to solve the problem. Newton-Raphson method is a widely used algorithm to solve this type of equation systems. In Newton-Raphson method, the system of non-linear equations is linearized employing a first-order Taylor expansion as expressed in Eq. 4-32,

$$f_i\left(x^{k+1}\right) = f_i\left(x^k\right) + \sum_{j=1}^{n} \left.\frac{\partial f_i}{\partial x_j}\right|_{x^k} \left(x_j^{k+1} - x_j^k\right) + \ldots \quad \text{..... (4-32)}$$

where x^k is a column vector of starting points, $f_i\left(x^k\right)$ is the values of the function at the starting points, x^{k+1} is the column vector of points at some other location, $f_i\left(x^{k+1}\right)$ is the approximate function values at that location, and the first derivatives of the functions are the Jacobian of the equation system. In a Jacobian matrix, the functions that are differentiated go down the matrix as rows and the parameters for which the partial

derivatives are calculated go across the matrix as columns. An example of Jacobian matrix is given below.

$$J = \begin{bmatrix} \frac{\partial f_1(X)}{\partial x_1} & \frac{\partial f_1(X)}{\partial x_2} & \cdots & \frac{\partial f_1(X)}{\partial x_n} \\ \frac{\partial f_2(X)}{\partial x_1} & \frac{\partial f_2(X)}{\partial x_2} & \cdots & \frac{\partial f_2(X)}{\partial x_n} \\ \vdots & \vdots & \ddots & \vdots \\ \frac{\partial f_n(X)}{\partial x_1} & \frac{\partial f_n(X)}{\partial x_2} & \cdots & \frac{\partial f_n(X)}{\partial x_n} \end{bmatrix} \quad \text{..... (4-33)}$$

For this study, the details of the Jacobian matrix for spent acid and gas flow equations, Eq. 4-25 and 4-28, can be found in Ertekin et al.'s book (2001). With the definition of Jacobian matrix, the Newton-Raphson method estimates the new root using the following equation.

$$X^{k+1} = X^k - \left[J\left(X^k\right)\right]^{-1} F\left(X^k\right) \quad \text{..... (4-34)}$$

It is noted that an iterative process is established in Eq. 4-26. First, an initial estimate is used to solve the linear system and provides a search direction. Then, the Newton direction is used to update the previous estimate. The process is repeated until a convergence criterion, e.g. Eq. 4-35, is attained (Monteagudo and Firoozabadi, 2007).

$$\left\| X^{k+1} - X^k \right\| \le \varepsilon \quad \text{..... (4-35)}$$

where ε is the tolerance.

Having shown the details of the system models and the solving method, we now list the flow sequence of our program. The essential steps in a simulator are given below (Cao, 2002):

1. Provide input data (problem definition)
2. Initialize (allocate data and set initial conditions)
3. Start time step calculations
    a. Initialize with old time step data

b. Start the Newton iteration

c. Calculate gridblock properties

d. Linearize (calculate and assemble Jacobian and RHS)

e. Solve the linear system

f. Perform Newton update

g. Check convergence, do another Newton iteration if necessary

4. Print and plot results at appropriate times
5. Increment time and go to Step 3 if ending conditions are not reached
6. End when run is complete

4.2.4 Treatments of boundary conditions

Two common boundary conditions, constant-pressure boundary and specified-flux boundary, are implemented in our program.

A constant-pressure boundary develops when the rate of fluids withdrawn on one side of the boundary is equal to the rate of fluids being supplied or injected on the other side of the same boundary (Ertekin et al., 2001). In the program, we handle the constant-pressure condition by replacing it with a fictitious well in the boundary gridblock. Take boundary gridblock $i = 1$ in one dimension as an example, the resulting equation and the injecting (or producing) rate of the fictitious well are given in the following equations, respectively,

$$q^*_{gsc1} + T_{g\eta_{1+1/2}}{}^{n+1}\left(p_{g\eta_2}{}^{n+1} - p_{g\eta_1}{}^{n+1}\right) = \ldots \quad \text{(4-36)}$$

$$q^*_{gsc1} = \left[2\beta_c\left(\frac{k_\eta A_\eta}{\Delta\eta}\right)_1\left(\frac{k_{rg}}{\mu_g B_g}\right)_1\right]\left(p_e - p_{g\eta_1}{}^{n+1}\right) \quad \text{(4-37)}$$

A specified-flux boundary condition arises when the reservoir is in communication with the surroundings. This type of boundary condition can be replaced with a no-flow

boundary and a fictitious injection/production well with the specified fluid flux distributed along the boundary gridblocks as well (Ertekin et al., 2001). The resulting equation shares the same form as Eq. 4-36.

4.3 Model and Program Validation

In this section, we validate our model and program by calculating cases and comparing the results with those from the commercial software. Two synthetic cases are built for the validation purpose. The first case is built to test the stability of the program and is run without considering any evaporation, meanwhile in the second case only the evaporation process is considered.

4.3.1 Program validation without evaporation

In this synthetic case, the simulation region has a rectangular shape, with four injectors on one side and two producers on the other side. The simulation structure is presented in **Fig. 4.3** and the detailed reservoir and well parameters are listed in **Table 4.1**.

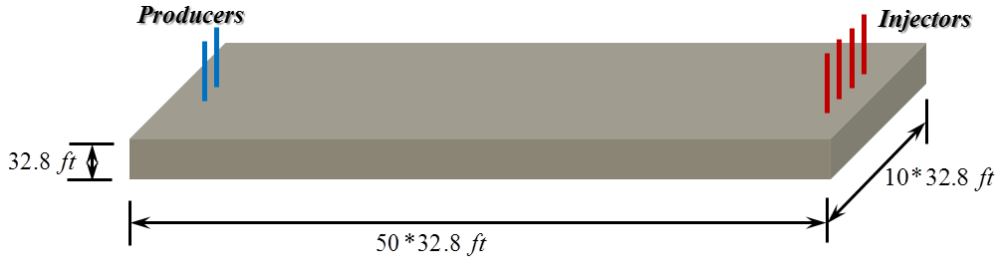

Fig. 4.3 Illustration of the simulation domain

Table 4.1 Reservoir and well parameters in program validation

Reservoir			Wellbore	
Drainage area, ft×ft	50×10×32.82		Depth of the wellbore, ft	4016.4
Thickness, ft	32.8		Wellbore radius, ft	0.583
Depth of top, ft	4000		Producer pressure, psi	3000
Porosity	0.2		Injector Pressure, psi	4000
Permeability, md	100		Producer location, grid	(1, 5&6)
Initial pressure, psi	3800		Injector location, grid	(50, 4&5&6&7)

Two phases, gas and water, are included in this case. In order to test program stability, an abrupt saturation change is assigned to the initial water distribution, as is shown in **Fig. 4.4**. Other parameter values, such as fluid and rock properties, are given in **Table 4.2** through **Table 4.4**.

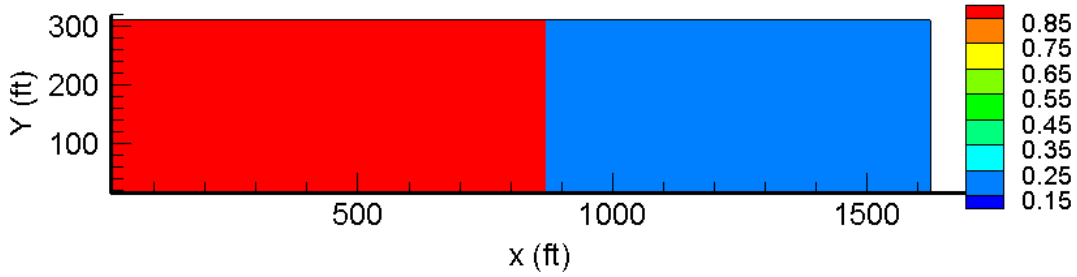

Fig. 4.4 Initial water saturation

Table 4.2 Fluid and rock properties

	Gas	Water	Rock
Density at reference pressure (lbm/ft^3)	0.07	62	
Compressibility (1/psi)		3.0e-06	3.0e-06
Formation volume factor at reference pressure, RB/STB		1	
Reference pressure, psi		2800	

Table 4.3 Gas-water saturation functions

Gas Saturation	k_{rg}	k_{rw}	p_c (psi)
0.08	0.00	0.80	0.00
0.10	0.07	0.77	7.49
0.15	0.17	0.69	18.22
0.20	0.24	0.62	26.72
0.30	0.37	0.48	41.09
0.40	0.49	0.36	53.61
0.50	0.59	0.25	65.03
0.60	0.68	0.15	75.68
0.70	0.77	0.07	85.74
0.80	0.86	0.01	95.34
0.85	0.90	0.00	100.00

Table 4.4 PVT properties of dry gas

Pressure(psi)	Gas FVF(rb/Mscf)	Gas Viscosity (*cP*)
400	5.9	0.0130
800	2.95	0.0135
1200	1.96	0.0140
1600	1.47	0.0145
2000	1.18	0.0150
2400	0.98	0.0155
2800	0.84	0.0160
3200	0.74	0.0165
3600	0.65	0.0170
4000	0.59	0.0175
4400	0.54	0.0180
4800	0.49	0.0185
5200	0.45	0.0190
5600	0.42	0.0195

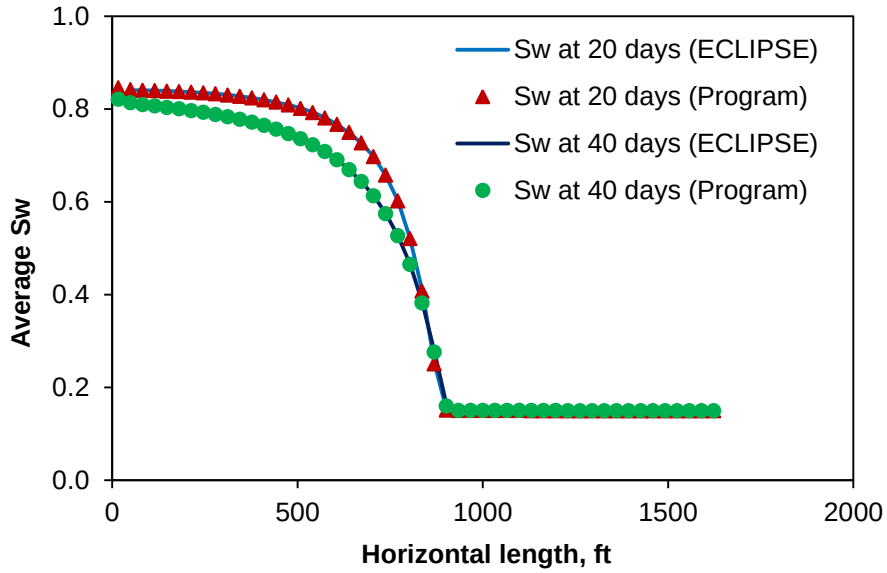

Fig. 4.5 Comparison of average water saturation at different times between commercial software and the program

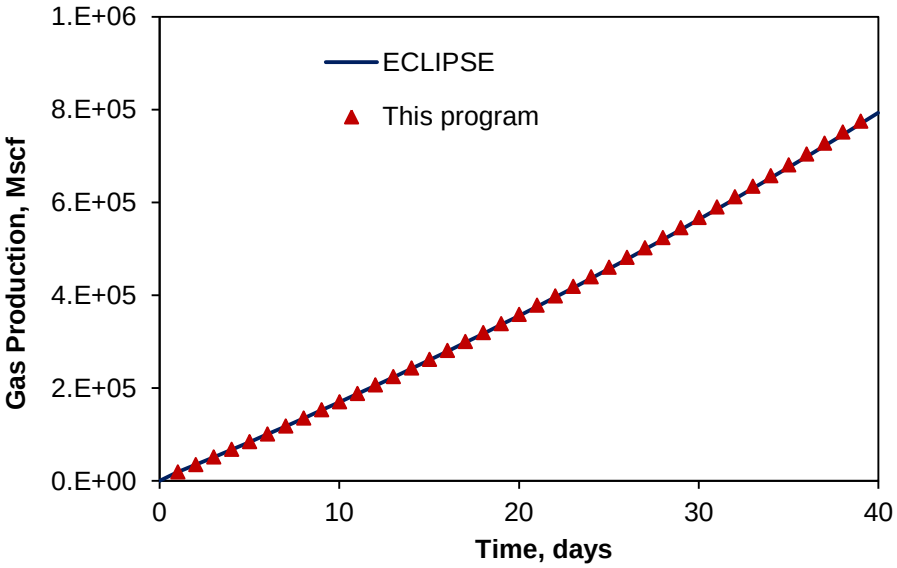

Fig. 4.6 Comparison of cumulative gas production between commercial software and the program

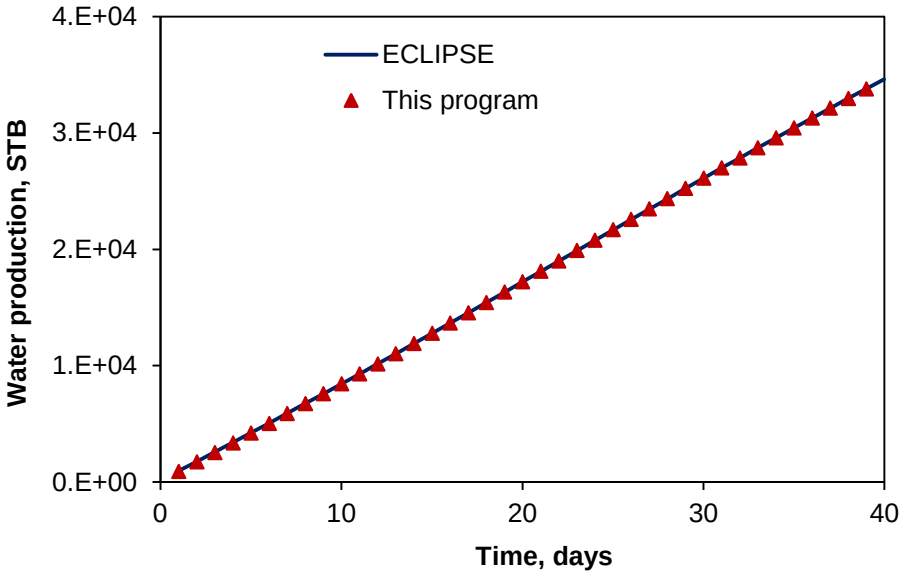

Fig. 4.7 Comparison of cumulative water production between commercial software and the program

In the simulation, gas is injected. Since no evaporation is included, commercial software Eclipse 100 (Schlumberger) is utilized. In **Fig. 4.5** through **Fig. 4.7**, the comparisons of average water saturation along the reservoir at different times, the cumulative gas production, and the cumulative water production between the program and the commercial software are presented. We can see that our program can capture the average water distributions effectively. Besides, good agreements for cumulative productions are obtained as well. The comparison results validate the program and its stability.

4.3.2 Evaporation validation

In this part, we build a synthetic case to study the performance of our program in simulating the spent acid evaporation phenomenon. In order to do so, we only consider the evaporation term in the spent acid flow equation, thus Eq. 4.3 becomes

$$\frac{\partial}{\partial t}\left[\frac{\phi R_V \rho_{ws}}{B_g} S_g\right] = -\vec{\nabla}\cdot\left(\frac{R_V \rho_{ws}}{B_g}\vec{u}_g\right) + q_w \quad \text{..... (4-38)}$$

The simulated area has a simple rectangular shaped structure, as is shown in **Fig. 4.8**. Constant pressure conditions are applied to both the left and right boundaries. All the other boundaries are no-flow boundaries. The irreducible spent acid saturation is 0.15, as can be seen from the gas-spent acid saturation function table (**Table 4.5**). The initial spent acid saturation is set to 0.05 for all the gridblocks to make sure that spent acid does not flow by itself. The other parameters that are involved in this simulation are listed in **Table 4.6**.

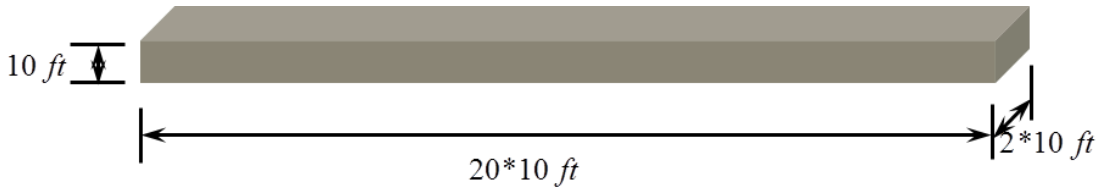

Fig. 4.8 Illustration of the simulation domain

Table 4.5 Gas-spent acid saturation functions

Gas Saturation	k_{rg}	k_{rw}
0.08	0	0.8
0.1	2.54e-06	0.769034
0.15	0.000204	0.693427
0.2	0.001345	0.620474
0.3	0.01122	0.482945
0.4	0.041644	0.357415
0.5	0.107869	0.245164
0.6	0.227791	0.148001
0.7	0.421595	0.068785
0.8	0.711523	0.013238
0.85	0.9	0

Table 4.6 Reservoir parameters in program validation

Drainage area, ft×ft	20×2×10		Initial spent acid saturation, fraction	0.05
Thickness, ft	10		Reservoir temperature, K	350
Depth of top, ft	4000		Left boundary pressure, psi	3000
Porosity, fraction	0.2		Right boundary pressure, psi	4000
Permeability, md	100		Initial reservoir pressure, psi	3800

The method used in our program is the modified black oil method and we compare the results with those from a compositional simulator (Eclipse E300). The comparison results are listed in the following figures.

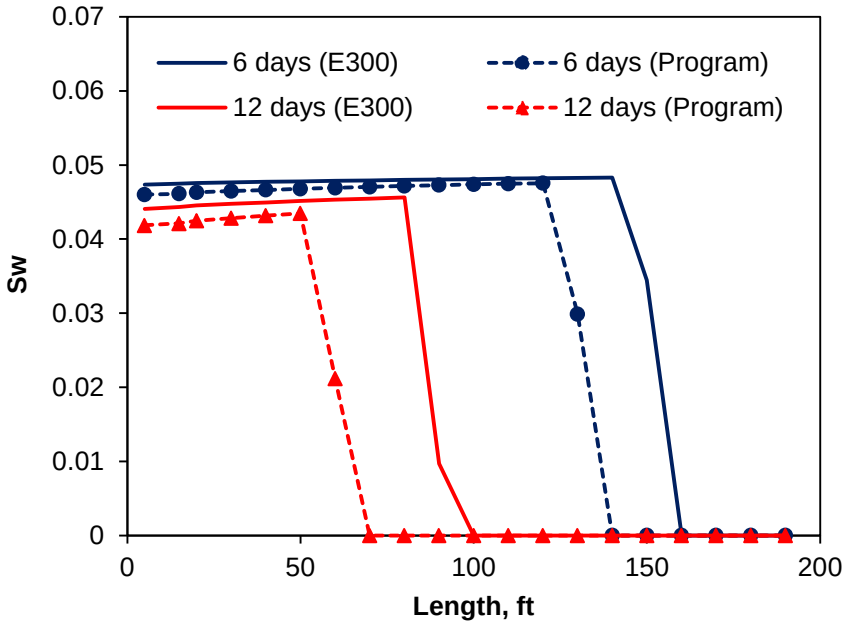

Fig. 4.9 Comaprison of spent acid distribution along the simulation domain between commercial software and the program

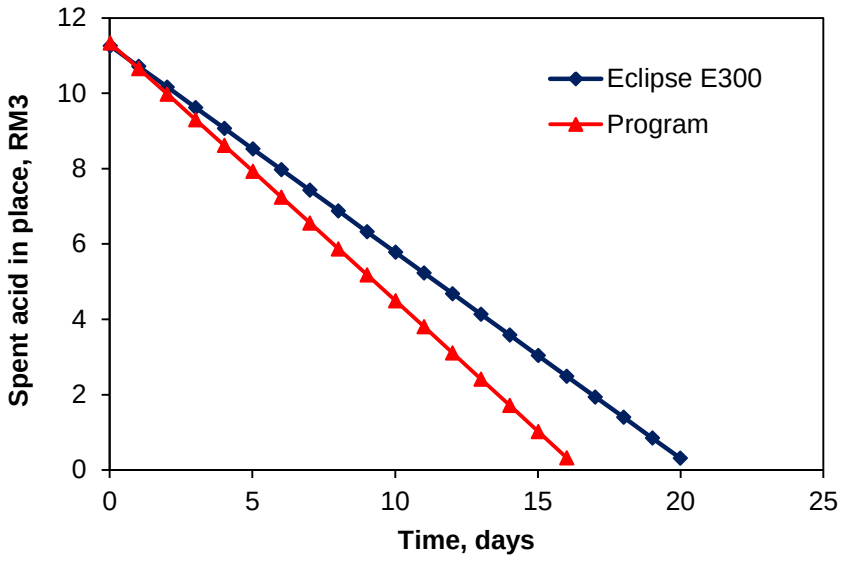

Fig. 4.10 Comparison of spent acid left in place between commercial software and the program

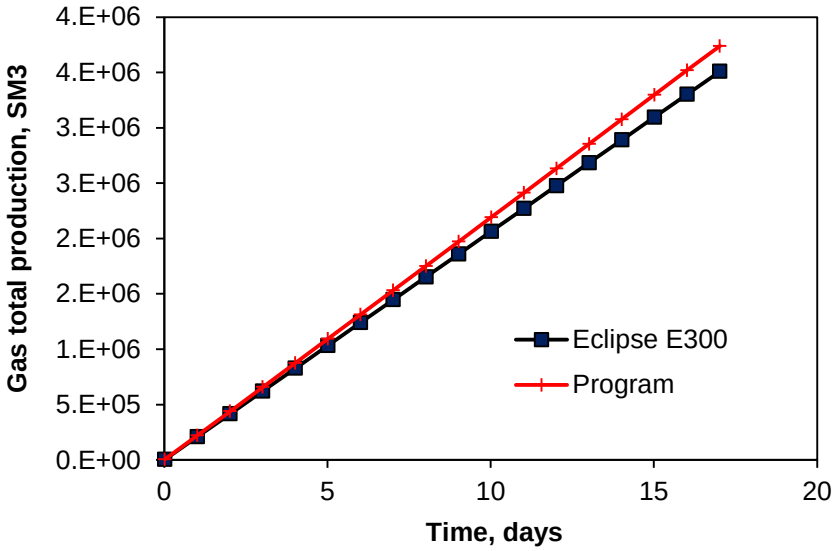

Fig. 4.11 Comparison of total gas production between commercial software and the program

In **Fig. 4.9**, the spent acid distributions along the simulation domain are presented at different times. We can see that at both times the dry front moves faster in our programs. It is because we use the modified black oil method to characterize the fluid and

the commercial software employs the full equation-of-state compositional simulation to characterize the fluid. This difference results in a slightly larger spent acid content (i.e., higher evaporation rate) in the gas phase at each time step for our program. However the spent acid distributions do share similar shapes. In **Fig. 4.10** and **Fig. 4.11**, we compare the spent acid amount left in the place as well as the total gas production. Both of the curves have the same trends. But since the evaporation rate in our program is larger than that in the commercial software, the spent acid left in the place decreases faster in our program and also the total gas production is higher at different times. The comparison results validate the accuracy of evaporation part in our programs.

4.4 Chapter Summary

In this chapter, we borrow the idea from the modified black oil model to model the evaporation phenomenon in the spent acid recovery process. This idea is fulfilled by introducing a vaporized spent acid/water-gas ratio, R_V. We then describe the details of the controlling equations. Following that, the method that is used to characterize the fluids are presented. The nonlinear PDE's are then discretized and linearized by using the Newton-Raphson method.

Finally, two synthetic cases are built to verify the program. The first case is set up without including evaporation and it validates the stability of the program. The second case is built to test the evaporation part in the program. Although there are differences between the two methods, the discrepancy is acceptable since we use a different method to calculate the spent acid content in vapor phase at different time steps.

5. PARAMETRIC STUDY OF SPENT ACID RECOVERY[†]

5.1 Introduction

It is commonly believed that spent acid recovery process is affected by different factors. Mahadevan and Sharma (2003) performed gas displacement experiments on cores fully saturated with brine for long periods of time and quantified effects of several factors on cleanup of water blocks. Their results showed that increases in core permeability, temperature, pressure drawdown and change of wettability of the rock from water-wet to oil-wet all resulted in faster cleanups. Parekh and Sharma (2004) conducted a detailed parametric study for a gas-water system and an oil-water system and showed the effect of various factors on the cleanup of the water blocks. They concluded that some key parameters which have a strong influence on the cleanup of water blocks are: drawdown, formation permeability, fracture length, shapes of relative permeability curves, and volumes of water leak-off and formation heterogeneity.

With the spent acid front calculated in the preceding chapter, we are now able to simulate the gas flowback/spent acid recovery process that follows acid stimulation. In the subsequent part of this section, a number of simulations are performed to investigate the influence of pressure drawdown, formation permeability, pore-size distribution, and formation wettability on the spent acid recovery processes.

5.2 Parametric Study of Spent Acid Recovery

In the succeeding studies, for the purpose of parametric study, we use the same spent acid profile for all the cases. This specific spent acid profile was obtained by simulating the injection of acid into a formation (porosity = 0.15) for 1 hour, which is the outmost curve

[†]Part of this section is reprinted with permission from "Modeling of Spent-Acid Blockage Damage in Stimulated Gas Wells" by A.D. Hill, Q. Zhang, D. Zhu. Paper IPTC 16481-MS presented at the International Petroleum Technology Conference, 26-28 March 2013, Beijing, China. Copyright 2013 by International Petroleum Technology Conference.

as shown in **Fig. 3.8**. The spent acid penetration distance along the wormhole tip direction is about 5 inches and the penetration distance perpendicular to the tip direction is about 8.53 inches. An illustration of the simulation domain and boundary conditions is provided in **Fig. 5.1**. The spent acid front profile is not an exact ellipse although its shape is very close to an ellipse. Therefore, in order to use the constant boundary condition along the elliptical outline, extra gridblocks are added between the spent acid front and the outer boundary. The parameter studies without considering the evaporation terms are shown first and the simulation results with evaporation included are presented following that. In **Table 5.1**, some fluid and reservoir properties are listed. Other parameters that are not listed here are calculated and updated during the simulations.

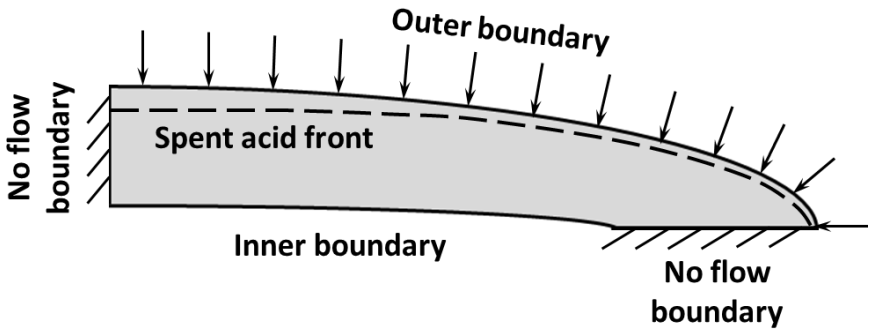

Fig. 5.1 The simulation domain and the boundary conditions

Table 5.1 Reservoir and fluid properties for parametric studies

Number of grid cells	52 * 53
Initial reservoir pressure at reference depth, p_i, psi	3450
Porosity, fraction	0.15
Rock compressibility, c_r, psi^{-1}	3.0e-6
Spent acid compressibility at reference pressure, $c_{sp}(p_{ref})$, psi^{-1}	3.0e-6
Spent acid FVF at reference pressure, $B_{sp}(p_{ref})$, RB/STB	1
Spent acid viscosity at reference pressure, $\mu_{sp}(p_{ref})$, cp	1
Reference pressure, p_{ref}, psi	2800

5.2.1 Effect of pressure drawdown

The starting point in this part of the study is the effect of pressure drawdown. Since spent acid invasion happens very close to the wellbore and a large pressure drop can be usually observed around this region, we set the largest pressure drawdown to be 100 psi. Smaller pressure drawdowns are applied as comparisons. The formation absolute permeability is set to 10 millidarcy. We do not take into account any other property changes and we also consider that the formation is liquid wetted since most of the reservoirs are originally liquid-wetted.

In **Fig. 5.2** and **Fig. 5.3**, the spent acid and gas production recovery processes with different pressure drops are presented. From the simulation results, we can see that as long as the pressure drawdowns are larger than the capillary entry pressure, the spent acid can be recovered to the same level for all the cases. However, since the formation is liquid-wetted, when the spent acid recovery has reached a plateau, there is still over 60% of spent acid left in the formation. Accordingly, the gas production rates are all restored to a level of over 80% of the unaffected production rates.

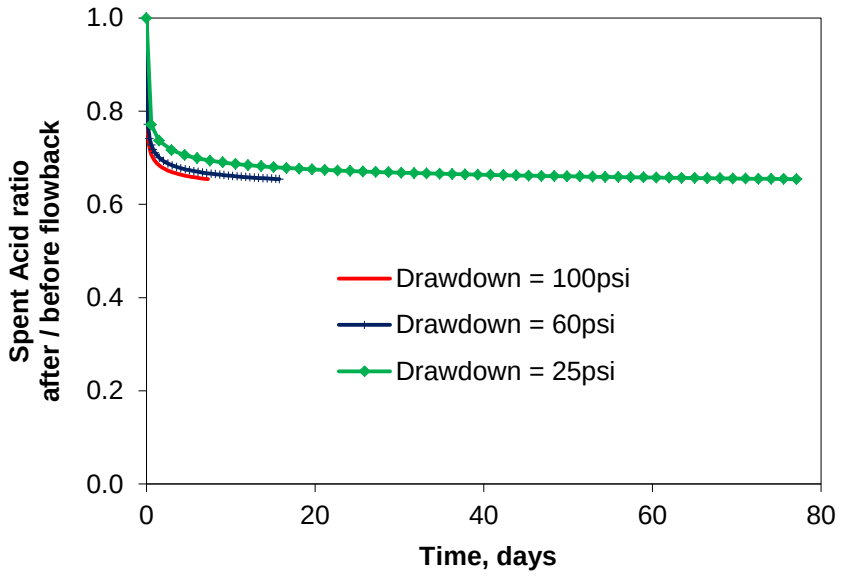

Fig. 5.2 Spent acid recovery process with different pressure drops

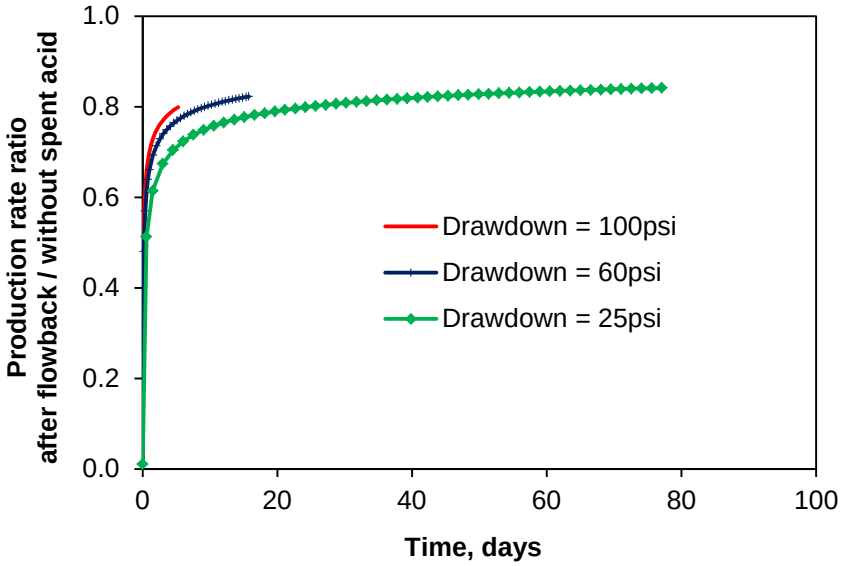

Fig. 5.3 Production recoveries with different pressure drops

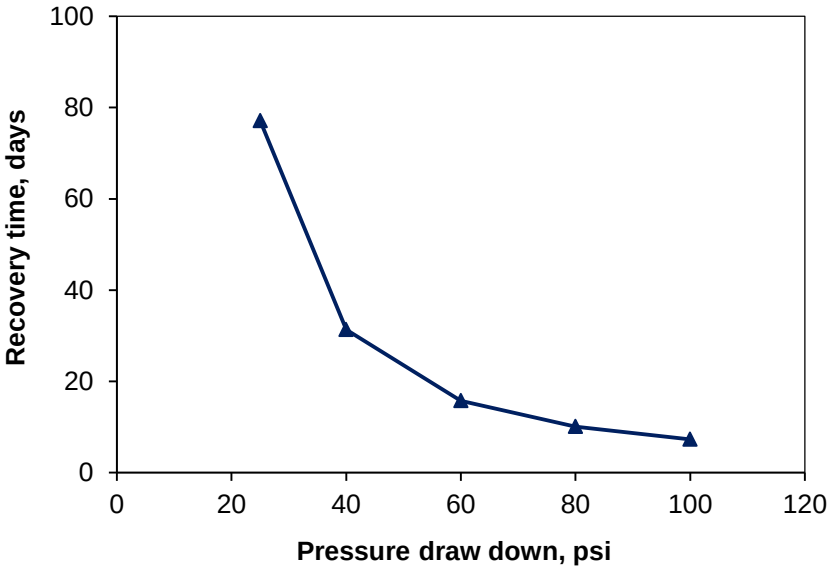

Fig. 5.4 Recovery time with different pressure drops

In **Fig. 5.4**, we show the time that is needed to recover the same amount of spent acid. It can be seen that the time increases exponentially with the decreasing pressure drawdown. When the pressure drop is around 20 psi, it takes almost 3 months to restore the gas production. The above analyses indicate that small pressure drop would definitely

the production rate and lower the bottom-hole pressure might assist the spent acid recovery process to an extent.

Fig. 5.5 shows the pressure distribution at the end of the simulation. From the figure we notice that the largest pressure drop happens around the wormhole tip zone. In **Fig. 5.6**, we show the spent acid distribution profile in the simulation domain at different recovery stages. We can see that there are remarkable saturation changes between the first 3 figures and the simulation period for these 3 figures is only about 2.78 days. The last figure in **Fig. 5.6** is plotted close to the end of the simulation, which is about 18.3 days of gas flowback. It is obvious that there is not much change between the last two figures. It implies that spent acid gets recovered at a high rate at the early stages and then the recovery rate slows down. This corresponds with the spent acid recovery curves in **Fig. 5.2**, which all have steep shapes at earlier times and turn flat at later stages.

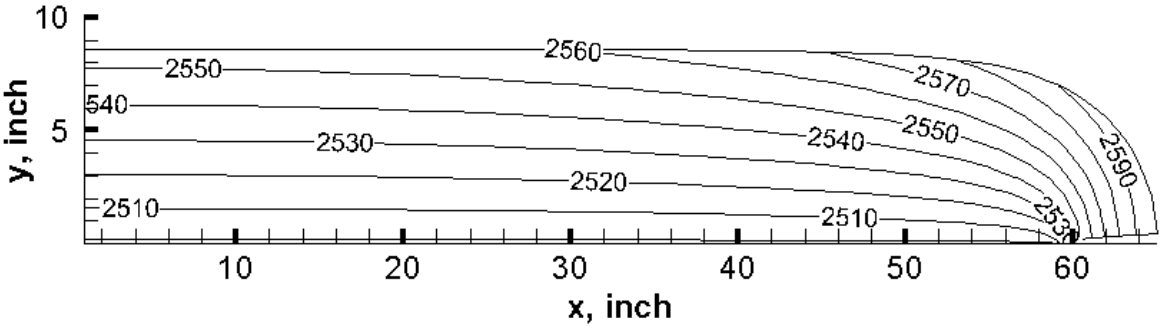

Fig. 5.5 Pressure distribution in the simulation domain

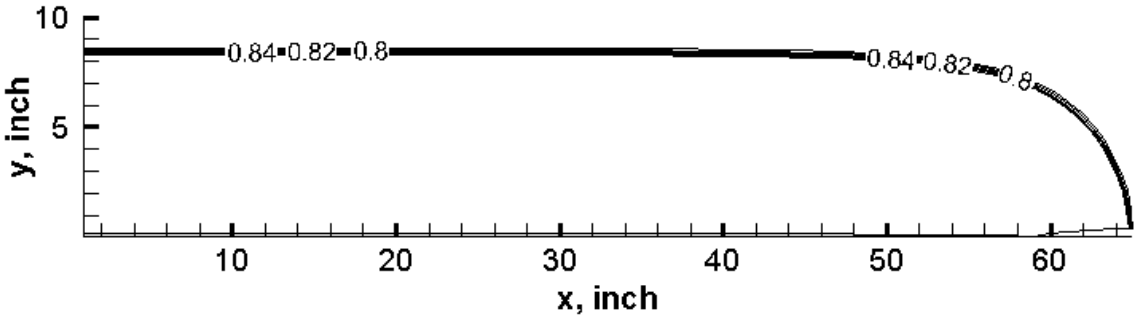

t = 0.0001 days

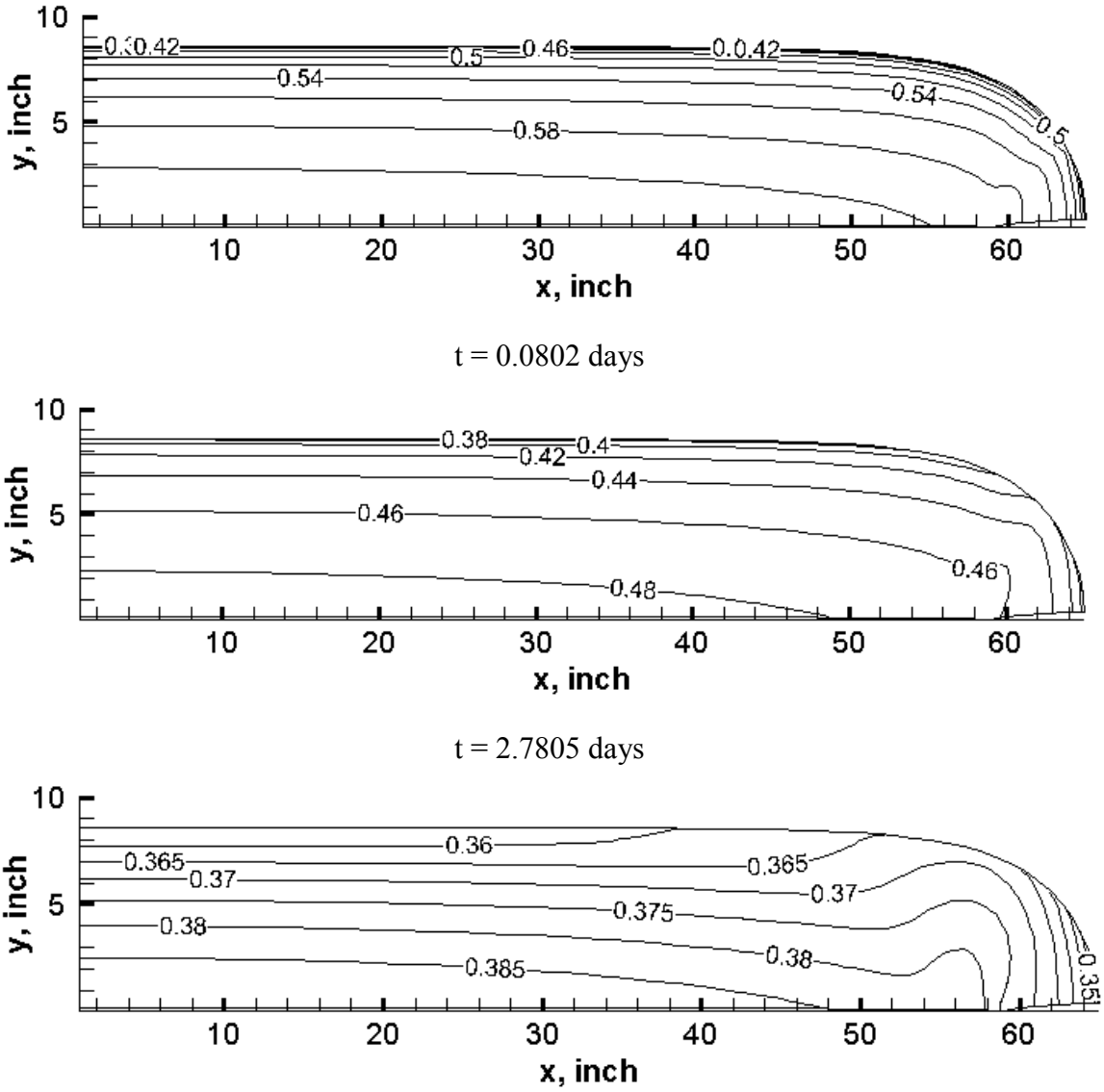

Fig. 5.6 Spent acid distribution profiles at different recovery stages

5.2.2 Effect of absolute permeability

Formation permeability is another factor that is often considered in spent acid recovery studies. Permeability is important because it is a rock property that relates to the rate at which hydrocarbon can be recovered. Carbonate reservoirs throw challenges to geologists to characterize due to their heterogeneous tendency for depositional and diagenetic

processes. The petrophysical heterogeneity of carbonate reservoir is demonstrated by the wide variablity observed in porosity-permeability cross-plots (Sharma, 2011).

The permeability of carbonate rocks cover orders of magnitude. In order to examine the effect of formation permeability, three cases are simulated and compared, with formation permeabilities set to 1 md, 10 md, and 100 md separately. The pressure drawdown is set to 40 psi for all the cases. The formation is still considered as liquid wetted and all the other properties are kept the same. The spent acid recovery process is recorded in **Fig. 5.7**. The figure for the highest permeability (100 md) situation is shown additionally in **Fig. 5.8** to illustrate that the spent acid recovery has reached the steady regime for this case. From the simulation results, we can see that the spent acid recovery reached a plateau for the high permeability reservoir in about 1.5 days. While for the low permeability formation, it would take over 3 months to recover the spent acid to the same level. In all the three cases, the production rates are restored to over 80% of the unaffected production rates too.

In **Fig. 5.9**, the times needed to remove the same amount of spent acid for different formation permeabilities are presented. We can see that the time increases exponentially with the decreasing formation permeability. This result indicates that formation absolute permeability could have a pronounced effect on gas production, since low permeability usually leads to extreme slow spent acid cleanups. The situation might become even worse in formations with low pressure drops, because the spent acid recovery time also increases exponentially with decreasing pressure drop.

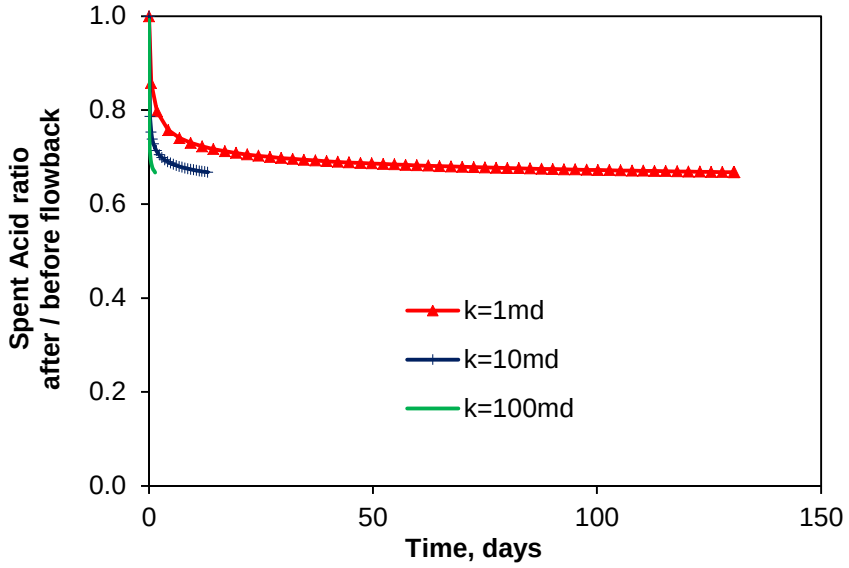

Fig. 5.7 Spent acid recovery process with different absolute permeability

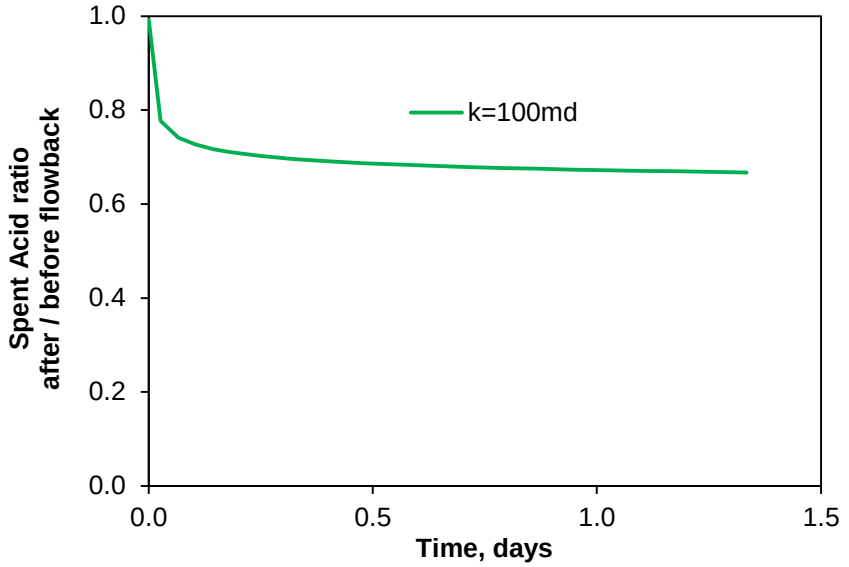

Fig. 5.8 Spent acid recovery process (absolute permeability equals 100md)

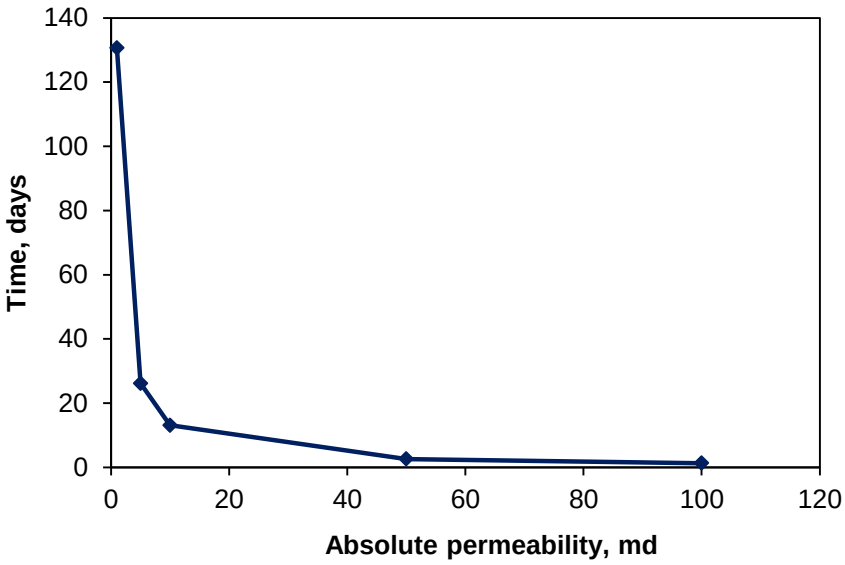

Fig. 5.9 Recovery time with different formation permeabilities

5.2.3 Effect of pore-size distribution

Relative permeability is "a direct measure of the ability of the porous system to conduct one fluid when one or more fluids are present. These flow properties are the composite effect of pore geometry, wettability, fluid distribution, and saturation history (Anderson, 1987)." Different empirical correlations for relative permeability curves have been suggested. The most utilized relative permeability model is the so called modified Brooks and Corey model or the power law model (Brooks and Corey, 1964). The modified Brooks and Corey model is explicitly a function of relative permeability end points.

$$\begin{aligned} k_{r,w} &= k'_{r,w}\left(S_{wn}\right)^{n_w} \qquad n_w = 3 + 2/\lambda \\ k_{r,nw} &= k'_{r,nw}\left(S_{nwn}\right)^{n_{nw}} \qquad n_{nw} = 1 + 2/\lambda \end{aligned} \quad \text{..... (5-1)}$$

where

$$S_{wn} = \frac{S_w - S_{w,irr}}{1 - S_{w,irr} - S_{nw,irr}} \quad \text{..... (5-2)}$$

is the normalized wetting phase saturation. $k'_{r,w}$ and $k'_{r,nw}$ are the endpoint relative permeability for wetting and non-wetting phases, respectively. $S_{w,irr}$ and $S_{nw,irr}$ are the irreducible saturations for both phases.

Capillary pressure is a basic rock-fluid characteristic in multiphase flow. The displacement of one fluid by another in the pores of a porous medium is either aided or opposed by surface forces of capillary pressure. Accurately predicting capillary pressures in a porous medium is essential to understand the movement and distribution of fluids within such systems. The relationship between capillary pressure and fluid saturation often follows some form of power law, other than the expression in Eq. 1-1, which is only valid for the capillary equilibrium situation. In the existing capillary pressure correlations, there are typically two adjustable parameters. One parameter expresses the pore size distribution and hence the curvature of the capillary pressure curve and the other parameter expresses the actual level of the capillary pressure, i.e., the entry or the mean capillary pressure (Skjaeveland et al., 2000). The capillary function is given in the following equation (Brooks and Corey, 1964),

$$P_c = P_{entry}\left(S_{wn}\right)^{-1/\lambda} \quad \text{..... (5-3)}$$

where P_{entry} is the capillary entry pressure. λ is the rock sorting parameter (pore-size distribution coefficient).

The term "sorting" is used to describe the distribution of grain sizes in a formation. Reservoir rocks usually have a parameter λ between 0.25 and 4. Very well sorted rocks have fairly uniform grain size, resulting in high porosity and high values of λ. Poorly sorted rocks have a wide range of grain size and low porosity and they have low values of λ. An illustration of reservoir rock sorting is given in **Fig. 5.10**.

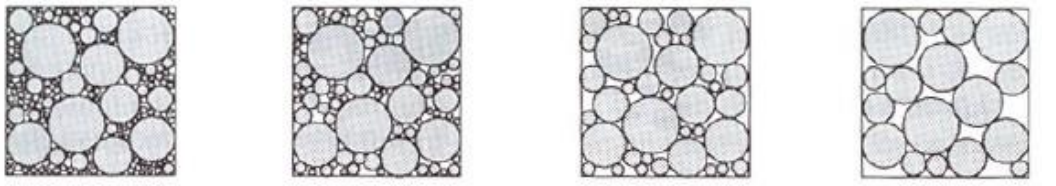

Fig. 5.10 Illustration of differently sorted formations (Crain)

In order to investigate the impact of pore-size distribution on spent acid recovery processes, we study cases on liquid wetted formations with two extreme sorting numbers. For the very-well sorted formation, the pore-size distribution coefficient is set to 4 and the exponents in spent acid and gas relative permeability functions are 3.5 and 1.5 (Eq. 5-1), respectively. Meanwhile, the pore-size distribution coefficient for the poorly sorted formation equals 0.5, resulting in 7 and 5 for the exponents of spent acid and gas phases. The pressure drops for both cases are 400 psi. The values we choose for the other parameters are: $k_{r,w}^{'} = 0.8$, $k_{r,nw}^{'} = 0.9$, $S_{w,irr} = 0.15$, and $S_{nw,irr} = 0.08$.

The relative permeability curves are shown in **Fig. 5.11**. We use the same end-point phase relative permeability since both formations are considered non-liquid wetted. It can be noticed that the sorting number greatly affects the shapes of the relative permeability profiles. According to the figure, for the well sorted formation, the spent acid relative permeability approaches zero only when spent acid saturation is close to the irreducible value. For the poorly sorted formation, the spent acid relative permeability becomes very small even when the spent acid saturation is about 0.5. It indicates that comparing with the well sorted formation it would take a longer time to recover the same amount of spent acid from the poorly sorted one.

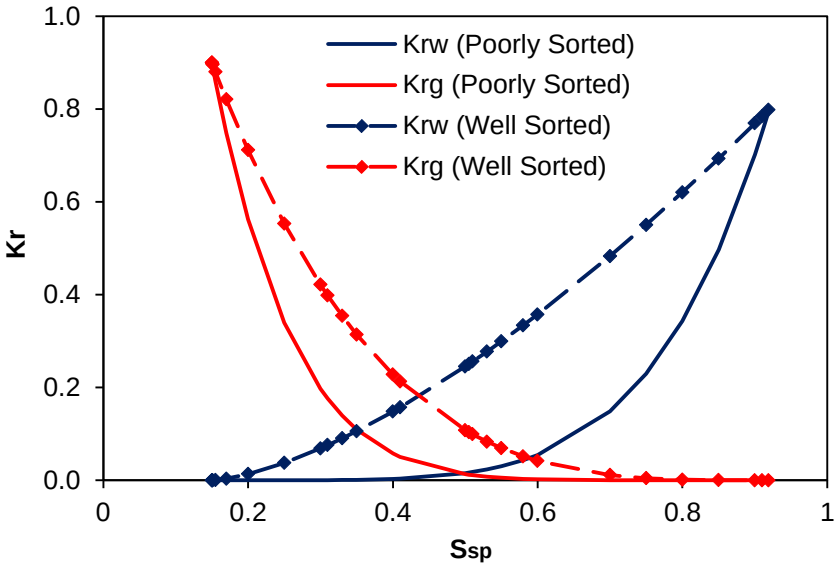

Fig. 5.11 Relative permeability curves for poorly ($n_w = 7$, $n_{nw} = 5$) and well sorted ($n_w = 3.5$, $n_{nw} = 1.5$) matrices

In **Fig. 5.12**, we present the capillary pressure curves. We see that capillary pressure curve gives information about the pore size distribution (sorting). The shape of the middle part of the capillary pressure is: flat for well-sorted pore size and steep for poorly sorted pore size (Schon, 2011). Again according to Anderson (1987), the work for one fluid to displace the other from the formation is related to the area under the capillary pressure curve. For gas displacing spent acid, the external work, ΔW_{ext} , required is,

$$\Delta W_{\text{ext}} = -\phi V_b \int_{S_{sp1}}^{S_{sp2}} p_c \, \mathrm{d}S_{sp} \quad \text{..... (5-4)}$$

where V_b is the bulk volume. From the figure, it is obvious that the capillary pressure curve for a poorly sorted formation covers more area than the very well sorted one. That once again implies that for reservoirs with the same pressure drops, longer time is needed to recover the same amount of spent acid from a poorly sorted formation.

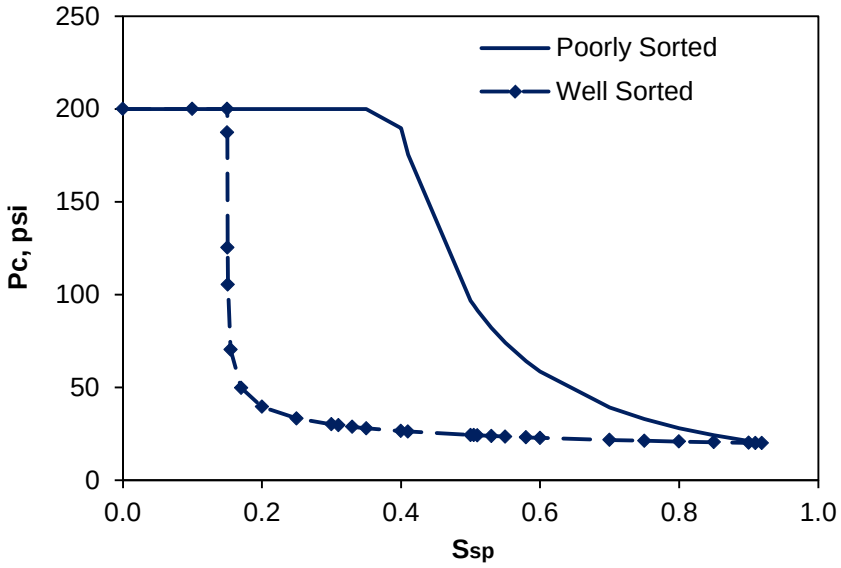

Fig. 5.12 Capillary pressure curves for poorly ($\lambda = 0.5$) and well sorted ($\lambda = 4$) matrices

The above discussions are verified with the simulation results, as shown in **Fig. 5.13** and **Fig. 5.14**. For both of the cases, the simulated gas injection periods are about 3 months. For the very well sorted formation, spent acid recovery process happens fast and most of the recovery happens in the first 10 days. Correspondingly, the recovered production rate is over 80% of that before the spent acid invasion. For the poorly sorted one, the spent acid can be recovered almost to the same levels. However, since the gas relative permeability is still very low, only over 40% of the original production rate is recovered. From the above analyses, we know that pore-size distribution is an important factor that affects spent acid recovery since it has a great influence on spent acid and gas relative permeabilities. Introduction of liquid phase into the poorly sorted formations might be harmful to the production and it would be beneficial if the formation textural properties can be understood before any treatment.

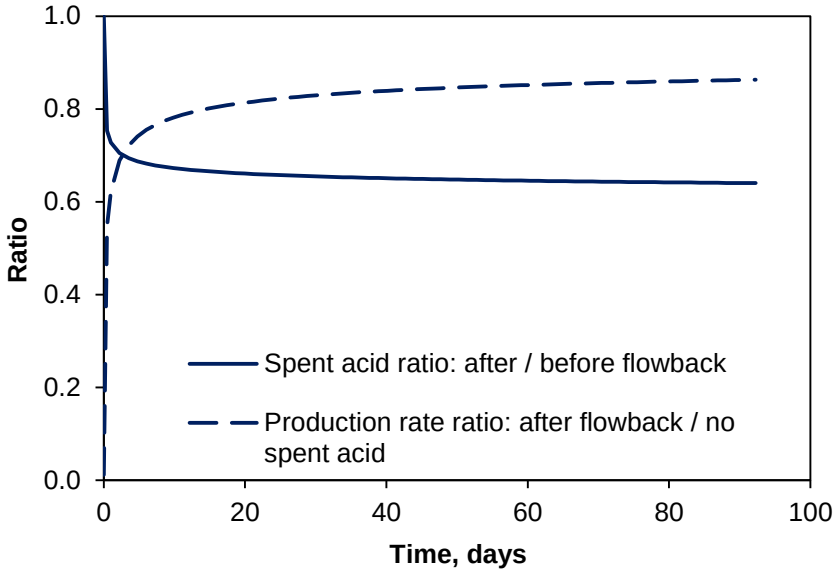

Fig. 5.13 Spent acid and production rate recovery curves for well sorted matrix

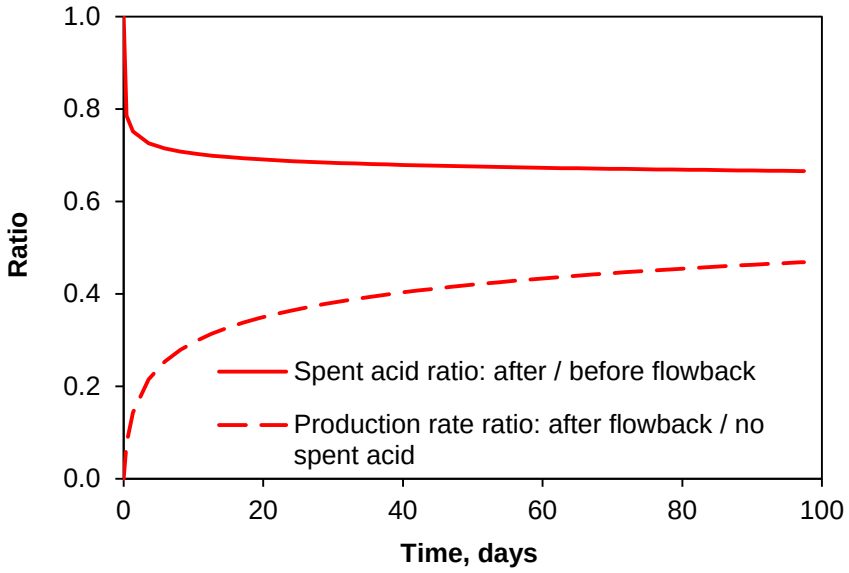

Fig. 5.14 Spent acid and production rate recovery curves for poorly sorted matrix

5.2.4 Effect of wettability

Wettability is another major factor controlling the flow and spatial distribution of fluids in a reservoir. In a rock-fluid system, the wetting phase occupies the small pores and forms a thin film over all the rock surfaces. Meanwhile, the non-wetting phase will

occupy the center of the larger pores. This fluid distribution occurs because it is the most energetically favorable (Anderson, 1987). **Fig. 5.15** is an illustration of how different wetted system performances during a water flooding process.

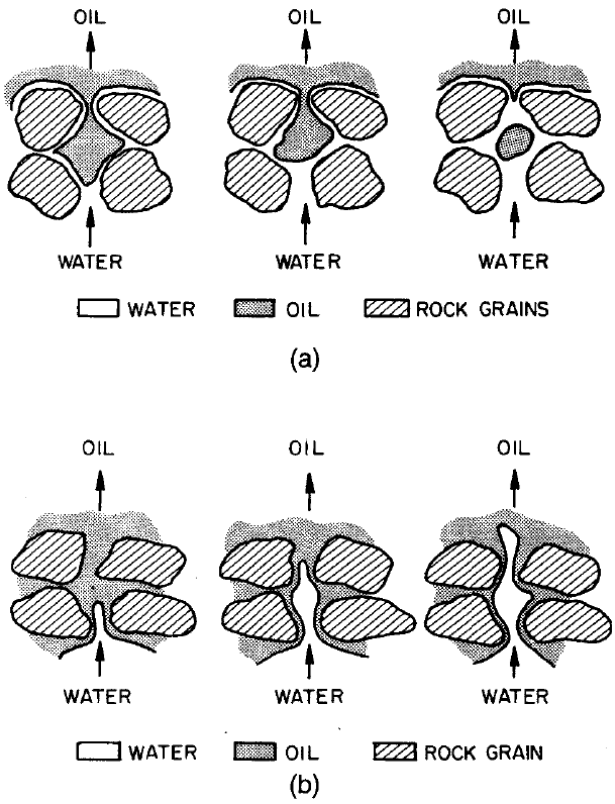

Fig. 5.15 Water displacing oil from a pore during a waterflood: (a) strongly water-wet rock, (b) strongly oil-wet rock (Anderson, 1987)

Typical relative permeability curves for two different wetted systems, strongly water-wet and strongly oil-wet systems, are shown in **Fig. 5.16**. In general, at a given saturation, the relative permeability of a fluid is higher when it is the non-wetting fluid. This occurs because the wetting fluid tends to travel through the smaller, less permeable pores. This explains the end-point relative permeability positions in the figure as well and it helps us to choose reasonable parameters in the following simulations.

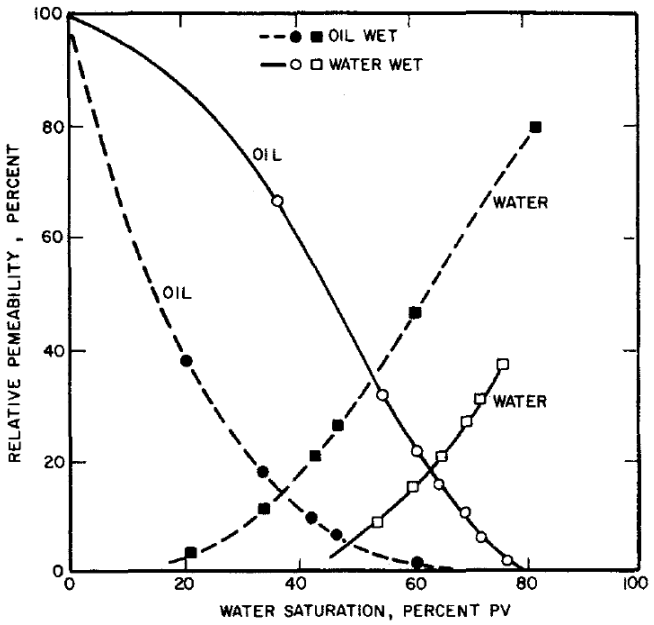

Fig. 5.16 Steady-state oil/water relative permeabilities (Anderson, 1987)

Two systems, liquid-wetted and non-liquid wetted systems, are built to study the effect of wettability on spent acid recovery processes. The parameters used are listed in **Table 5.2**.

Table 5.2 Parameters used for liquid and non-liquid wetted systems

	dp **(psi)**	$k'_{r,w}$	$k'_{r,nw}$	$S_{w,irr}$	$S_{nw,irr}$	n_w	n_{nw}
Liquid wet	**600**	**0.5**	**0.75**	**0.3**	**0.05**	**5**	**2**
Non-liquid wet	**600**	**0.9**	**0.8**	**0.08**	**0.15**	**5**	**2**

Fig. 5.17 and **Fig. 5.18** presented the relative permeability and capillary pressure curves, respectively. We can see that the relative permeability curve in the figure share the similar shapes; however the positions of the curves are shifted for different cases. For the liquid-wetting formation, the liquid phase starts to have zero relative permeability when its saturation is about 0.6. In the capillary pressure figure, the capillary pressure

curve for liquid-wetted formation encloses more area under the curve than the non-liquid wetted formation, which indicates that more external work is needed to displace the same amount of spent acid for the liquid-wetted case according to Eq. 5-4.

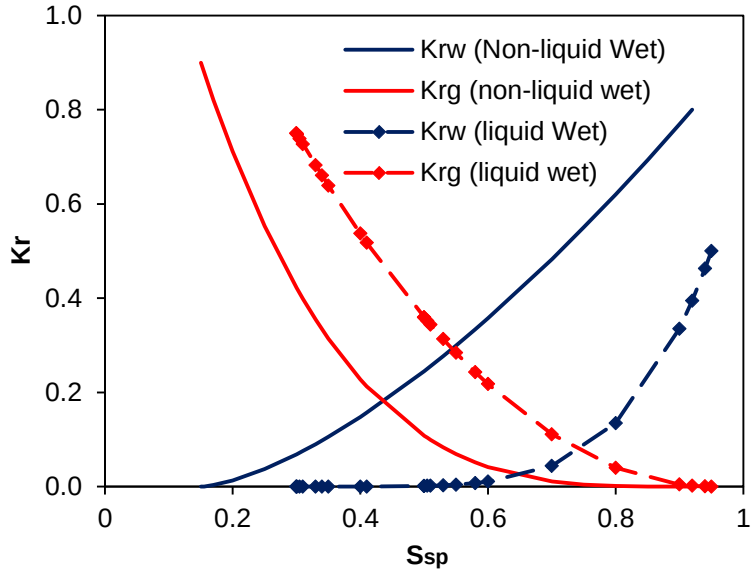

Fig. 5.17 Relative permeability curves for non-liquid wet and liquid wet matrices

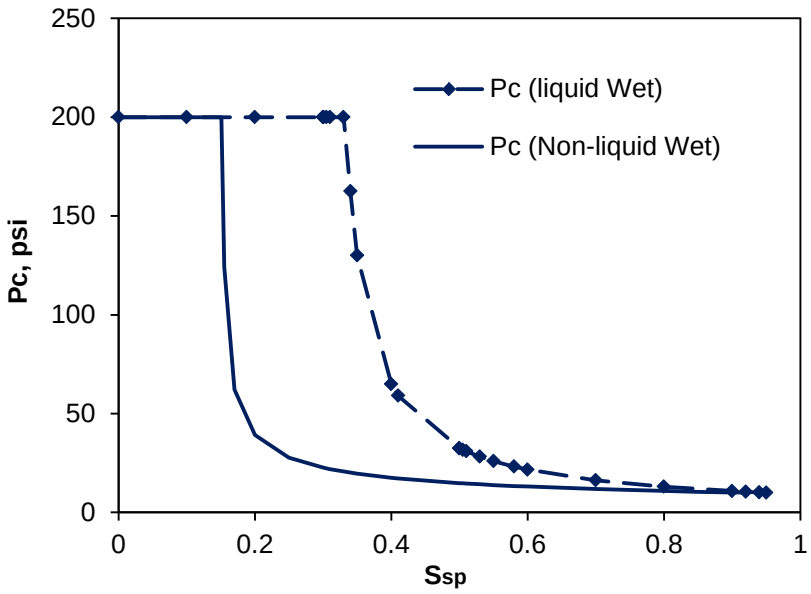

Fig. 5.18 Capillary pressure curves for non-liquid wet and liquid wet matrices

Simulation results for non-liquid and liquid wetted formations are presented in **Fig. 5.19** and **Fig. 5.20**. We can see that the recovery of spent acid in non-liquid wetted formation reached a plateau after about 5 days. After about one month recovery, the recovered production rate is over 95% of the unaffected production rate. Compared to non-liquid wetted formation, the spent acid recovery rate in liquid-wetted formation is slow. In about 3 month recovery, there is still about 65% spent acid left in the formation and the recovered production rate is just over 80%.

Based on the above discussions, it is obvious that to displace spent acid quickly, we prefer spent acid to be the non-wetting phase, i.e. the formation is non-liquid wetted. Most of the reservoirs are considered to be water-wet, although oil-wet reservoirs do exist (Ahr, 2008). The wettability of a formation can be altered during the stimulation process by the flushing actions of stimulation fluids, particularly if the fluid contains surfactants. Changes in wettability have been shown to affect capillary pressure and relative permeability by influencing end-point relative permeability and phase irreducible saturations. This was proved by the experiments and property parameters that are used in simulations in **Chapter 2**. In **Table 2.3**, since the spent acid exponent n_{sp} is smaller than the gas exponent n_{sp}, we know that the core plug in experiment **TxCC 4** was changed to non-liquid wetted core after the acid treatment, while the core plugs in all the other experiment remained liquid wetted. Our experiment results show that using corrosion inhibitor and iron control agent alone will not impede spent acid recovery process. However, besides these two kinds of acid additives, a lot of other additives are also utilized in real field acid stimulations. To guarantee the success of the treatments, these additives should all be tested before they are used.

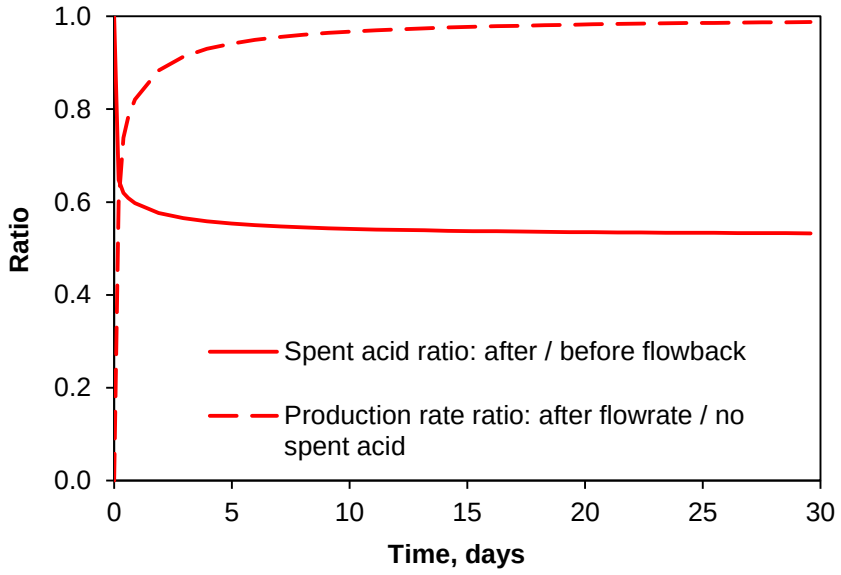

Fig. 5.19 Spent acid and production rate recovery process for non-liquid wetted matrix

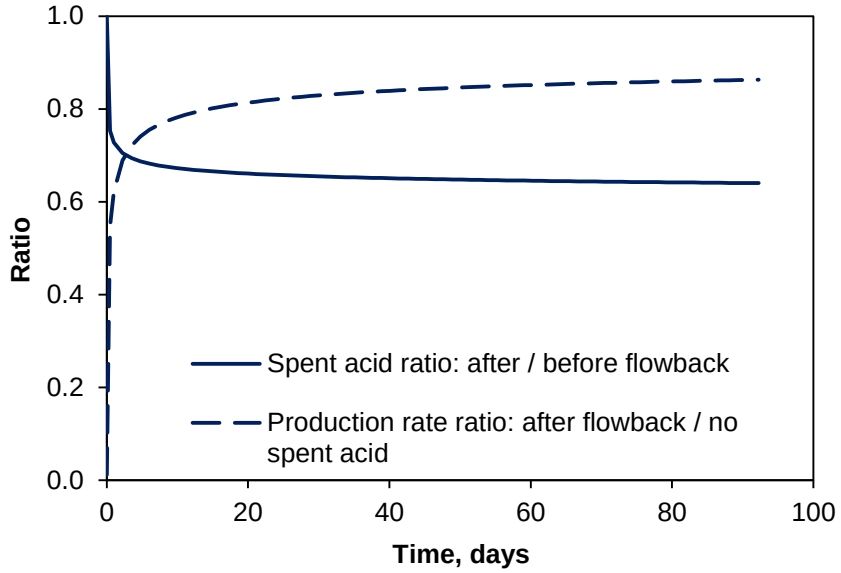

Fig. 5.20 Spent acid and production rate recovery process for liquid wetted matrix

5.2.5 Parametric study results with evaporation included

The foregoing parametric studies consider only the displacement mechanism in the spent acid recovery process and the effects of the evaporation are not taken into account in them. It has been believed that in a water/spent acid blockage phenomenon, if water/spent

acid removal rate is very slow, evaporation will become a comparable process with displacement (Kamath and Laroche, 2000).

First, we present the comparison between the results with and without considering the evaporation mechanism. The parameters used here are mostly the same as before. In **Fig. 5.21**, the spent acid recovery processes are presented. We can see that the spent acid recovery curve for the case without considering evaporation becomes totally flat after about 5 days of gas flowback. It means that at this point the spent acid hit the irreducible saturation in the whole region and is not movable any more. Meanwhile, the spent acid keeps coming out of the simulation domain when evaporation is included. However, in about 15 day gas flowback, only a small portion is recovered by evaporation. The comparison indicates that gas relative permeability could be raised through evaporation. However, it is a very slow process comparing to the displacement regime.

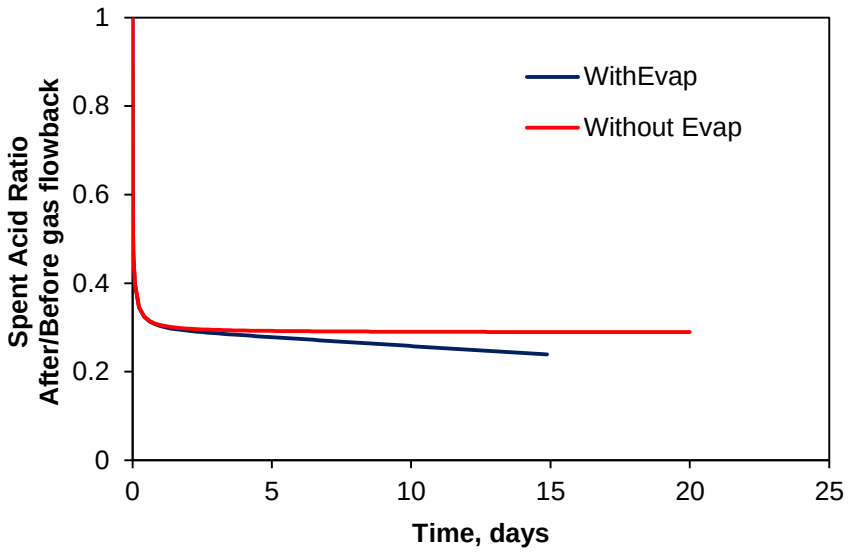

Fig. 5.21 Spent acid recovery process comparison with and without considering evaporation

In the following figures, the spent acid recovery simulation results with evaporation included are presented for different parameters. **Fig. 5.22** shows the results with different

pressure drops. In all the cases, because of the evaporation, spent acid saturations keep going down slowly after the displacement regime finishes. The curve for the highest pressure drop (1000 psi) has a slight larger slope than the other ones, which implies a higher evaporation rate. The reason for this phenomenon is that we use the same outer boundary pressure for all three cases. When a higher pressure drop is used, it results in a lower average pressure in the formation which leads to a higher evaporation rate.

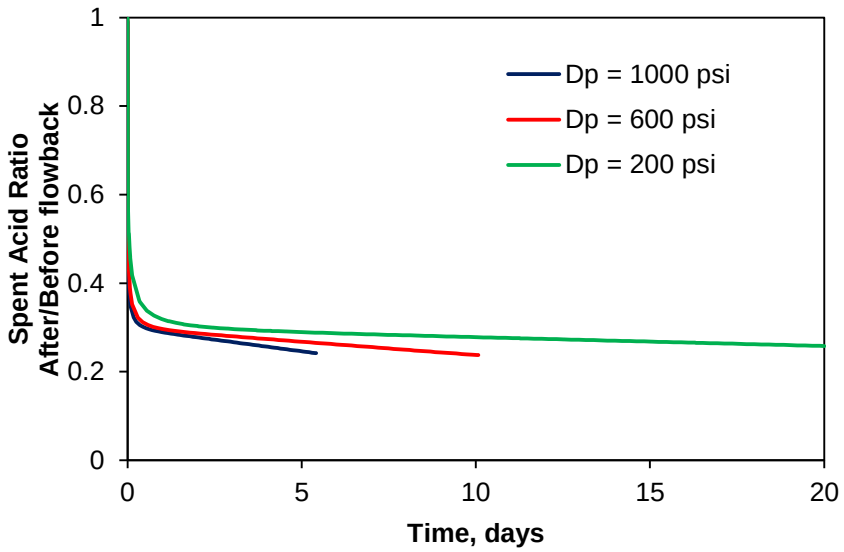

Fig. 5.22 Spent acid recovery processes for different pressure drops considering evaporation

In **Fig. 5.23** and **Fig. 5.24**, we give the results for formations with different pore-size distributions and wetting systems. At specific times, the spent acid values are all slightly smaller than the ones without evaporation mechanism included (**Fig. 5.13** and **Fig. 5.19**). However, we can see that the spent acid contents for poorly sorted formations and liquid wetted system are still high since the evaporation rates are super low. The simulation results with evaporation included all imply that evaporation is a very slow process. Only in the long term, the evaporation may be able to help increase the gas relative permeability.

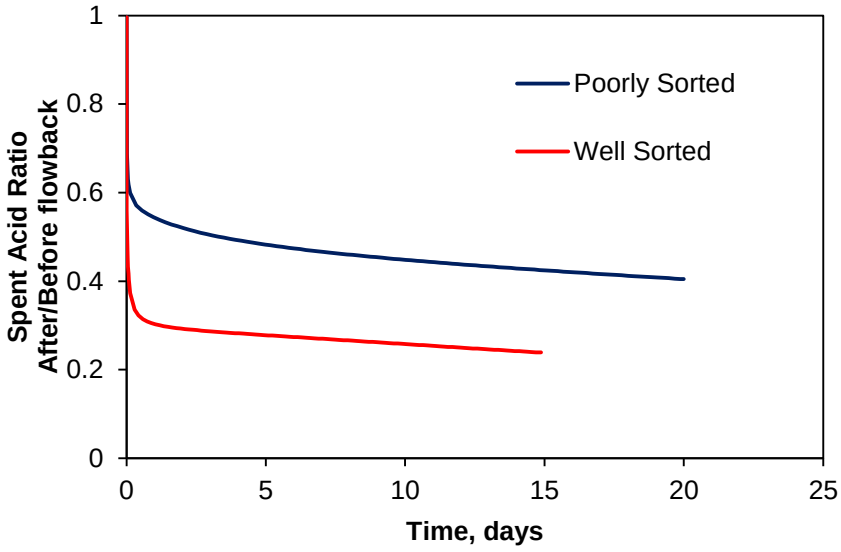

Fig. 5.23 Spent acid recovery processes for differently sorted formations considering evaporation

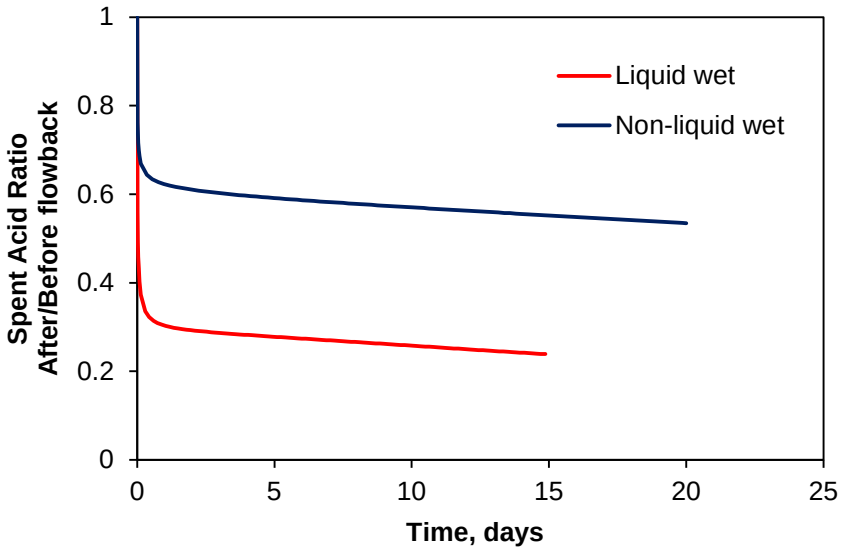

Fig. 5.24 Spent acid recovery processes for different wetted systems considering evaporation

5.3 Chapter Summary

In this chapter, studies are performed to study the effects of different parameters on the spent acid recovery processes. The parameters that are studied include pressure drop, absolute permeability, pore-size distribution and wettability. The simulation results with and without considering evaporation mechanisms are presented separately.

The parametric study indicates that spent acid recovery time increases exponentially with decreasing pressure drop and absolute formation permeability. Besides, formation pore-size distribution and wettability have significant effects on spent acid recovery as well. Well sorted and non-liquid wetted formations are preferred in spent acid recoveries. The evaporation is a slow process and it could help spent acid recovery in the long run. In addition, additives have the potential of changing formation wettabilities and they should be tested before applying to real field acid treatments.

6. CONCLUSIONS

This study presents an integrated experimental and numerical study of spent acid recovery that follows acid stimulations. Our approach combines core flood experiments with 1.5-inch by 20-inch limestone or Texas cream chalks cores, experiment numerical simulations, theoretical calculations of spent acid front penetration, and mathematical modeling of spent acid recovery. Important developments and conclusions can be summarized as:

1. The different experimental tactic of stopping acid injection before wormhole fully penetrates the core samples and addition of dopants in the treatment fluids allow us to observe the spent acid penetration phenomenon. Experiment results indicate that spent acid does penetrate further beyond wormholes. This phenomenon has the potential of blocking the critical matrix surrounding the wellbore and decreasing well productivities in reality.
2. The experiment numerical simulation was introduced to match with the experiment results, by adjusting relative permeability and capillary pressure function parameters. This simulation helps us to obtain the information of the properties that cannot be measured directly from the experiments. The simulation results show that core sample wettability remains liquid-wet when iron control agent is added and changes to non-liquid wet when corrosion inhibitor is utilized.
3. Simplification of a wormhole to half of a slender ellipse eases the mathematical study of spent acid recovery. Spent acid mass balance and the method of characteristics allow us to obtain the spent acid fronts within the acid treatments. The theoretical studies indicate: 1) a slower spent acid penetration rate with increasing stimulation time; 2) a deeper spent acid penetration with smaller formation porosity.

4. A vaporized spent acid/water-gas ratio, R_V, is introduced in our numerical models to calculate the amount of spent acid in the vapor phase at different time steps. This idea borrowed from the modified black oil model is helpful in simulating spent acid recovery process numerically, especially when evaporation is included.
5. Effects of different parameters on spent acid recoveries are studied. It is observed that spent acid recovery and gas production can be recovered to the same level for formations with different pressure drops and absolute permeabilities. However, the time needed to recovery the same amount of spent acid increases exponentially with decreasing pressure drop and absolute formation permeability. Besides, changes in pore-size distribution and formation wettability have noticeable impacts on spent acid recoveries as well. It is very difficult to recover spent acid in poorly sorted and liquid-wetted formations. Spent acid has great potential to cause blockage problem in such formations.
6. This study tells us it is very important to measure and understand formation textures ahead of any stimulation. It is also very important to test the effects of acid additives before real field treatments.

REFERENCES

Ahmadi, M., Sharma, M.M., Pope, G. et al. 2011. Chemical Treatment to Mitigate Condensate and Water Blocking in Gas Wells in Carbonate Reservoirs. SPE Production & Operations, **26** (1), 67-74.

Ahr, W.M. 2008. Geology of Carbonate Reservoirs: The Identification, Description and Characterization of Hydrocarbon Reservoirs in Carbonate Rocks, Wiley.

Al-Anazi, H.A., Okasha, T.M., Haas, M.D. et al. 2005a. Impact of Completion Fluids on Productivity in Gas/Condensate Reservoirs. SPE 94256. SPE Production Operations Symposium, Oklahoma City, Oklahoma, 16-19 April.

Al-Anazi, H.A., Pope, G.A., Sharma, M.M. et al. 2002. Laboratory Measurements of Condensate Blocking and Treatment for Both Low and High Permeability Rocks. SPE 77546. SPE Annual Technical Conference and Exhibition, San Antonio, Texas, 29 September-2 October.

Al-Anazi, H.A., Solares, J.R., and Al-Faifi, M. 2005b. The Impact of Condensate Blockage and Completion Fluids on Gas Productivity in Gas-Condensate Reservoir. SPE 93210. SPE Asia Pacific Oil and Gas Conference and Exhibition, Jakarta, Indonesia, 5-7 April.

Al-Anazi, H.A., Walker, J.G., Pope, G.A. et al. 2005c. A Successful Methanol Treatment in a Gas/Condensate Reservoir: Field Application. SPE Production & Operations, **20** (1), 60-69.

Anderson, W.G. 1987. Wettability Literature Survey Part 5: The Effects of Wettability on Relative Permeability. Journal of Petroleum Technology, **39** (11), 1453-1468.

Bahrami, H., Rezaee, M.R., Nazhat, D.H. et al. 2011. Effect of Water Blocking Damage on Flow Efficiency and Productivity in Tight Gas Reservoirs. SPE 142283. SPE Production and Operations Symposium, Oklahoma City, Oklahoma, 27-29 March.

Bang, V.S.S., Pope, G.A., Sharma, M.M. et al. 2009. Development of a Successful Chemical Treatment for Gas Wells with Water and Condensate Blocking Damage. SPE 124977. SPE Annual Technical Conference and Exhibition, New Orleans, Louisiana, 4-7 October.

Barrett, J.F. and Keat, N. 2004. Artifacts in CT: Recognition and Avoidance. Radiographics, **24** (6), 1679-1691.

Bazin, B., Peysson, Y., Lamy, F. et al. 2010. In-Situ Water-Blocking Measurements and Interpretation Related to Fracturing Operations in Tight Gas Reservoirs. SPE Production & Operations, **25** (4), 431-437.

Bennion, D.B., Bietz, R.F., Thomas, F.B. et al. 1994. Reductions in the Productivity of Oil and Low Permeability Gas Reservoirs Due to Aqueous Phase Trapping. Journal of Canadian Petroleum Technology, **33** (9), 45-54.

Bennion, D.B. and Thomas, F.B. 2005. Formation Damage Issues Impacting the Productivity of Low Permeability, Low Initial Water Saturation Gas Producing Formations. Journal of Energy Resources Technology, **127** (3), 240-247.

Bennion, D.B., Thomas, F.B., and Bietz, R.F. 1996. Low Permeability Gas Reservoirs: Problems, Opportunities and Solutions for Drilling, Completion, Stimulation and Production. SPE 35577. SPE Gas Technology Symposium, Calgary, Alberta, Canada, 28 April-1 May.

Bette, S. and Heinemann, R.F. 1989. Compositional Modeling of High-Temperature Gas-Condensate Reservoirs with Water Vaporization. SPE18422. SPE Symposium on Reservoir Simulation, Houston, Texas, 6-8 February.

Blasingame, T.A., Amini, S., and Rushing, J. 2007. Evaluation of the Elliptical Flow Period for Hydraulically-Fractured Wells in Tight Gas Sands-Theoretical Aspects and Practical Considerations. SPE 106308. SPE Hydraulic Fracturing Technology Conference, College Station, Texas, 29-31 January.

Brooks, R.H. and Corey, A.T. 1964. Hydraulic Properties of Porous Media. Hydrology Papers (Colorado State University) **3**.

Buijse, M.A. and Glasbergen, G. 2005. A Semi-Empirical Model to Calculate Wormhole Growth in Carbonate Acidizing. SPE 96892. SPE Annual Technical Conference and Exhibition, Dallas, Texas, 9-12 October.

Butler, M., Trueblood, J.B., Pope, G.A. et al. 2009. A Field Demonstration of a New Chemical Stimulation Treatment for Fluid-Blocked Gas Wells. SPE 125077. SPE Annual Technical Conference and Exhibition, New Orleans, Louisiana, 4-7 October.

Cao, H. 2002. Development of Techniques for General Purpose Simulators. Doctoral dissertation. Stanford University.

Chau, K. and Jiang, Y. 2001. 3D Numerical Model for Pearl River Estuary. Journal of Hydraulic Engineering, **127** (1), 72-82.

Coats, K.H. 1985. Simulation of Gas Condensate Reservoir Performance. Journal of Petroleum Technology, **37** (10), 1870-1886.

Collins, D.A., Nghiem, L.X., Sharma, R. et al. 1991. Field-Scale Simulation of Horizontal Wells with Hybrid Grids. SPE 21218. SPE Symposium on Reservoir Simulation, Anaheim, California, 17-20 February.

Collins, R.E. 1961. Flow of Fluids through Porous Materials: R.E.Collins. Petroleum Publishing Company.

Crain, E.R. Crain's Petrophysical Handbook. http://www.spec2000.net/12-phibasics.htm.

Culberson, O.L. and Mcketta Jr., J.J. 1951. Phase Equilibria in Hydrocarbon-Water Systems III - the Solubility of Methane in Water at Pressures to 10,000 Psia. Journal of Petroleum Technology, **3** (8), 223-226.

Duan, Z. and Mao, S. 2006. A Thermodynamic Model for Calculating Methane Solubility, Density and Gas Phase Composition of Methane-Bearing Aqueous

Fluids from 273 to 523 K and from 1 to 2000 Bar. Geochimica et Cosmochimica Acta, **70** (13), 3369-3386.

El-Banbi, A.H., Fattah, K.A., and Sayyouh, H. 2006. New Modified Black-Oil Correlations for Gas Condensate and Volatile Oil Fluids. SPE 102240. SPE Annual Technical Conference and Exhibition, San Antonio, Texas, 24-27 September.

El-Banbi, A.H., Forrest, J.K., Fan, L. et al. 2000a. Producing Rich-Gas-Condensate Reservoirs - Case History and Comparison between Compositional and Modified Black-Oil Approaches. SPE 58988. SPE International Petroleum Conference and Exhibition in Mexico, Villahermosa, Mexico, 1-3 February.

El-Banbi, A.H., W.D. Mccain, J., and Semmelbeck, M.E. 2000b. Investigation of Well Productivity in Gas-Condensate Reservoirs. SPE 59773. SPE/CERI Gas Technology Symposium, Calgary, Alberta, Canada, 3-5 April.

Ertekin, T., Abou-Kassem, J.H., and King, G.R. 2001. Basic Applied Reservoir Simulation. Henry L. Doherty Memorial Fund of AIME, Society of Petroleum Engineers.

Fahes, M.M. and Firoozabadi, A. 2007. Wettability Alteration to Intermediate Gas-Wetting in Gas-Condensate Reservoirs at High Temperatures. SPE Journal, **12** (4), 397-407.

Furui, K., Burton, R.C., Burkhead, D.W. et al. 2010. A Comprehensive Model of High-Rate Matrix Acid Stimulation for Long Horizontal Wells in Carbonate Reservoirs. SPE 134265. SPE Annual Technical Conference and Exhibition, Florence, Italy, 19-22 September.

Goldman, L.W. 2007. Principles of CT and CT Technology. Journal of Nuclear Medicine Technology, **35** (3), 115-128.

Hill, A.D., Zhang, Q., and Zhu, D. 2013. Modeling of Spent-Acid Blockage Damage in Stimulated Gas Wells. IPTC 16481. International Petroleum Technology Conference, Beijing, China, 26-28 March.

Hoffman, J.D. and Frankel, S. 2001. Numerical Methods for Engineers and Scientists, Second Edition. Taylor & Francis.

Honarpour, M. and Mahmood, S.M. 1988. Relative-Permeability Measurements: An Overview. Journal of Petroleum Technology, **40** (8), 963-966.

Humphreys, N.V. 1991. The Material Balance Equation for a Gas Condensate Reservoir with Significant Water Vaporization. SPE 21514. SPE Gas Technology Symposium, Houston, Texas, 22-24 January.

Izgec, O. 2009. Reactive Flow in Vuggy Carbonates: Methods and Models Applied to Matrix Acidizing of Carbonates. Doctoral dissertation. Texas A&M University.

Kamath, J. and Laroche, C. 2003. Laboratory-Based Evaluation of Gas Well Deliverability Loss Caused by Water Blocking. SPE Journal, **8** (1), 71-80.

Kamath, J. and Laroche, C. 2000. Laboratory Based Evaluation of Gas Well Deliverability Loss Due to Waterblocking. SPE 63161. SPE Annual Technical Conference and Exhibition, Dallas, Texas, 1-4 October.

Kravets, S. 2012. Stochastic Modelling of the Reservoir Lithological and Petrophysical Attributes. A Case Study of the Middle East Carbonate Reservoir. Doctoral dissertation. Faculdade de Ciências e Tecnologia.

Kucuk, F. and Brigham, W.E. 1979. Transient Flow in Elliptical Systems. Society of Petroleum Engineers Journal, **19** (6), 401-410.

Kumar, V., Pope, G.A., and Sharma, M.M. 2006. Improving the Gas and Condensate Relative Permeability Using Chemical Treatments. SPE 100529. SPE Gas Technology Symposium, Calgary, Alberta, Canada, 15-17 May.

Kurihara, M., Liang, J., Fujimoto, F. et al. 2000. Development and Application of Underground Gas Storage Simulator. SPE 59438. SPE Asia Pacific Conference on Integrated Modelling for Asset Management, Yokohama, Japan, 25-26 April.

Li, K. and Firoozabadi, A. 2000. Experimental Study of Wettability Alteration to Preferential Gas-Wetting in Porous Media and Its Effects. SPE Reservoir Evaluation & Engineering, **3** (2), 139-149.

Liao, Y. and Lee, W.J. 1993. New Solutions for Wells with Finite-Conductivity Fractures Including Wellbore Storage and Fracture-Face Skin. SPE 26912. SPE Eastern Regional Meeting, Pittsburgh, Pennsylvania, 2-4 November.

Ma, S. and Morrow, N. 1996. Relationships between Porosity and Permeability for Porous Rocks. Paper 9610. International Symposium of the Society of Core Analysis, Montpelier, France, 8-10 September.

Mahadevan, J. and Sharma, M.M. 2003. Clean-up of Water Blocks in Low Permeability Formations. SPE 84216. SPE Annual Technical Conference and Exhibition, Denver, Colorado, 5-8 October.

Mahadevan, J., Sharma, M.M., and Yortsos, Y.C. 2007a. Capillary Wicking in Gas Wells. SPE Journal, **12** (4), 429-437.

Mahadevan, J., Sharma, M.M., and Yortsos, Y.C. 2007b. Evaporative Cleanup of Water Blocks in Gas Wells. SPE Journal, **12** (2), 209-216.

Mcduff, D., Jackson, S., Shuchart, C. et al. 2010a. Understanding Wormholes in Carbonates: Unprecedented Experimental Scale and 3D Visualization. Journal of Petroleum Technology, **62** (10), 78-81.

Mcduff, D., Shuchart, C.E., Jackson, S. et al. 2010b. Understanding Wormholes in Carbonates: Unprecedented Experimental Scale and 3-D Visualization. SPE 134379. SPE Annual Technical Conference and Exhibition, Florence, Italy, 19-22 September.

Mcleod, H.O. and Coulter, A.W. 1966a. The Use of Alcohol in Gas Well Stimulation. SPE 1663. SPE Eastern Regional Meeting, Columbus, Ohio, 10-11 November.

Mcleod, H.O., Mcginty, J.E., and Smith, C.F. 1966b. Deep Well Stimulation with Alcoholic Acid. SPE 1558. Fall Meeting of the Society of Petroleum Engineers of AIME, Dallas, Texas, 2-5 October.

Monteagudo, J.E.P. and Firoozabadi, A. 2007. Comparison of Fully Implicit and Impes Formulations for Simulation of Water Injection in Fractured and Unfractured Media. International Journal for Numerical Methods in Engineering, **69** (4), 698-728.

Nasir, E. 2012. Effects of Acid Additives on Spent Acid Flowback through Carbonate Cores. Master's thesis. Texas A&M University.

Nevito G., J. 2006. Design, Set up, and Testing of a Matrix Acidizing Apparatus. Master's Thesis. Texas A&M University.

Panga, M.K.R., Ooi, Y.S., Koh, P.L. et al. 2006. Wettability Alteration for Water-Block Prevention in High-Temperature Gas Wells. SPE 100182. SPE Europec/EAGE Annual Conference and Exhibition, Vienna, Austria, 12-15 June.

Parekh, B. and Sharma, M.M. 2004. Cleanup of Water Blocks in Depleted Low-Permeability Reservoirs. SPE 89837. SPE Annual Technical Conference and Exhibition, Houston, Texas, 26-29 September.

Penny, G.S., Conway, M.W., and Briscoe, J.E. 1983. Enhanced Load Water-Recovery Technique Improves Stimulation Results. SPE 12149. SPE Annual Technical Conference and Exhibition, San Francisco, California, 5-8 October.

Sharma, P., G. Mamgain, and V.K. Bahuguna. 2011. Improved Permeability Estimates in Carbonate Reservoirs Using Electrofacies Characterization: A Case Study of Mumbai High South. The 2nd South Asain Geoscience Conference and Exhibition, New Delhi, India, 12-14 January.

Rae, P. and Lullo, G.D. 2003. Matrix Acid Stimulation-A Review of the State-of-the-Art. SPE 82260. SPE European Formation Damage Conference, The Hague, Netherlands, 13-14 May.

Rigby, M. and Prausnitz, J.M. 1968. Solubility of Water in Compressed Nitrogen, Argon, and Methane. The Journal of Physical Chemistry, **72** (1), 330-334.

Riley, M.F., Brigham, W.E., and Horne, R.N. 1991a. Analytic Solutions for Elliptical Finite-Conductivity Fractures. SPE 22656. SPE Annual Technical Conference and Exhibition, Dallas, Texas, 6-9 October.

Riley, M.F. 1991b. Finite Conductivity Fractures in Elliptical Coordinates. Doctoral dissertation. Stanford University.

Saneifar, M. 2011. The Effect of Acid Additives on Carbonate Rock Wettability and Spent Acid Recovery in Low Permeability Gas Carbonates. Master's thesis. Texas A&M University.

Schechter, R.S. 1992. Oil Well Stimulation. Prentice Hall.

Schlumberger. 2011. Eclipse Reservoir Simulation Software Reference Manual.

Schon, J.R. 2011. Physical Properties of Rocks. Elsevier Science & Technology Book.

Shibue, Y. 2003. Vapor Pressures of Aqueous Nacl and $CaCl_2$ Solutions at Elevated Temperatures. Fluid Phase Equilibria, **213** (1–2), 39-51.

Shukla, S., Zhu, D., and Hill, A.D. 2006. The Effect of Phase Saturation Conditions on Wormhole Propagation in Carbonate Acidizing. SPE Journal, **11** (3), 273-281.

Skjaeveland, S.M., Siqveland, L.M., Kjosavik, A. et al. 2000. Capillary Pressure Correlation for Mixed-Wet Reservoirs. SPE Reservoir Evaluation & Engineering, **3** (1), 60-67.

Spivak, A. and Dixon, T.N. 1973. Simulation of Gas-Condensate Reservoirs. SPE 4271. SPE Symposium on Numerical Simulation of Reservoir Performance, Houston, Texas, 11-12 January.

Tang, G.-Q. and Firoozabadi, A. 2003. Wettability Alteration to Intermediate Gas-Wetting in Porous Media at Elevated Temperatures. Transport in Porous Media, **52** (2), 185-211.

Tang, G.-Q. and Firoozabadi, A. 2002. Relative Permeability Modification in Gas/Liquid Systems through Wettability Alteration to Intermediate Gas Wetting. SPE Reservoir Evaluation & Engineering, **5** (6), 427-436.

Valsecchi, P., Mcduff, D., Chang, D.-L. et al. 2012. Simulation and Visualization of near-Well Flow. SPE 157028. SPE International Production and Operations Conference & Exhibition, Doha, Qatar, 14-16 May.

Wagner, W. and Pruss, A. 1993. International Equations for the Saturation Properties of Ordinary Water Substance. Revised According to the International Temperature Scale of 1990. Addendum to J. Phys. Chem. Ref. Data, 893 (1987). Journal of Physical and Chemical Reference Data, **22** (3), 783-787.

Wang, Y., Hill, A.D., and Schechter, R.S. 1993. The Optimum Injection Rate for Matrix Acidizing of Carbonate Formations. SPE 26578. SPE Annual Technical Conference and Exhibition, Houston, Texas, 3-6 October.

Withjack, E.M. 1988. Computed Tomography for Rock-Property Determination and Fluid-Flow Visualization. SPE Formation Evaluation, **3** (4), 696-704.

Xie, X., Liu, Y., Sharma, M.M. et al. 2008. Wettability Alteration to Increase Deliverability of Gas-Production Wells. SPE 117353. SPE Eastern Regional/AAPG Eastern Section Joint Meeting, Pittsburgh, Pennsylvania, 11-15 October.

Yarrison, M., Cox, K.R., and Chapman, W.G. 2006. Measurement and Modeling of the Solubility of Water in Supercritical Methane and Ethane from 310 to 477 K and Pressures from 3.4 to 110 MPa. Industrial & Engineering Chemistry Research, **45** (20), 6770-6777.

Yuster, S.T. 1946. The Rehabilitation of Drowned Gas Wells. API-46-209. Drilling and Production Practice.

Zuluaga, E. and Lake, L.W. 2008. Modeling of Experiments on Water Vaporization for Gas Injection Using Traveling Waves. SPE Journal, **13** (2), 248-256.

Zuluaga, E. and Lake, L.W. 2004. Modeling of Experiments on Water Vaporization for Gas Injection. SPE 91393. SPE Eastern Regional Meeting, Charleston, West Virginia, 15-17 September.

Zuluaga, E. and Monsalve, J.C. 2003. Water Vaporization in Gas Reservoirs. SPE 84829. SPE Eastern Regional Meeting, Pittsburgh, Pennsylvania, 6-10 September.

Zuluaga, E., Munoz, N.I., and Obando, G.A. 2001. An Experimental Study to Evaluate Water Vaporisation and Formation Damage Caused by Dry Gas Flow through Porous Media. SPE 68335. International Symposium on Oilfield Scale, Aberdeen, United Kingdom, 30-31 January.

APPENDIX A

Sample ECLIPSE input file for experiment simulation study

```
RUNSPEC
=========================================================================
TITLE
Experiment Simulation Input File

DIMENS
--   NX   NY   NZ
       179   38     1 /

--    Phases
WATER
GAS

--   Requested formatted output files
UNIFOUT

--   Field unit is used
FIELD

TABDIMS
1     1     20   20    1   20 /

WELLDIMS              -- / For memory allocation only
50    50    50    50 /

START
1 'JAN' 1983 /

NSTACK
50/

GRID
=========================================================================
EQUALS
 'DX'    1.32          1   106   1   38   1    1 /
 'DX'    2.64        107   179   1   38   1    1 /
/

EQUALS
'DY'    0.66           1   179   1   38   1    1 /
/
```

```
DZ
6802*1.32 /

TOPS
6802*4000.0 /

PORO
6802*0.15 /

PERMX
6802*3.0 /

PERMY
6802*3.0 /

PERMZ
6802*3.0 /

--   BOX panel edit: PERMX multiplied by 1000000 for box (1:106, 19:20, 1:1)
BOX
1   106     19   20     1   1 /
MULTIPLY
PERMX    1000000 /
/
ENDBOX

BOX
1   179     1   38     1   1 /
COPY
--  From          To
  PERMX    PERMY /
/
ENDBOX

BOX
1   179     1   38     1   1 /
COPY
--  From          To
  PERMX     PERMZ /
/
ENDBOX

PROPS
================================================================
RVCONST
```

```
 0.01 /
SGWFN
0.001          0                0.5              2
0.04           1.24652E-05      0.38605156       2.096296296
0.08           0.000147458      0.292197635      2.205194805
0.1            0.000324861      0.25282188       2.264
0.15           0.001358708      0.172988379      2.425714286
0.2            0.003740762      0.115080349      2.612307692
0.3            0.015553334      0.045916894      3.087272727
0.4            0.042695241      0.015228129      3.773333333
0.5            0.093395563      0.003822539      4.851428571
0.6            0.17699794       0.000600686      6.792
0.65           0.234331554      0.000176053      8.49
0.7            0.303839652      3.61809E-05      11.32
0.75           0.386955208      3.89025E-06      16.98
0.85           0.6              1.06759E-91      200
/

PVTW
 0.0      1.0       3.03E-06        .5        0.0 /

PVDG
400.000        5.9000          .01300
800.000        2.9500          .01350
1200.00        1.9600          .01400
1600.00        1.4700          .01450
2000.00        1.1800          .01500
2400.00        .98000          .01550
2800.00        .84000          .01600
3200.00        .74000          .01650
3600.00        .65000          .01700
4000.00        .59000          .01750
4400.00        .54000          .01800
4800.00        .49000          .01850
5200.00        .45000          .01900
5600.00        .42000          .01950 /

ROCK
 4000.0         .30E-05 /

DENSITY
 52.0000   64.0000   .04400 /

RPTPROPS
/
```

```
REGIONS
=============================================================
SATNUM
6802*1 /
IMBNUM
6802*1 /

SOLUTION
=============================================================
DEBUG
2         4 /

EQUALS
'SWAT'   1.00          1   106   1   38   1   1  /
'SWAT'   0.99        107   107   1   38   1   1  /
'SWAT'   0.98        108   108   1   38   1   1  /
'SWAT'   0.97        109   109   1   38   1   1  /
'SWAT'   0.96        110   110   1   38   1   1  /
'SWAT'   0.94        111   111   1   38   1   1  /
'SWAT'   0.91        112   112   1   38   1   1  /
'SWAT'   0.834       113   113   1   38   1   1  /
'SWAT'   0.733       114   114   1   38   1   1  /
'SWAT'   0.5459      115   115   1   38   1   1  /
'SWAT'   0.2638      116   116   1   38   1   1  /
'SWAT'   0.1926      117   117   1   38   1   1  /
'SWAT'   0.167       118   118   1   38   1   1  /
'SWAT'   0.1538      119   119   1   38   1   1  /
'SWAT'   0.095       120   120   1   38   1   1  /
'SWAT'   0.0         121   179   1   38   1   1  /
/

PRVD
4000    3800
5000    4150 /

SUMMARY
=============================================================
BSWAT
/
FGIT
/

SCHEDULE
=============================================================
WELSPECS
'I1'     'G'     179      1      4000.66      'GAS'  /
```

```
'I2'    'G'    179    2    4000.66    'GAS'  /
'I3'    'G'    179    3    4000.66    'GAS'  /
'I4'    'G'    179    4    4000.66    'GAS'  /
'I5'    'G'    179    5    4000.66    'GAS'  /
'I6'    'G'    179    6    4000.66    'GAS'  /
'I7'    'G'    179    7    4000.66    'GAS'  /
'I8'    'G'    179    8    4000.66    'GAS'  /
'I9'    'G'    179    9    4000.66    'GAS'  /
'I10'   'G'    179    10   4000.66    'GAS'  /
'I11'   'G'    179    11   4000.66    'GAS'  /
'I12'   'G'    179    12   4000.66    'GAS'  /
'I13'   'G'    179    13   4000.66    'GAS'  /
'I14'   'G'    179    14   4000.66    'GAS'  /
'I15'   'G'    179    15   4000.66    'GAS'  /
'I16'   'G'    179    16   4000.66    'GAS'  /
'I17'   'G'    179    17   4000.66    'GAS'  /
'I18'   'G'    179    18   4000.66    'GAS'  /
'I19'   'G'    179    19   4000.66    'GAS'  /
'I20'   'G'    179    20   4000.66    'GAS'  /
'I21'   'G'    179    21   4000.66    'GAS'  /
'I22'   'G'    179    22   4000.66    'GAS'  /
'I23'   'G'    179    23   4000.66    'GAS'  /
'I24'   'G'    179    24   4000.66    'GAS'  /
'I25'   'G'    179    25   4000.66    'GAS'  /
'I26'   'G'    179    26   4000.66    'GAS'  /
'I27'   'G'    179    27   4000.66    'GAS'  /
'I28'   'G'    179    28   4000.66    'GAS'  /
'I29'   'G'    179    29   4000.66    'GAS'  /
'I30'   'G'    179    30   4000.66    'GAS'  /
'I31'   'G'    179    31   4000.66    'GAS'  /
'I32'   'G'    179    32   4000.66    'GAS'  /
'I33'   'G'    179    33   4000.66    'GAS'  /
'I34'   'G'    179    34   4000.66    'GAS'  /
'I35'   'G'    179    35   4000.66    'GAS'  /
'I36'   'G'    179    36   4000.66    'GAS'  /
'I37'   'G'    179    37   4000.66    'GAS'  /
'I38'   'G'    179    38   4000.66    'GAS'  /

'P1'  'G'   1    19  4000.66    'GAS'  /
'P2'  'G'   1    20  4000.66    'GAS'  /
/

COMPDAT
'I1     '    179   1    1   1   'OPEN'   0   .0    0.002 /
'I2     '    179   2    1   1   'OPEN'   0   .0    0.002 /
'I3     '    179   3    1   1   'OPEN'   0   .0    0.002 /
```

```
'I4     '    179   4     1   1    'OPEN'    0    .0    0.002 /
'I5     '    179   5     1   1    'OPEN'    0    .0    0.002 /
'I6     '    179   6     1   1    'OPEN'    0    .0    0.002 /
'I7     '    179   7     1   1    'OPEN'    0    .0    0.002 /
'I8     '    179   8     1   1    'OPEN'    0    .0    0.002 /
'I9     '    179   9     1   1    'OPEN'    0    .0    0.002 /
'I10    '    179   10    1   1    'OPEN'    0    .0    0.002 /
'I11    '    179   11    1   1    'OPEN'    0    .0    0.002 /
'I12    '    179   12    1   1    'OPEN'    0    .0    0.002 /
'I13    '    179   13    1   1    'OPEN'    0    .0    0.002 /
'I14    '    179   14    1   1    'OPEN'    0    .0    0.002 /
'I15    '    179   15    1   1    'OPEN'    0    .0    0.002 /
'I16    '    179   16    1   1    'OPEN'    0    .0    0.002 /
'I17    '    179   17    1   1    'OPEN'    0    .0    0.002 /
'I18    '    179   18    1   1    'OPEN'    0    .0    0.002 /
'I19    '    179   19    1   1    'OPEN'    0    .0    0.002 /
'I20    '    179   20    1   1    'OPEN'    0    .0    0.002 /
'I21    '    179   21    1   1    'OPEN'    0    .0    0.002 /
'I22    '    179   22    1   1    'OPEN'    0    .0    0.002 /
'I23    '    179   23    1   1    'OPEN'    0    .0    0.002 /
'I24    '    179   24    1   1    'OPEN'    0    .0    0.002 /
'I25    '    179   25    1   1    'OPEN'    0    .0    0.002 /
'I26    '    179   26    1   1    'OPEN'    0    .0    0.002 /
'I27    '    179   27    1   1    'OPEN'    0    .0    0.002 /
'I28    '    179   28    1   1    'OPEN'    0    .0    0.002 /
'I29    '    179   29    1   1    'OPEN'    0    .0    0.002 /
'I30    '    179   30    1   1    'OPEN'    0    .0    0.002 /
'I31    '    179   31    1   1    'OPEN'    0    .0    0.002 /
'I32    '    179   32    1   1    'OPEN'    0    .0    0.002 /
'I33    '    179   33    1   1    'OPEN'    0    .0    0.002 /
'I34    '    179   34    1   1    'OPEN'    0    .0    0.002 /
'I35    '    179   35    1   1    'OPEN'    0    .0    0.002 /
'I36    '    179   36    1   1    'OPEN'    0    .0    0.002 /
'I37    '    179   37    1   1    'OPEN'    0    .0    0.002 /
'I38    '    179   38    1   1    'OPEN'    0    .0    0.002 /

'P1     '    1     19    1   1    'OPEN'    0    .0    0.002 /
'P2     '    1     20    1   1    'OPEN'    0    .0    0.002 /
/

WCONPROD
'P1'    'OPEN'    'BHP'    5*    3200.0 /
'P2'    'OPEN'    'BHP'    5*    3200.0 /
/

WCONINJE
```

```
'I1'    'GAS'    'OPEN'    'BHP'    2*    5325.0 /
'I2'    'GAS'    'OPEN'    'BHP'    2*    5325.0 /
'I3'    'GAS'    'OPEN'    'BHP'    2*    5325.0 /
'I4'    'GAS'    'OPEN'    'BHP'    2*    5325.0 /
'I5'    'GAS'    'OPEN'    'BHP'    2*    5325.0 /
'I6'    'GAS'    'OPEN'    'BHP'    2*    5325.0 /
'I7'    'GAS'    'OPEN'    'BHP'    2*    5325.0 /
'I8'    'GAS'    'OPEN'    'BHP'    2*    5325.0 /
'I9'    'GAS'    'OPEN'    'BHP'    2*    5325.0 /
'I10'   'GAS'    'OPEN'    'BHP'    2*    5325.0 /
'I11'   'GAS'    'OPEN'    'BHP'    2*    5325.0 /
'I12'   'GAS'    'OPEN'    'BHP'    2*    5325.0 /
'I13'   'GAS'    'OPEN'    'BHP'    2*    5325.0 /
'I14'   'GAS'    'OPEN'    'BHP'    2*    5325.0 /
'I15'   'GAS'    'OPEN'    'BHP'    2*    5325.0 /
'I16'   'GAS'    'OPEN'    'BHP'    2*    5325.0 /
'I17'   'GAS'    'OPEN'    'BHP'    2*    5325.0 /
'I18'   'GAS'    'OPEN'    'BHP'    2*    5325.0 /
'I19'   'GAS'    'OPEN'    'BHP'    2*    5325.0 /
'I20'   'GAS'    'OPEN'    'BHP'    2*    5325.0 /
'I21'   'GAS'    'OPEN'    'BHP'    2*    5325.0 /
'I22'   'GAS'    'OPEN'    'BHP'    2*    5325.0 /
'I23'   'GAS'    'OPEN'    'BHP'    2*    5325.0 /
'I24'   'GAS'    'OPEN'    'BHP'    2*    5325.0 /
'I25'   'GAS'    'OPEN'    'BHP'    2*    5325.0 /
'I26'   'GAS'    'OPEN'    'BHP'    2*    5325.0 /
'I27'   'GAS'    'OPEN'    'BHP'    2*    5325.0 /
'I28'   'GAS'    'OPEN'    'BHP'    2*    5325.0 /
'I29'   'GAS'    'OPEN'    'BHP'    2*    5325.0 /
'I30'   'GAS'    'OPEN'    'BHP'    2*    5325.0 /
'I31'   'GAS'    'OPEN'    'BHP'    2*    5325.0 /
'I32'   'GAS'    'OPEN'    'BHP'    2*    5325.0 /
'I33'   'GAS'    'OPEN'    'BHP'    2*    5325.0 /
'I34'   'GAS'    'OPEN'    'BHP'    2*    5325.0 /
'I35'   'GAS'    'OPEN'    'BHP'    2*    5325.0 /
'I36'   'GAS'    'OPEN'    'BHP'    2*    5325.0 /
'I37'   'GAS'    'OPEN'    'BHP'    2*    5325.0 /
'I38'   'GAS'    'OPEN'    'BHP'    2*    5325.0 /
/

TUNING
0.005    0.005    0.0005    1*    1.0 /
    /
2*100   /

TSTEP
```

200*0.01 /

END

APPENDIX B

The method for solving Cubic Equations

For a cubic equation,

$$ax^3 + bx^2 + c + d = 0 \quad \text{(B-1)}$$

We define,

$$f = \frac{(3c/a) - (b^2/a^2)}{3} \quad \text{(B-2)}$$

$$g = \frac{(2b^2/a^3) - (9bc/a^2) + (27d/a)}{27} \quad \text{(B-3)}$$

$$h = (g^2/4) + (f^3/27) \quad \text{(B-4)}$$

When $h \le 0$, all 3 roots are real and we proceed as follows,

$$x_1 = -\frac{2f}{3}\cos\left(\frac{9g}{2f^3}\right) - \frac{b}{3a} \quad \text{(B-5)}$$

$$x_2 = \frac{f}{3}\left[\cos\left(\frac{9g}{2f^3}\right) + \sqrt{3}\sin\left(\frac{9g}{2f^3}\right)\right] - \frac{b}{3a} \quad \text{(B-6)}$$

$$x_3 = \frac{f}{3}\left[\cos\left(\frac{9g}{2f^3}\right) - \sqrt{3}\sin\left(\frac{9g}{2f^3}\right)\right] - \frac{b}{3a} \quad \text{(B-7)}$$

When $h > 0$, there is only one real root and we proceed as follows,

$$R = \left[-(g/2) + (h)^{1/2}\right]^{1/3} \quad \text{(B-8)}$$

$$S = \left[-(g/2) - (h)^{1/2}\right]^{1/3} \quad \text{(B-9)}$$

$$x_1 = (R + S) - (b/3a) \quad \text{(B-10)}$$

$$x_2 = -(R+S)/2 - (b/3a) + i * \frac{\sqrt{3}}{2}(R-S) \quad \text{..... (B-11)}$$

$$x_3 = -(R+S)/2 - (b/3a) - i * \frac{\sqrt{3}}{2}(R-S) \quad \text{..... (B-12)}$$

When $f = 0$, $g = 0$, and $h = 0$, all 3 roots are real and equal and we proceed as follows,

$$x_1 = x_2 = x_3 = -(d/a)^{1/3} \quad \text{..... (B-13)}$$